



Center of Excellence for Explosive Detection, Mitigation and Response

Center of Excellence for Explosive Detection, Mitigation and Response

A Department of Homeland Security
Center of Excellence

University of Rhode Island (URI);
California Institute of Technology; Purdue University
New Mexico State University; University of Illinois
Florida International University Hebrew University, Jerusalem Israel
Weizmann Institute of Science

Third Annual Report
July 2010-September 2011

DHS agreement number: 2008-ST-061-ED0002

Table of Contents

Introduction	1
Characterization	
<i>Denaturing Explosive Precursors</i> James Smith & Jimmie Oxley (URI)	5
<i>Performance Estimation for HME</i> Jimmie Oxley & James Smith (URI)	14
<i>Simulants for X-ray Explosive Detection Systems</i> Jimmie Oxley & James Smith (URI)	25
<i>Theoretical Projects within the Center of Excellence</i> Ronnie Kosloff (Hewbrew UJI) & Yehuda Zeiri (BGU)	32
<i>Characterization of Non-Ideal Explosives</i> Steve Son (Purdue)	37
<i>Simulants for Canines & IMS Explosive Detection Systems</i> Jose Almirall (FIU)	41
Detection	
<i>Explosive Particles Sampling & Detection</i> Yehuda Zeiri (Ben Gurion U)	51
<i>New Sensors for Explosives Detection</i> William Euler (URI)	59
<i>Development of Resonating Nanocantilever Chemical Vapor Sensors and Thiol Encapsulated Gold Nanoparticle Chemiresistors</i> Nathan S. Lewis (CIT)	62
<i>Persistent Surveillance Technique for the Detection of Explosives & Precursors</i> Otto Gregory (URI)	69
<i>Gas Phase Ion Chemistry</i> Gary Eiceman (NMSU)	80
<i>Solution-Based Direct Readout SERS Method for Detection</i> Radha Narayanan (URI)	85
<i>Shaped Femtosecond Pulses for Remote Chemical Detection</i> Yaron Silberberg (Weizmann)	90
Mitigation	
<i>Damage Criterion & Residual Life of Structural Steel Subjected to Blast Loading</i> H. Ghonem (URI)	94
<i>Development of Novel Composite Materials & Structures for Blast Mitigation</i> Arun Shukla (URI)	101
<i>Attenuation & Mitigation of stress waves propagating in blast shielding materials</i> Carl-Ernst Rousseau (URI)	109
<i>Structural Response to Non-ideal Explosions</i> J. E. Shepherd (California Institute of Technology)	113
<i>Water Blast Mitigation: Progress Report</i> Steve Son (Purdue University)	119
<i>Self Healing Materials for Autonomic Mitigation of Blast Damage</i> Nancy R. Sottos (U of Illinois)	124
<i>Self-Healing Concrete</i> Arijit Bose (URI)	129

University of Rhode Island (URI)
DHS CoE in Explosives Detection, Mitigation, Response & Characterization

The mission of the DHS Center of Excellence in Explosives Detection, Mitigation, Response is to protect the nation from physical and economic harm caused by the threat, real or perceived, of attack using explosive devices. We take a four part approach to achieving our mission:

- identification/characterization of the most likely explosive threat scenarios to include compositions/formulations and design of ways to counter threat scenarios;
- development of detection schemes appropriate for each threat should countering fail;
- design and retrofit structural components to mitigate catastrophic results if there is failure at preventing a bombing.
- education of the next generation

Identification and characterization of the threat includes projects such as

- 1) identification of future threats by developing small-scale, “early warning” tests (Oxley-Smith & Son projects). Potential customers: TSA, FBI, military, the chemical industry;
- 2) determination of ways to prevent commonly available chemicals from being used to make explosives, including chemical denaturation and administrative controls and gentle destruction techniques (Oxley-Smith). Potential customers: DHS, the chemical industry; bomb squads;
- 3) determination of explosive properties which would facilitate detection, destruction, or protection against threats (Oxley-Smith).
- 4) creation of explosives stimulants for explosive detection systems—x-ray (Oxley-Smith); canines & IMD (Almirall)

These objectives are being addressed by both experimentally and theoretically (Kosloff & Zeiri)

Development of detection technologies for trace, bulk, standoff and persistent detection will continue. URI and partner universities are emphasizing trace, standoff and persistent detection schemes. The study of trace detection techniques began with examination of particle-substrate adhesion (Zeiri), which help inform all of the other detection methods on the issues of analyte capture. Trace detection approaches include the development of novel surfaces porous silicon (Euler) to amplify fluorescence quenching, dogbone-shaped gold nanoparticles (Narayanan) to develop a sensitive Surface Enhanced Raman Spectroscopic method, and swelling polymers (Lewis) to take advantage of the sensitive response of electrical measurements. A detailed examination of ionization of analytes and their response to the common trace instrument IMS (Eiceman) has also been pursued. In addition two standoff detection techniques are being developed: persistence surveillance of air borne particles and vapor via catalytic decomposition on micro sensors (Gregory); and resolved femtosecond CARS vibrational spectra for standoff detection (Silberberg).

Blast mitigation efforts for structural protection have focused primarily on three different aspects, namely, mitigation of blast pressure prior to hitting a structure, developing new materials for better structural resilience and improving the post blast performance of structures by incorporating self healing agents in the material. The effectiveness of water mist as a pressure dampener and blast mitigant has been evaluated. Novel composite materials with graded structures, particulate components, sandwich constructions and self healers have been developed and studied. In addition to new materials, projects have sought to understand failure and model structural response of widely used current materials like glass, low carbon steel and concrete for the purpose of new design criteria and for damage projections. New glass panels with protective

coatings were designed and tested for superior blast protection. The effect of geometry of structural panels on blast response was also studied. Procedures to understand the residual life of steel structures subjected to blast were developed and based on this understanding methods to create better steels have been proposed.

Education: Our work in this field to date is as follows. Each University project in the Center supports one or more graduate students. (See listing on the projects.) This is their best learning experience. Undergraduates are also supported on the projects as their class schedules permit. In addition, URI has a traveling magic shows for elementary and junior high students. For the past two summers we hosted Minority Scholars and for the last three summers we have hosted high school science teachers. In the summer of 2011 our Center supported eight high school teachers to conduct research at University of Rhode Island (URI). Four teachers of physics were placed in URI engineering departments. One worked on chemical sensors with a URI chemical engineering group (Professor Gregory) and the other three worked on blast mitigation projects with different URI mechanical engineering groups (Professors Shukla, Ghonem, Rousseau). The four teachers of chemistry were placed in the URI chemistry department. One worked with Professor Euler on chemical sensors and the other three worked on explosives characterization projects with Professors Oxley and Smith. The teachers worked fulltime for 8-10 weeks. They were required to prepare a poster and give a brief presentation of their work at the end of their tenure. The purpose of this program is to provide high school teachers with an opportunity to gain research experiences they can take back to the classrooms.

We have hosted and participated in a number of educational workshops.

TSA Bomb Appraisal Officers short courses	June 1-3, 2010
briefing to Under Secretary O'Toole	June 11, 2010
summer visiting Professor (Dr. Bu) and graduate student from Clark Atlanta University	
TSA Bomb Appraisal Officers short courses	July 25, Aug 12, Sept 16, 2010
TSA Fundamentals of Explosive short course	Aug 9-11, 2010
IMPLAST 2010	October 12-14, 2010
Texas Tech & ALERT safety course	October 27, 2010

Over 300 working professionals took part in one of our advanced studies courses.

Nano-energetics	20	May 25-26, 2010
Pyrotechnics	28	June 7-10, 2010
Fundamentals of Explosives	24	July 26-28, 2010
Material Characterization & Processing	19	Sept 21-23, 2010
Unintended Ignitions Sources/Hazards	19	Oct. 20-22, 2010
Terrorism Issues	18	Apr 26, 27, 2011
Fundamentals of Explosives	37	May 3-5, 2011 URI
Propellants & Combustion	18	May 9-10 2011
Insensitive Munitions	26	May 10-11, 2011
Detonation & DDT	20	June 7-9, 2011
Dynamic Response of Materials	15	July 21-22, 2011
Explosive Safety-Protocol	16	August 2,3 2011
Detonation & DDT	35	Sept 6-8 2011 SNL
Dynamic Diagnostics	13	Sept 28-29 2011
Explosive Devices & Train Design		Oct 25-27, 2011

Denaturing Explosive Precursors

P.I. J. Smith; J. Oxley;

Grad Students: J. Brady; Pat Bowden; Lucus Steinkamp; Guang Zhang
University of Rhode Island

Objective

The long-term *goal* is to identify ways to control chemical precursors of explosives. Some will require administrative controls; some can be adulterated yet still fulfill their intended function but not be diverted for illicit purposes. Our *approach* was to target the precursors—hydrogen peroxide (HP), acetone (used in TATP manufacture); and potassium nitrate (KN) (used in black powder). For HP, we attempted to find a way to prevent concentration of the widely available 3% HP. For KN we attempted to find a way to prevent its use in making urea nitrate. For acetone we sought to decompose the HP in situ or divert it to reaction with other species. Our attempts to prevent concentration of HP were successful and resulted in a patent. Our efforts to divert production of KN explosives or TATP were moderately successful, as well. Furthermore, we have expanded our efforts to include finding ways to destroy TATP, gently.

Accomplishments

Executive Summary

Hydrogen Peroxide: Because those who would synthesis hydrogen peroxide (HP) generally begin with boiling to remove water and thus concentrating the HP, we sought ways to thwart production of explosives at this step. We tested 75 different additives to determine if they accelerated HP decomposition at the elevated temperatures, such as used by terrorists to boil off water. The added requirement for these additives is that they did not adversely affect HP shelf-life. We have found 5 to 10 species, which at parts-per-million levels, cause HP (3wt%, 12wt% or 30wt%) solutions to quiescently decompose rather than concentrate. These additives are not toxic, and studies showed that shelf-life is not adversely affected by addition of the selected additives.

TATP Mitigation: The precursors for TATP synthesis, hydrogen peroxide and acetone, are available to the general public. To address the problem of proliferation of TATP, a two-fold approach was taken: 1) seeking a practical way for law enforcement to safely, gently destroy TATP stores; and 2) determining the mechanism of TATP synthesis for the purpose of thwarting its manufacture. The goal was to find a safe, effective, field-usable way to destroy TATP or prevent its synthesis. Acid is used to catalyze TATP synthesis; it also destroys TATP. Strong acid reacts so quickly with TATP that it can be used to initiate its explosion. Therefore, it became essential for us to understand the mechanism of TATP formation and TATP destruction so that acid could be safely employed. For destruction, a combination of carefully controlled acid strength and slightly solvated TATP reduced the rate of heat release so that safe destruction was possible.

Conditions which result in the formation of triacetone triperoxide (TATP) or diacetone diperoxide (DADP) from acetone and hydrogen peroxide (HP) have been studied for the purposes of inhibiting the reaction. The reaction of HP with acetone precipitates either DADP or TATP, but the overall yield and amount of each was found to depend on (1) reaction temperature; (2) the molar ratio of acid to HP/acetone; (3) initial concentrations of reactants, and (4) length of reaction. Controlling molar ratios and concentrations of starting materials was complicated by the fact that both sulfuric acid and hydrogen peroxide were aqueous solutions. Temperature appeared to exercise great control over the reaction. Holding all molar concentrations constant and raising the temperature from 5 to 25°C showed an increase of DADP over TATP formation and a decrease in overall yield. At 25°C a good yield of TATP was

obtained if the HP to acetone ratio was kept between 0.5-to-1 and 2-to-1. At constant temperature and HP-to-acetone held at a one-to-one ratio, optimal acid-to-HP molar ratio appeared to be between 0.10:1 and 1.2:1. Plotting the molality of HP versus that of sulfuric acid revealed regions in which relatively pure DADP and TATP could be obtained. Because there has been much speculation of the relative stability, sensitivity and performance of DADP and TATP, standard tests (DSC, drop weight impact, and SSED) were performed.

To inhibit the reaction between acetone and hydrogen peroxide we sought chemicals to adulterate the precursors without interfering with their desired usage. Ideally, an adulterant could be kept at a loading of 1% or less, be relatively non-toxic and completely inhibit formation of TATP under nearly all conditions. Our approach was to look for species that destroyed hydrogen peroxide, diverted hydrogen peroxide (by reacting with it), quenched the acid catalyst, or made isolation of TATP cumbersome. Over one hundred adulterants, chosen from eight classes of reagents were tested: (1) antioxidants; (2) radical initiators; (3) metal salts. (4) halides and halogenated organics; (5) amines and inorganic bases; (6) molecules containing reactive bonds; (7) ketones other than acetone; (8) organic solvents to prevent TATP precipitation. None of the adulterants were effective below the 10 wt% level. Basic substances, other ketones, and iodine salts were effective in preventing TATP formation; however, for various reasons they were judged unlikely to be employed for this purpose.

Details of Patent for Prevention of Hydrogen Peroxide Concentration:

To use HP as the main ingredient in a liquid explosive, its concentration must be greater than 60wt%. While industries routinely purchase HP of 50 wt% concentration, generally, the public can only purchase 3wt% HP, widely available in pharmacies for disinfectant use. Beauty supply houses distribute 12wt% (termed 40 vol %) for hair bleaching, and spa chemical supply houses sell 27wt% HP. The would-be bombmaker generally can purchase, 3wt% or 12wt% HP and concentrate these by simple open boiling to remove water in order to acquire 35wt% HP or greater for purposes of efficient bombmaking. We have found a set of chemicals which, present in HP at ppm levels, enhance HP decomposition at elevated temperatures. The result is that would-be bombmakers are thwarted in their attempts to concentrate retail-grade HP. They are prevented from diverting retail HP from its intended use, and using it to create bombs. The chemicals included have some or all of the following advantages:

- At elevated temperatures they enhance HP decomposition;
- They function at the part-per-million (ppm) scale or below;
- (often they function below therapeutics levels)
- They are generally regarded as safe (gras);
- At the concentration they are used in HP, they impart no noticeable color to the HP;
- At ambient temperatures the shelf-life of HP containing ppm-levels of these additives is not substantially reduced.

The chemicals at the 100 ppm level or below found to be effective in destroying HP include those containing inorganic salts, phthalate, benzoate, citrate, and acetate salts as well as glycols and a number of amines. Good catalysts for HP degradation at the 10 ppm level or below are metal salts with oxo or electronegative ions e.g. carbonates, sulfates, iodates, nitrates, fluorides and chlorides. Effective at ppm levels less than 10 are oxo and halide salts of the first-row transition metals.

Figure 1 shows the concentration of HP after heating at 125°C for 8 to 10 hours. The blue line would be the concentration of HP if during heating only water was lost from the HP solution. However, some HP is actually destroyed during heating; the black line is the observed

concentration change; some additives do nothing to enhance HP decomposition (green markers). The red markers show the resulting HP concentration for HP solutions containing additives which promote HP decomposition. Among the red markers there are a number of additives which at 1.25 ppm ($\mu\text{g/mL}$) concentration dramatically accelerated HP decomposition during heating at 125°C. Tables 1 and 2 show the additive and amount used, the theoretical (theo) concentration of HP expected, the observed (obs) concentration of HP, and the percentage of HP destroyed in the process of distilling 3wt% HP to 30wt% (Table 1) or 12wt% to 60wt% (Table 2). A value of "100%" represents a total destruction of HP during the evaporation process.

Table 1: HP (3wt%) with 1 ppm additive heated at 125C until volume reduction suggested ~30wt% HP

3wt% HP	% destroyed	%HP obs	HP% theo
Blank	12.9	23.0	26.4
CerrAmmSulf	35.1	13.6	21.3
CoCl ₂	33.8	19.5	20.7
CrCl ₂	92.1	2.1	28.7
CuAcet	98.8	0.2	31.1
CuCl ₂	99.4	0.2	70.5
Fe(NO ₃) ₃	23.1	21.1	27.2
FeCl ₂	40.5	14.4	23.8
KIO ₃	43.3	12.9	23.9
MnSO ₄	23.1	18.1	23.2
ZnAcetate	35.5	19.5	30.0
ZnCl ₂	32.9	19.5	29.3

Table 2: HP (12wt%) with 1 ppm additive heated at 125C until volume reduction suggested ~60wt% HP

12wt% HP	% destroyed	%HP obs	HP% theo
Blank	15.7	50.3	60.0
CerrAmmSulf	35.7	32.6	51.7
CoCl ₂	28.2	37.7	56.9
CrCl ₂	41.4	37.5	65.0
CuAcet	70.4	29.3	98.9
CuCl ₂	60.9	37.4	96.1
Fe(NO ₃) ₂	36.0	32.8	54.8
KIO ₃	32.9	34.3	50.5
MnSO ₄	29.5	38.4	55.1
ZnAcet	38.6	31.7	51.6
ZnCl ₂	46.3	32.1	60.8

Example of Experimental Details: CrCl₃ (40 μg) was added to 40 mL (40.44 g) of 3% hydrogen peroxide and the solution is heated at 125°C until 3.8 g of solution remained, the concentration of the HP was 2.3wt% (as analyzed by refractometry or titration) Without the degradation agent, the calculated concentration of the solution was 31.9%.

A literature search for potential toxicity of these additives was performed. It was found that all the additives except the cerium (Ce) salts are essential micronutrients. An individual would need to purposefully ingest liters of a hydrogen peroxide solution adulterated with the potential additives to exceed the FDA's Recommended Daily Allowance. We believe these additives could be used to denature HP sold into certain markets. We have found that some of the same additives used to denature 3% HP also denature 12% and 30% HP, two other commercially available concentrations of HP. Thus, it would become impossible to concentrate products such as Clairoxide 40 to use it to produce liquid explosives.

It is important that the additive employed would not shorten the shelf-life of the product; therefore, we conducted standard aging tests. Accelerated aging studies were performed at 65°C for 226 days. At this temperature that length of time was equated to an ambient shelf-life of 2 years, which is the present advertized shelf-life. When hydrogen peroxide of 3wt%, 12wt%, or 30wt% was sealed in a glass ampoule with 0.25ppm of one of the potential salts, less than 3% of the HP was destroyed compared to the unadulterated HP.

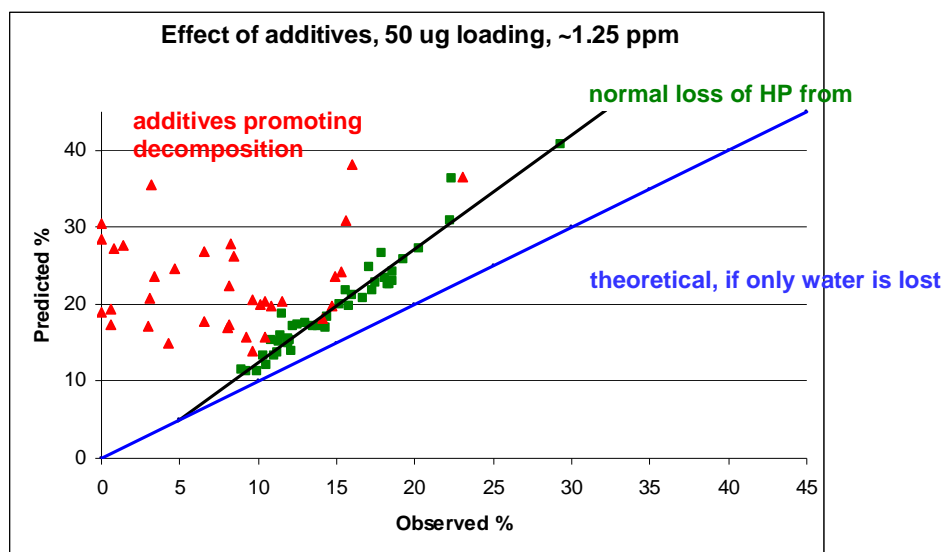


Fig. 1: HP Concentration Change upon Heating

TATP Mitigation

Beginning in Israel in the 1980's, terrorist attacks have used TATP, either as the main or initiating charge. A few of those incidents are shown in Table 1.

Table 1: Terrorist Use of Peroxide Explosive

Where:	Who:	What:	When:	Ref:
Flight to US	Richard Reid	TATP initiator in "Shoe Bomb"	12/14/2001	23
NY/Denver	Najibullah Zazi	Collected HP as a precursor	Sept. 2009	24
London	Group of 6	Subway attempt, TATP & HP/Fuel	7/21/2005	25
Denmark	Lors Dukayev	Attempted letter bomb, TATP	9/10/2010	26
S. Hadley, MA	Jack Robison Jr.	Amateur Chemist, home-made TATP + Other Explosives seized	2007-2008	27
Texas City, TX	Matthew Rugo	Killed while grinding TATP + metals	7/21/2006	28

Currently, the safest way to dispose of illegal explosives is to blow-in-place. This procedure keeps law enforcement from handling and transporting these highly sensitive materials. However, because the peroxide explosives are frequently found in apartments and other high-population density areas, blow-in-place protocols are impractical. In recent years we have examples of finds of illicit explosives where law enforcement went to extreme measures to destroy on the premises: "...the Escondido rental home contained the largest amount of certain homemade explosives ever found in a single U.S. location. Nearly every room was packed with piles of explosive material and items related to making homemade bombs....technicians found six mason jars with highly unstable Hexamethylene triperoxide diamine, or HMTD...." KTLA News 11:53 a.m. PST, Dec 11, 2010 "ESCONDIDO, Calif. (AP) Authorities say the controlled burn of a home packed with explosives cost the San Diego County Sheriff's Department more than \$541,000." Feb 2, 2011 CBS 8 (KFMB)

The goal of this work was to find a safe, effective, field-usable destruction method. Few reports address this issue. We sought a room-temperature, general, chemical destruction method for peroxides. Previously, we found that at the milligram scale, concentrated sulfuric acid effectively destroyed TATP; however, on scale-up to 1 gram, the heat released in the reaction caused a violent release of energy, perhaps detonation. We next looked for an all-liquid chemical solution that could be sprayed over solid peroxide "finds" or in which peroxide saturated materials could be immersed and the peroxide would quiescently be destroyed with no further handling. The desired chemical solution should destroy within hours either TATP or HMTD so that white illicit explosives would not require prior characterization. While a number of mixtures were found effective against solutions of the peroxides, strong acids proved the most useful against the solid peroxide materials. Initial studies did not go beyond the gram scale.

TATP is made by the reaction of acetone and hydrogen peroxide. Under the right conditions these two reagents will slowly form some TATP at room temperature. However, when synthesis of TATP is desired, the amount and rate of the acid addition and the temperature maintained during the reaction is carefully controlled. With too much acid or too high a temperature the reaction may form DADP, or may explode violently. In fact, TATP can be initiated to detonation by addition of acid or simply induced to gently decompose. We explored the region where acid can be used to affect quiescent decomposition of TATP. This work mainly focused on the destruction of 0.5 g or 3g quantities of solid TATP, but kinetics of TATP solutions were also examined. Successful, field tests were performed on 100g quantities of TATP.

For the destruction, 500 mg of recrystallized TATP was placed in clear 40 mL glass vials and moistened with an organic solvent (aqueous and anhydrous ethanol, aqueous and anhydrous isopropanol, aqueous ethylene glycol, ethyl acetate, iso-octane, toluene or acetone). The volume of solvent (0.5, 1, 2 or 4 mL) was insufficient to dissolve the TATP even if it were a solvent in which TATP was soluble. In fact, with 1 mL or less solvent the TATP did not even appear wet. Acid [HCl, H₂SO₄, HNO₃, H₃PO₄, HClO₄, trifluoroacetic acid, methanesulfonic acid (MSA)] was added to the TATP to initiate decomposition. Various concentrations (20%, 35%, 50%, 65% and 80% sulfuric acid, 36% and 18% hydrochloric acid, and 70% nitric acid) and amounts (0.5, 1, 2, 3, 4, 5 or 9 mL) were employed. All mixtures were allowed to react at room temperature uncovered for 2-24 h.

Addition of a mineral acid could be the perfect field approach to destroying TATP. The reagent is an inexpensive liquid, and as a liquid one could envision it being applied as a spray or mist with no stirring required. The problem was identifying which acid and acid concentration would destroy TATP, which would have no effect, and which would cause an instant violent reaction (an explosion). All three reactions were observed. A survey of acids was performed, which showed that all strong acids were effective in destroying TATP (Table 2). In the survey and in all subsequent systems an organic solvent was used. Without solvent the reaction with concentrated acids was dangerously violent, and with dilute acids it was non-existent. Instead of attempting to dissolve TATP, just enough solvent to wet the TATP was used. We found that acid destruction was effective in a ratio of one milliliter of alcohol to 2 mL of acid. Moistening with solvent prevented an instant exothermic reaction with the acid; a controlled decomposition occurred. It is assumed that as the layer of dissolved TATP reacts with the acid, more TATP is dissolved.

Table 2: Percent TATP remaining after acid treatment (1:2 is solvent to acid ratio)

Solvent	MeSO ₃ H	HClO ₄	HCl 36%	H ₂ SO ₄ 65%	HNO ₃ 70%	CF ₃ CO ₂ H	BF ₃	H ₃ PO ₄	CH ₃ CO ₂ H
3h IPA EtOH 50%	1:2 0%	1:2 0%	1:2 9-0%	1:2 37-30%	1:2 0%	1:2 1-0%	1:2 0%	1:2 83- 75%	2:2, 2:3 100%
24h toluene	1:0.5 43%	1:0.5 violent	0.5:2 36%	0.5:1 73%	1:0.5 0%				
pK _a	-13	-8	-6.3	-3	-1.64	0.23		2.15	4.75

The key to controlling the acid destruction of TATP is maintaining a balance between the wetting solvent, the acid and the TATP. To examine this relationship and to determine how low a concentration of acid could be employed, a more detailed survey was performed (Table 3). In those tests the vials of reactants were allowed to sit at room temperature between 3 and 6 hours or between 17 and 24 hours. As the acid concentration was decreased (sulfuric from 65% down to 20% or hydrochloric 35% to 18%) TATP destruction became less complete. A larger volume of lower concentration acid, i.e. the same number of moles, did not aid destruction, probably because the increase in amount of water lowered the solubility of the TATP.

Table 3 Ratios of Solvent-to-Acid Destroyed TATP(white squares no more than 25% remaining)

mL:mL solvent:acid	H ₂ SO ₄ , 65%		H ₂ SO ₄ , 50%		H ₂ SO ₄ , 35%		H ₂ SO ₄ , 20%		HCl, 36%		HCl, 18%	
	3-6 hr	17-24 hr	3-6 hr	17-24 hr	3-6 hr	17-24 hr	3-6 hr	17-24 hr	3-6 hr	17-24 hr	3-6 hr	17-24 hr
EtOH, 100%		1:2, 2:2		1:3, 2:3		1:5 2:5		1:9, 2:9		1:2, 2:2		1:4, 2:4
EtOH, 90%		1:1, 1:2, 2:2		1:2, 2:2; 1:1-30%		2:2-30%; 1:2-40%; 1:1-75%						1:0.5, 1:1
EtOH, 70%			1:1:1:2		1:1:1:2		1:1:1:2		2:2:1:4:2:4; 1:1-30%; 2:1-78%		1:1:1:2	
EtOH, 50%	1:2	1:2, 2:2 (80%acid 1:1)	2:2:2:4	1:3:2:3	2:2:2:4	1:5:2:5	2:2:2:4	1:9:2:9	1:1, 1:2 1:4; 2:2; 2:4 *1:1-	1:2, 2:2	2:2:2:4	1:4:2:4
i-PrOH, 100%	0.5:1; 1:1, 2:2	1:1, 2:2		1:1-30%; 2:2-20%		1:1; 2:2		1:1; 2:2	0.5:1, 1:1, 1:2, 2:2, 2:4 boil	0.5:1, 1:1, 1:2, 2:2, 2:4		1:1; 2:2
i-PrOH, 90%	1:1, 1:2- 44,77%	1:1, 1:2	1:1:1:2	1:1; 1:2	1:1:1:2	1:1; 1:2	1:1:1:2	1:1; 1:2	1:1, 1:2	1:1, 1:2	1:1:1:2	1:1; 2:2
i-PrOH, 50%	1:2								1:2			
EG/H ₂ O (1:1)		1:2, 2:2		1:3,2:3		1:5,2:5		1:9,2:9		1:2, 1:4; 2:2-40% remain		1:4,2:4
EtAcetate		2:2		2:3		2:5		2:9		2:2		2:4
Acetone	0.5:1; 1:1	0.5:0.5, 1:0.5							0.5:1, 1:1boils	0.5:0.5, 1:0.5		
Toluene		0.5:1, 0.5:2	0.5:0.5, 1:0.5	0.5:1, 0.5:2	0.5:0.5, 1:0.5			0.5:1, 0.5:2	0.5:0.5, 1:0.5	0.5:0.5, 0.5:1, 0.5:2	0.5:0.5, 1:1	
i-Octane		1:2		1:3		1:5		1:9		1:2		1:4

*solvent (mL) : 0-25 25-50 71-100 % remaining

On-going Work:

TATP/DADP Synthesis and Mechanism: The key to controlling the acid destruction of TATP is maintaining a balance between the wetting solvent, the acid and the TATP in order to control the rate of reaction. Rate of reaction is being studied in solution with various concentrations of sulfuric and hydrochloric acids. All strong acids were effective in destroying TATP (Table 3), but not every acid was compatible with the organic solvent used. In other acids, DADP formation was observed and, in many cases, minor amounts of species we tentatively identified as peroxo-acetone species. DADP is also decomposed by the acid, but at a much slower rate than TATP. Since all reactions were allowed to progress at room temperature for the same length of time, (3 hours), the amount of DADP observed was directly related to the rate of the TATP decomposition in each acid. Studies are underway to determine the controlling factors in DADP versus TATP formation.

The mechanism of peroxide formation from ketones was last studied 30 years old. Present evidence shows some serious flaws. Studies are underway to better understand both formation and destruction. Furthermore, internet blogs claim DADP formation should be avoided since it is more sensitive than TATP. This claim is being investigated.

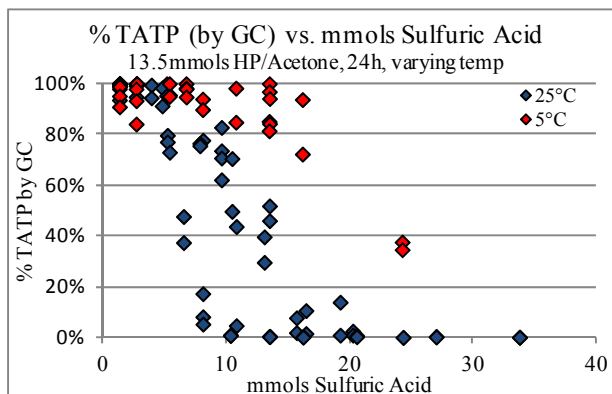


Fig. 1: Effect of Acid on TATP Formation

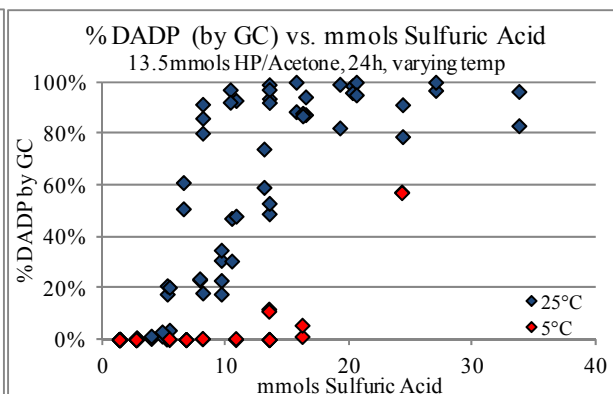


Fig. 2: Effect of Acid on DADP Formation

Graduate Students (partially supported)



Joe Brady Pat Bowden Lucas Steinkamp Guang Zhang Maria Donnelly Matt Porter
 PhD Jul 2011 PhD Nov 2011
 Brookhaven NL Los Alamos NL

Papers

Oxley, J.C.; Smith, J.L.; Brady, J.E.; Hart, C.E. Estimating Ambient Vapor Pressure of Low Volatility Explosives by Rising-Temperature Thermogravimetry; Propellants, Explosives, Pyrotechnics, accepted

Oxley, J.C.; Smith, J.L.; Brady, J.E.; Brown, A.C. Characterization and Analysis of Tetranitrate Esters, Propellants, Explosives, Pyrotechnics, accepted

Wilson, S.A.; Brady, J.E.; Smith, J.L.; Oxley, J.C. The Risk of Mixing Dilute Hydrogen Peroxide and Acetone Solutions accepted J of Chemical Health & Safety

Oxley, J.C.; Smith, J.L.; Kirschenbaum, L.; Marimiganti, S.; Efremenko, I.; Zach, R.; Zeiri, Y. Accumulation of Explosive in Hair: Part 3: Binding Site Study accepted to J Forensic Sci

Presentations

PhD Thesis Joseph Brady July 18, 2011
 Clinical Lab Science Convention; Providence, May 4, 2011
 Wheaton College Chemistry Seminar April 6, 2011
 MIT Lincoln Labs Feb 24, 2011
 Warwick Rotary Club Warwick RI Jan 6, 2011

CSHEMA Reactive Chemicals Webinar Jan 19, 2011
URI Explosive Research for Safety and Security; Grand Challenge Course Dec. 9, 2010
IEEE Tutorial on the Explosive Threat; Waltham, MA Nov. 9, 2010
Soc Experimental Mechanics IMPLAST 2010 Blast Mitigation Wkp; Providence, RI Oct 14, 2010
What & Where to Look ; Oakland University, Chemistry, Dept. Detroit, Sept 29 2010
Overview of DHS Center of Excellence; Texas Tech, Chemistry; Lubbock, TX; Oct 27 2010
½ tutorial for UnderSecretary Tara O'Toole, Washington, DC June 11, 2010
1 day tutorial TSA Bomb Appraisal Officers; Charlotte, NC, June 3, July 15, Aug 12, Sept 16, 2010
Clinical Lab Science Convention; Providence, May 4, 2011
Wheaton College Chemistry Seminar April 6, 2011
MIT Lincoln Labs Feb 24, 2011
Warwick Rotary Club Warwick RI Jan 6, 2011
CSHEMA Reactive Chemicals Webinar Jan 19, 2011
URI Explosive Research for Safety and Security; Grand Challenge Course Dec. 9, 2010
IEEE Tutorial on the Explosive Threat; Waltham, MA Nov. 9, 2010
Soc Experimental Mechanics IMPLAST 2010 Blast Mitigation Wkp; Providence, RI Oct 14, 2010
What & Where to Look ; Oakland University, Chemistry, Dept. Detroit, Sept 29 2010
Overview of DHS Center of Excellence; Texas Tech, Chemistry; Lubbock, TX; Oct 27 2010
½ tutorial for UnderSecretary Tara O'Toole, Washington, DC June 11, 2010
1 day tutorial TSA Bomb Appraisal Officers; Charlotte, NC, June 3, July 15, Aug 12, Sept 16, 2010

Characterization: Performance Estimation for HME

PI J. Oxley, J. Smith, J. Kennedy, S. Stewart; Grad Students: P. Bowden & R. Rettinger

Objective:

The long-term *goal* is to develop a test that allows early identification of detonable formulations at a scale which is safe and relatively inexpensive in terms of time and materials.

Many homemade explosives (HMEs), e.g. ANFO, don't release all their energy promptly at the detonation front. In these, loss of energy at edges becomes so significant that it is necessary to use large charges to achieve detonation, i.e. large critical diameter. This does not stop terrorists; they use them in VBIED's. For the researcher it means he may not observe detonability without using large amounts of material—expensive, time-consuming, & hazardous. A small-scale test is being developed to overcome edge effects so that detonability or lack thereof can be observed without regard to critical diameter. Target materials are those which fail to detonate at the scale of DoT testing but may be threats at large scale, i.e. tons.

Approach

With active confinement provided by a detonating annular booster, a convergent, overdriving shock wave is driven into the test material. If it is detonable, the test material will detonate regardless of its critical diameter because the shock is being driven from the edges, not lost at the edges. The goal of this research is to develop a test to observe detonability without requiring large amounts of material. By creating a small test we save time and money and make it possible to test large numbers of potential explosives or industrial hazards with significantly less hazard to the researcher. Hazard to the researcher is reduced because this detonability test uses less material and because less material need be synthesized.

To date we have conducted five test firings seeking a configuration appropriate for our approach. In the first three test series the device contained roughly 950 g (2 lb) total explosive weight surrounding a ~1" cylinder of the test material of ~60 mL volume. Those tests results suggested that the length and width of the booster charge (4" x 4" right cylinder) were not critical to the results; thus, in the fourth test series the outer cylinder was reduced to 3" in diameter, reducing the total explosive weight to about 500 g (1 lb). The test series experimented with the following variables summarized below:

type of flyer [series 1: flat disk (a nickel coin); series 2 & 3: steel ball; series 4 & 5: none];
stand-off distance from the witness plate;
detonator interrupter (low density polyethylene, high density polyethylene, none);
mode of initiating the booster;
chemistry of the booster and acceptor.

series	# shots	booster			inner		flyer	standoff	variables	
1	3-09	20	PVC	4" x 4"	H2O2/EtOH	acrylic	1"	nickel	7mm	H2O2 filler
2	8-09	22	PVC	4" x 4"	H2O2/EtOH	polycarbonate	1"	steel ball	6"	stand-off, ball, NM
3	11-09	36	PVC	4" x 4"	NM/NA	polycarbonate	1"	steel ball	10"	device size
4	5-10	41	PVC	3" x 4"	NM/NA	PVC	1"	none	8"	test liquids & solids
5	6-11	37	PVC	4" or 6" x 4" or 12"	NM/NA	PVC	1" or 2"	none	10"	flyer pipe, length, inner width
		156			7/3 NM/NA					
					60/27/13 HP/H ₂ O/EtOH					

In the *first test series*, a nickel coin was used as a flyer plate to impact a 1" thick steel witness plate about 7 mm beneath the test fixture. The annular booster was a detonable hydrogen peroxide (HP)/H₂O/ethanol (EtOH) mixture (60/27/13 wt %), labeled test mix "A," and the test material was a variety of HP formulations, which were demonstrated to be non-detonable in the 4" x 4" PVC test fixture. A variable in this series was the amount of sheet explosive used to couple the detonator impulse to the annular booster: one or two 2 mm sheets. A detonator interrupter (Fig 1- purple section), preventing impulse from going directly into the center acceptor material was placed

below the sheet explosive. Dents in witness plates ranged from 3 to 8 mm; in one heavily confined test using a steel rather than PVC booster made a 2 mm dent. There was a slight trend to observed larger dents with less detonable mixture, e.g. water 5mm. Severe bowing of the witness plate from the detonation of the annular booster and poor reproducibility of flyer dent caused us to change device configuration.

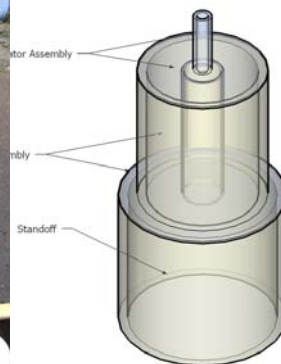
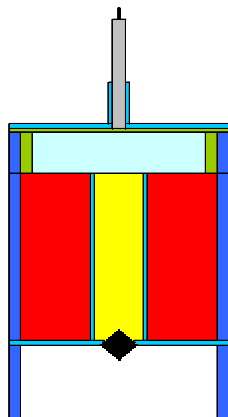
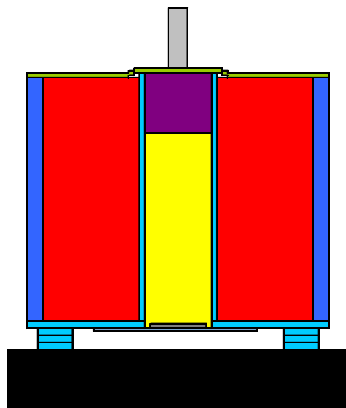


Fig. 1: Series 1 Fixture

Fig 2: Series 2 Ribbon Design

Fig 3: Series 4

In the *second test series* and the third a stainless steel ball flyer was used instead of a nickel (series 1). Eliminating a flat flyer removed our concern about it tumbling in flight; therefore the stand-off distance from the device to the witness plate could be increased from 7 mm to many inches; and damage to the witness plate by the booster was greatly decreased. For test series 2, the sealing of the flyer ball to the fixture was accomplished by melting the polycarbonate with dichloromethane, but leakage was a problem in many tests. The second test series used the same HP/H₂O/EtOH annular booster as series 1, in most of the tests. Six inch stand-off distance was determined to produce observable dents from the center test material without causing severe damage to the witness stack by the booster. In this test series, the sheet explosive configuration was varied from flat across the entire cylindrical device, with a high density polyethylene interrupter, to a ribbon of several strips of sheet explosive positioned 90° to the fixture top edge (Fig 2). The ribbon configuration produced smaller dents and was abandoned for the easier to fabricate flat initiator. Reproducibility of results was better, but differentiation between an inert (H₂O) and a detonable material (60/27/13 HP/H₂O/EtOH) was not great, 0.068" to 0.106" dent depths, respectively. Fixture length was increased from 4" to 8" without a dramatic change in results. What did change the results was changing the booster from HP/H₂O/EtOH to sensitized nitromethane (NM). It was clear sensitized NM was a more powerful annular booster; with the HP booster dent depths never exceeded 4 mm, whereas with NM they were 10 to 11 mm.

For *third test series*, the device configuration was not changed for that of series 2, but the hydrogen peroxide booster was replaced with sensitized nitromethane. This change required a redetermination of appropriate standoff distance; experimentation suggested 10" was best. The change also required investigation into the safest way to sensitize NM. Diethylenetriamine (DETA) reacts with hydrogen peroxide; therefore, concentrated nitric acid (70 wt%) was used to sensitize NM. Preliminary experiments suggested NM with 10% nitric acid (NA) was not detonable at 1" boosted by one 2mm thick sheet explosive; therefore, most of the tests were primarily performed using 30% NA although 20% and 50% concentrated NA were also tested. In the third series, one

variable examined was the size of the test fixture; it was increased from 4" to 6" in diameter and from 4" to 8" in length. The dents produced by the larger devices were not noticeably different from the smaller device; thus, in keeping with the goal of using less energetic material, the 4" x 4" fixture was used in most tests. In some tests in series 3 there was more than one main dent. In an attempt to eliminate or understand this problem a larger standoff (28") and inert solids (sugar and sand) were tested. Ordering the test materials in Table 1 from smallest to largest dent, no clear trend is seen among the solid materials. For the liquids, materials known to be detonable came out on top showing dents between 0 to 7 mm; those known to be inert, on the bottom, dents between 19 to 24 mm. This is a trend but exactly opposite from what we expected. We had expected that detonable materials would drive the flyer ball deep into the witness plate whereas inert materials would barely push it. Instead, inert materials, such as water and brine, bore large holes in the 1" steel witness plate and the detonable material left only the dent of the flyer ball. To understand this phenomenon, Scott Stewart (U of Illinois) modeled the test series 3 setup using ALE3D. The ALE3D model suggested that inert materials were propelled out of the inner tube as a jet which overtook the flyer ball, impacting the witness plate before the ball, hence, the presence of two dents in some test.

Table 2: Test Series 3 with Solid Acceptors

Solid Test Materials and Special Tests					
Test #	Size inches	Standoff (inch)	Annular NM Booster	inner test material	Dent Depth (mm)
28	4" x 4"	10	P	Percarbonate	-12.2
25	6" x 8"	12	P	DNT	-12.4
17	4" x 4"	10	P	Sand	-13.5
19	4" x 4"	10	P	Bullseye	-14.7
20	4" x 4"	10	P	AN	-14.7
29	4" x 8"	10	P	AN	-15.0
23	4" x 4"	10	P	Sugar	-16.0
26	4" x 4"	10	P	DNT	-24.6

Table 1: Test Series 3 with Liquid Acceptors

Test #	Size inches	Standoff (inch)	Annular NM Booster	inner test material	Dent Depth (mm)
1	4x4	6	O= 8/2 NM/NA	C = 50HP/5EtOH	
2	4x4	8	O= 8/2 NM/NA	C = 50HP/5EtOH	-9.91
3	4x4	10	O= 8/2 NM/NA	C = 50HP/5EtOH	
Liquid Test Materials					
Test #	diameter x length	Standoff (inch)	Annular NM Booster	inner test material	Dent Depth (mm)
15	4" x 8"	10	P = 7/3 NM/NA	P = 7/3 NM/NA	0.0
22	6" x 8"	12	P	P	-6.6
9	4" x 4"	10	P	P	-2.9
5	4" x 4"	10	O= 8/2 NM/NA	O = 8/2 NM/NA	-2.5
32	4" x 8"	10	P	A= 70HP/13EtOH	-5.0
18	4" x 4"	10	P	A= 70HP/13EtOH	-5.5
3	4" x 4"	10	O	C = 50HP/5EtOH	
10	4" x 4"	10	98/2 NM/deta	C = 50HP/5EtOH	-14.5
7	4" x 4"	10	P= 7/3 NM/NA	C = 50HP/5EtOH	-16.5
21	6" x 8"	12	P	C = 50HP/5EtOH	-15.5
31	4" x 8"	10	P	C = 50HP/5EtOH	-17.0
14	4" x 8"	10	P	C = 50HP/5EtOH	-18.3
8	4" x 4"	10	P	Brine	-24.4
16	4" x 8"	10	P	Brine	-25.4
4	4" x 4"	10	O	H2O	-19.3
24	4" x 4"	10	P	empty	-6.9
11	4" x 4"	10	50/50 NM/NA	C = 50HP/5EtOH	-9.1
12	4" x 4"	10	50/50 NM/NA	Brine	-19.3
27	4" x 4"	28	P	C	-3.0

The **fourth test series** reduced in diameter to 3," about 1 lb of explosive was required for the annular booster. This reduction in size was possible because of the change in annular booster from HP to NM. To make the inner tube walls impervious to NM, it was constructed of PVC rather than acrylic or polycarbonate; as a result its diameter became a little larger than 1." The biggest change was elimination of any flyer-no nuckel, no steel ball. We relied on a jet of unreacted material or lack thereof to leave its mark on the 7" witness plate stack. The top 2" were changed to aluminum to allow better differentiation between inert and explosive test materials. Table 3 shows a clear trend, albeit in reverse of our initial expectations. Non-

detonable materials, such as brine, produced large dents because the brine was focused and driven onto the witness plate, drilling a large hole. In contrast, detonable materials, detonated; no unreacted liquid remained to be driven into the witness plate; the witness plate remained flat. There is also a trend among the solid test materials, but unlike the liquid explosives, the solid explosives, e.g. the commercial emulsion explosive MagnaFrac® (Orica), produced a dent, though smaller than that made by the inert powdered polymethylmethacrylate (PMMA).

Table 3: Series 4 Solid Test Material

Shot #	Device diameter x length	Stand-Off Inches	Booster	Inner Mix no interrupter	Dent Depth (mm)	g of inner mix
				Solid Inner Material		
39	3" x 4"	8	70/30 NM/NA	MagnaFrac	-14	84
24	3" x 4"	8	70/30 NM/NA	DNT	-16	81
21	3" x 4"	8	70/30 NM/NA	87/13 AN/icing sugar	-17	82
23	3" x 4"	8	70/30 NM/NA	70/30 KN/icing sugar	-18	100
20	3" x 4"	8	70/30 NM/NA	AN	-20	82
22	3" x 4"	8	70/30 NM/NA	PMMA	-33	54

Table 4: Series 4 Liquid Test Materials

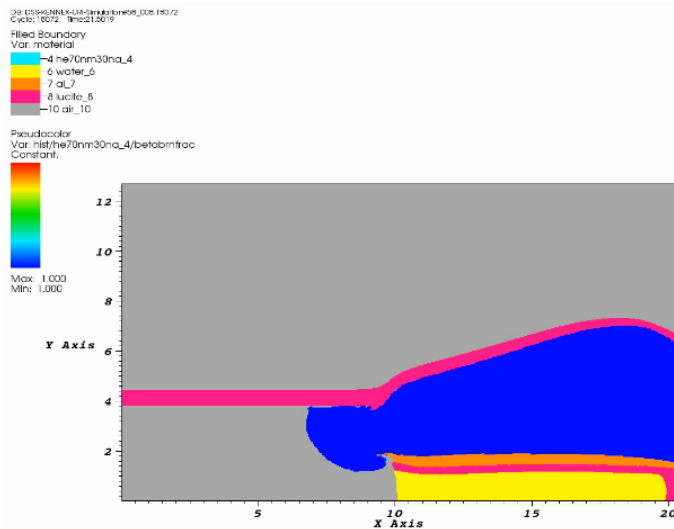
Shot #	diameter x length	Stand-Off Inches	Booster	Inner Mix	Dent Depth (mm)	g of inner mix
				Liquid Inner Materials		
14	3" x 4"	8	70/30 NM/NA	70/30 NM/NA No Det. Int.	-2	89
35	3" x 4"	8	50/50 NM/NA	70/30 NM/NA	-4	67
19	3" x 4"	8	70/30 NM/NA	80/20 NM/NA	-4	66
36	3" x 4"	8	80/20 NM/NA	70/30 NM/NA	-5	67
40	3" x 4"	8	98/2 NM/DETA	70/30 NM/NA	-5	66
5	3" x 4"	8	70/30 NM/NA	70/30 NM/NA	-5	65
41	3" x 4"	8	98/2 NM/DETA	70% HP/ 13% EtOH	-11	66
17	3" x 4"	8	70/30 NM/NA	90/10 NM/NA	-11	65
18	3" x 4"	8	70/30 NM/NA	95/5 NM/NA	-11	63
34	3" x 4"	8	70/30 NM/NA	99.5/0.5 NM/DETA	-12	63
38	3" x 4"	8	98/2 NM/DETA	NM	-12	63
25	3" x 4"	8	70/30 NM/NA	50/50 NM/NA	-13	71
9	3" x 4"	8	70/30 NM/NA	NM	-13	63
31	3" x 4"	8	70/30 NM/NA	80/20 NM/EtOH	-13	60
11	3" x 4"	8	70/30 NM/NA	80/20 NM/Acetone	-16	59
10	3" x 4"	8	70/30 NM/NA	90/10 NM/Acetone	-16	61
33	3" x 4"	8	70/30 NM/NA	30/70 NM/NA	-16	73
12	3" x 4"	8	70/30 NM/NA	70/30 NM/Acetone	-17	56
27	3" x 4"	8	70/30 NM/NA	70/13 HP/EtOH	-19	67
29	3" x 4"	8	70/30 NM/NA	50/10 HP/EtOH	-26	63
30	3" x 4"	8	70/30 NM/NA	50/30 HP/EtOH	-28	59
7	3" x 4"	8	70/30 NM/NA	50/5 HP/EtOH No Det. Int	-37	85
6	3" x 4"	8	70/30 NM/NA	50/5 HP/EtOH	-39	64

Test Series 5

At this point the test differentiated non-detonable from detonable materials, and it achieved this with only a pound of explosives. Unfortunately, there remained a large number of “in-between” or questionable materials. They tended to make dents in the 11 to 18 mm range. A basic re-design of the test fixture was undertaken to provide greater initiating impulse. Four major changes were made to the test fixture: (1) To provide time for run-up to detonation of the acceptor, a device length of 12” as well as the usual 4” was used; (2) A larger diameter of acceptor with a diameter of 2” in addition to others with 1” diameters; (3) Because the void between the flyer pipe and the acceptor reduced the total volume of the booster material, the outer diameter of the booster was increased to 6” in addition to 4” diameter boosters; (4) To provide higher impulse to the acceptor, a flyer pipe was added to impact the acceptor along its entire length, instead of having the acceptor in direct contact with the booster. The later change required a great number of

calculations and still several flyer pipe thicknesses as well as gap widths were tried. Table 5 outlines the ten device configurations. Variables included length of the device, diameter of the booster and of the acceptor, flyer pipe wall thickness and gap to acceptor.

Nine 12" long, 1" diameter acceptor devices with either 4" or 6" outer diameter devices were used. All but one produced a flat witness plate. Our conclusion, discussed below, is that in the 12" long devices the jet of test material was destroyed before it reached the witness plate. Seven out of 10 devices with a 2" diameter acceptor produced a hole or completely broke the witness plates. Three of the four devices where the test mixture was a detonable NM/NA mixture produced flat witness plates; the fourth one in this series that made a hole was a 12" long device. It appears using the larger (2") acceptor did not improve the device. From the evidence that one 12" long device created a hole in the witness plate even though the center test material was detonable, strongly suggests that the flyer pipe configuration is failing to cause complete initiation of a 2" diameter test material. Boosters of two outer diameters (O.D.), 4" and 6", were used. Total volume of nitromethane/nitric acid in each was 689 mL for 4" O.D. and 1558 mL or 2008 mL for 6" O.D., for device 3a and 2a, respectively. In general, switching from a 4" O.D. to a 6" O.D. resulted in more damage to the witness plate. However, in a test using a detonable NM/NA acceptor (shot 7), a flat witness plate with an undisturbed center region was produced using the 4" booster, but with an identical shot using a 6" O.D. booster (shot 27) resulted in a sizable hole indicating no detonation from the most detonable material used as an acceptor. The discussion above and the comparison of shots 19 and 36 (12" length; 2" NM/NA acceptor; 6" O.D. booster), the results of shots 27 and 7 (4" length, 1" NM/NA acceptor; 6" O.D. and 4" O.D. booster, respectively, 2.03" I.D. flyer pipe) both suggest the flyer pipe was not initiating the acceptor material.



Way Forward:

In trying to understand why some of the plates had a flat, undisturbed central section, Stewart's models were reviewed. As expected, there was a lag between the exit of detonation products from the booster and when the jet/detonation products exit the acceptor. With increased gap used in the actual tests we expect an increased lag between booster/acceptor exiting the device. In previous test series where the booster was in direct contact with the acceptor, there was no delay; without a delay the detonation products from the booster may have acted as a guide for the jet formed by the acceptor, not allowing jet to stray sideways or disintegrate.

Screen Capture of Stewart's model illustrating lag. The detonation products of the booster explosive are depicted in blue, the aluminum flyer pipe is orange; pink represents PVC; yellow is water. The time differential between detonation products of the booster exiting the device and the beginning of the water jet exiting is about 5 time units.

When the detonation products from the booster escape earlier than the acceptor material, this guidance effect would be lacking. With the flyer pipe configuration, is it possible the jet would be more likely to reach maximum velocity then begin to disintegrate before reaching the witness plate. At this point, there are too many variables in designing the test fixture to proceed without further modeling. That will comprise the bulk of this work in the near future.

Test Series 5 Experimental Details

Devices in 10 different configurations were constructed. Variables included length of the device, diameter of the booster and of the acceptor, flyer pipe wall thickness and gap to acceptor.

Table 5: Device Configurations

Length (")	Acceptor Diam (")	Booster Diam (")	Flyer ID (mm)	Flyer OD (mm)	Flyer Wall Thickness (mm)	M/C (Calc'd)	V _{flyer} (m/s) (Calc'd)	Pressure @ Impact (GPa) (Calc'd)	Test Config #
4	1	4	51.6	56.1	2.3	0.15	3235	16	1a
4	1	6	51.6	55.2	1.8	0.04	3955	22	2a
4	1	6	77.5	87.8	5.2	0.24	2918	14	3a
4	2	6	77.5	80.5	1.5	0.06	3675	19	4a
4	2	6	77.5	82.6	2.6	0.11	3423	17	5a
12	1	4	51.6	56.1	2.3	0.15	3235	16	1b
12	1	6	51.6	55.2	1.8	0.04	3955	22	2b
12	1	6	77.5	87.8	5.2	0.24	2918	14	3b
12	2	6	77.5	80.5	1.5	0.06	3675	19	4b
12	2	6	77.5	82.6	2.6	0.11	3423	17	5b



Photo 1: From left to right, top to bottom: Configurations 3a, 1a, 2a, 5a, 4a.

Shot setup with 10" S.O.

1) Length of the device (4" vs 12")

Nine 12" long, 1" diameter acceptor devices with either 4" or 6" outer diameter devices were used (Table 6). All but one produced a flat witness plate. Either a) all acceptor materials detonated, including shot 29 of brine (unlikely); or b) the materials didn't detonate but the witness plates were too far away to be affected by the liquid jet; or c) the jet was killed outside the device before it reached the witness plate.

Supporting hypothesis 1b, one device, 12" in length, 1" acceptor, 6" booster (shot 34) made a hole in the plate with a brine acceptor, but instead of 10" stand-off, it was 6". This observation could mean the other 8 devices were too far from the witness plate, but a second device (shot 35) also 6" from the witness plate also gave a flat witness plate (1" acceptor of TM-C, 4" booster). Supporting hypothesis 1c is a comparison of devices differing only in length of the device: e.g. shot 28 hole vs. 29 nearly flat; shot 6 hole vs. 14 flat; shots 11 & 12 hole vs. 10 & 15 flat. In all cases where the acceptor was 1" in diameter, a hole was produced by the 4" long device, but at the same stand off the 12" long device gave a flat witness plate, strongly suggesting the reaction was quenched in the device. From the photos, the plates were seemingly untouched in the center area of the witness plate for all 12" length devices, except shot 34 which resulted in multiple fragments of the witness plate. A completely untouched center region was also observed for shot 7, which was a 4" booster, 4" length, with NM/NA as the acceptor (Photo 2).



Photo 2: Shots labeled left to right with acceptor material indicated

Shots 28 (brine) 29 (brine) 6 (TM-C) 14 (TM-C) 7 (NM/NA)

Out of four 12” long devices with 2” diameter acceptors, 3 produced holes including one which contained the detonable NM/NA (shot 19) booster material. Although witness plates were still 10” away, there was more material to jet into the witness plate. The one 12” long device with 2” acceptor (shot 36) which produced a flat witness plate also contained NM/NA in the acceptor. However, a detonator interrupter was not used in this one shot; therefore, the acceptor was likely initiated directly by the sheet explosive; the witness plate was undisturbed in the center region. This observation suggests that the flyer pipe did not provide sufficient impulse to cause a detonation, even of a known detonable material.

Photo3: Shots (left to right with acceptor material) 19(NM/NA) & 36(NM/NA)



Table 6: Effect of Device Length & Standoff

Shot #	Length (")	Acceptor Diam (")	Booster Diam (")	S.O. (")	Acceptor Mix	Config	Dent Depth (")
28	4	1	6	10	brine	2a	1.08
29	12	1	6	10	brine	2b	0
34	12	1	6	6	brine	2b	>2
1	4	1	4	12	C	1a	0
6	4	1	4	10	C	1a	0.41
14	12	1	4	10	C	1b	0
35	12	1	4	6	C	1b	0
2	4	1	6	12	C	2a	0.73
11	4	1	6	10	C	2a	0.86
3	4	1	6	12	C	3a	0.51
12	4	1	6	10	C	3a	0.69
15	12	1	6	10	C	2b	0
10	12	1	6	10	C	3b	0
27	4	1	6	10	NM/NA	2a	0.73
30	4	1	6	10	NM/NA	3a	0
23	12	1	6	10	NM/NA	3b	0
25	4	2	6	10	B	5a	>2
18	12	2	6	10	B	5b	1.32
8	4	2	6	10	C	4a	1.28
4	4	2	6	12	C	4a	>2
5	4	2	6	12	C	5a	>2
16	12	2	6	10	C	5b	>2
9	4	2	6	10	NM/NA	4a	0
37	4	2	6	10	NM/NA	5a	0
19	12	2	6	10	NM/NA	5b	0.77
36	12	2	6	10	NM/NA	4b	0

* - Yellow highlighted indicates 12” length devices.

2) Diameter of the acceptor (1" vs. 2")

Seven out of 10 devices with a 2" diameter acceptor produced a hole or completely broke the witness plates, but 3 of the four devices with NM/NA (a detonable acceptor, shots 9, 37, 36) produced flat witness plates. Shots 9 and 37 were 4" length devices (Table 7). Shot 36 was a 12" long device which gave a flat plate, but a detonator interrupter was not used (Table 6); shot 19 was similarly configured (12" long; 2" acceptor, 6" booster), but with an interrupter and produced a hole in the witness plate. Comparing 4" length devices with 1" or 2" acceptors, it appears using the larger acceptor did not improve the device (Table 7).



Photo 4: From left to right: Shot 9, Shot 37, Shot 36 (NM/NA Acc.)

Table 7: Comparison of 1" vs. 2" acceptors

Shot #	Length (")	Acceptor Diam (")	Booster Diam (")	S.O. (")	Acceptor Mix	Config	Dent Depth (")
27	4	1	6	10	NM/NA	2a	0.73
30	4	1	6	10	NM/NA	3a	0
9	4	2	6	10	NM/NA	4a	0
37	4	2	6	10	NM/NA	5a	0
31	4	1	6	10	A	3a	0.53
33	4	2	6	10	A	4a	>2
32	4	2	6	10	A	5a	1.93
26	4	1	6	10	B	2a	0.78
25	4	2	6	10	B	5a	>2
2	4	1	6	12	C	2a	0.73
3	4	1	6	12	C	3a	0.51
12	4	1	6	10	C	3a	0.69
11	4	1	6	10	C	2a	0.86
8	4	2	6	10	C	4a	1.28
4	4	2	6	12	C	4a	>2
5	4	2	6	12	C	5a	>2
22	4	1	6	10	NM	2a	0.9
28	4	1	6	10	brine	2a	1.08
1	4	1	4	12	C	1a	0
6	4	1	4	10	C	1a	0.41

3) Comparing the Effect of Booster Size

Boosters of two outer diameters (O.D.), 4" and 6," were used. Total volume of nitromethane/nitric acid in each was 689 mL for 4" O.D. and 1558 mL or 2008 mL for 6" O.D., for device 3a and 2a, respectively.

In general, switching from a 4" O.D. to a 6" O.D. resulted in more damage to the witness plate. For example, among 4" length devices, the largest hole observed in the witness plate of 4" O.D. boosters was 0.60", while for the 6" O.D. devices the minimum hole in the witness plate was 0.73". Two comparisons bear more study; these were 4" long devices with 1" acceptors and 4" or 6" O.D. boosters-- shots 17 vs. 26 (TM-B) and shots 7 vs. 27 (NM/NA) (Table 8). For TM-B, a very slight dent was observed for the 4" O.D. booster (shot 17), whereas a considerable dent was formed for the 6" O.D. booster (shot 26). Shot 7, which contained detonable NM/NA in the acceptor, resulted in a flat plate with an undisturbed center region, while an identical shot using a 6" O.D. booster (shot 27) resulted in a sizable hole indicating no detonation from the most detonable material used as an acceptor.



Photo 5: Shots 17 & 26 (TM-B Acc.), Shots 7 & 27 (NM/NA Acc.)

Table 8: Effect of Booster Size 4" O.D. vs. 6" O.D.

Shot #	Length (")	Acceptor Diam (")	Booster Diam (")	S.O. (")	Acceptor Mix	Config	Dent Depth (")
13	4	1	4	10	brine	1a	0.6
28	4	1	6	10	brine	2a	1.08
1	4	1	4	12	C	1a	0
6	4	1	4	10	C	1a	0.41
2	4	1	6	12	C	2a	0.73
11	4	1	6	10	C	2a	0.86
3	4	1	6	12	C	3a	0.51
12	4	1	6	10	C	3a	0.69
17	4	1	4	10	B	1a	0.22
26	4	1	6	10	B	2a	0.78
7	4	1	4	10	NM/NA	1a	0
27	4	1	6	10	NM/NA	2a	0.73
30	4	1	6	10	NM/NA	3a	0
20	12	1	4	10	70	1b	0
21	12	1	6	10	70	3b	0.38
14	12	1	4	10	C	1b	0
35	12	1	4	6	C	1b	0
15	12	1	6	10	C	2b	0
10	12	1	6	10	C	3b	0

4) Effect of Flyer Pipe

The comparison of shots 19 and 36 (Table 5: 12" length; 2" NM/NA acceptor; 6" O.D. booster), the results of shots 27 and 7 (Table 7; 4" length, 1" NM/NA acceptor; 6" O.D. and 4" O.D. booster, respectively, 2.03" I.D. flyer pipe) both suggest the flyer pipe was not initiating the acceptor material. Shot 36 (NM/NA acceptor) was a 12" long device which gave a flat plate, but it did not use a detonator interrupter; in fact, shot 19 was similarly configured (12" length; 2" NM/NA acceptor, 6" booster), but with an interrupter and it produced a hole in the witness plate (Table 6). Table 8 shows 4" length devices with 1" acceptors and 4" or 6" O.D. boosters. Shots 7, 27 and 30 all had NM/NA as the acceptor. Shot 7, a 4" O.D. booster gave a flat, undisturbed center region plate; shot 27, a 6" O.D. booster with a 2" flyer pipe gave a dent, while shot 30, a 6" O.D. booster with a 3" flyer pipe gave a flat plate (center section pitted) (Table 8). However, shot 30 leaked out of the booster in between the flyer pipe and the acceptor pipe; therefore, the results may or may not be accurate.



Photo5: L→R: Shots 36, 19, 30(NM/NA Acc.) Photo6: L→R: Shots 24 (Empty Acc), 17(TM-B Acc), 6(TM-C Acc)

5) Flyer Pipe Damage

Damage to the witness plate was a result of jetting of undetonated material; plastic fragments from the pipe walls and the base plates; and fragments of aluminum from the flyer pipe. Our focus to this point has been on damage to the witness plate caused by the un-reacted acceptor material. However, in all test series, this one included, the plates have been pocked marked which we assume was a result of plastic fragment. Shot 24, 4" length, 4" O.D. was shot with an empty 1" acceptor pipe with a detonator interrupter in it. This resulted in a hole in the witness plate greater than or equal to similarly configured devices with TM-B (shot 17) or TM-C (shot 6). With an empty acceptor pipe, this is not a true blank; the acceptor pipe would collapse and be driven down, along with the flyer pipe into witness plate. All 12" length, 6" O.D. booster, 3" flyer pipe, 1" acceptor (configuration 3b), showed pitting of the central region; the other 12" length devices at 10" stand-off gave plates with undisturbed center regions. The mass of the flyer pipe is not insignificant (Table 9). Damage to the witness plate stands to reason.

Table 9: All Devices

Shot #	Length (")	Acc. Diam (")	Booster Diam (")	Flyer ID (")	Flyer Wall Thickness (mm)	Flyer Pipe Mass (g)	V _{flyer} (m/s) (Calc'd)	Pressure @ Impact (GPa)	S.O. (")	Acceptor Mix	Test Config #	Dent Depth (")	
17	4	1	4	2.030	2.3	102	3235	15.81	10	B	1a	H	0.22
13	4	1	4	2.030	2.3	101	3235	15.81	10	Brine	1a	H	0.60
1	4	1	4	2.030	2.3	96	3235	15.81	12	C	1a	F	0.00
6	4	1	4	2.030	2.3	97	3235	15.81	10	C	1a	TH	0.41
24	4	1	4	2.030	2.3	112	3235	15.81	10	MT	1a	H	0.41
7	4	1	4	2.030	2.3	101	3235	15.81	10	NM/NA	1a	F	0.00
31	4	1	6	3.050	5.2	364	2918	13.52	10	A	3a	D	0.53
26	4	1	6	2.030	18	83	3955	21.56	10	B	2a	H	0.78
28	4	1	6	2.030	18	80	3955	21.56	10	Brine	2a	H	1.08
2	4	1	6	2.030	18	77	3955	21.56	12	C	2a	D	0.73
11	4	1	6	2.03	18	83	3955	21.56	10	C	2a	H	0.86
3	4	1	6	3.050	5.2	369	2918	13.52	12	C	3a	D	0.51
12	4	1	6	3.050	5.2	361	2918	13.52	10	C	3a	H	0.69
22	4	1	6	2.030	18	76	3955	21.56	10	NM	2a	H	0.90
27	4	1	6	2.030	18	74	3955	21.56	10	NM/NA	2a	H	0.73
30	4	1	6	3.050	5.2	366	2918	13.52	10	NM/NA	3a	F	0.00
33	4	2	6	3.050	15	101	3675	19.24	10	A	4a	B	>2
32	4	2	6	3.050	2.6	169	3423	17.25	10	A	5a	H	1.93
25	4	2	6	3.050	2.6	173	3423	17.25	10	B	5a	B	>2
8	4	2	6	3.050	15	100	3675	19.24	10	C	4a	H	1.28
4	4	2	6	3.050	15	96	3675	19.24	12	C	4a	B	>2
5	4	2	6	3.050	2.6	168	3423	17.25	12	C	5a	B	>2
9	4	2	6	3.050	15	97	3675	19.24	10	NM/NA	4a	F	0.00
37	4	2	6	3.050	2.6	193	3423	17.25	10	NM/NA	5a	F	0.00
20	12	1	4	2.030	2.3	303	3235	15.81	10	70% HP	1b	F	0.00
14	12	1	4	2.030	2.3	316	3235	15.81	10	C	1b	F	0.00
35	12	1	4	2.030	2.3	303	3235	15.81	6	C	1b	F	0.00
21	12	1	6	3.050	5.2	1097	2918	13.52	10	70% HP	3b	F	0.00
29	12	1	6	2.030	18	212	3955	21.56	10	Brine	2b	F	0.00
34	12	1	6	2.030	18	254	3955	21.56	6	Brine	2b	B	>2
15	12	1	6	2.030	18	233	3955	21.56	10	C	2b	F	0.00
10	12	1	6	3.050	5.2	1104	2918	13.52	10	C	3b	F	0.00
23	12	1	6	3.050	5.2	1101	2918	13.52	10	NM/NA	3b	F	0.00
36	12	2	6	3.050	1.5	354	3675	19.24	10	NM/NA	4b	F	0.00
19	12	2	6	3.050	2.6	468	3423	17.25	10	NM/NA	5b	H	0.77
16	12	2	6	3.050	2.6	491	3423	17.25	10	C	5b	B	>2
18	12	2	6	3.050	2.6	488	3423	17.25	10	B	5b	B	1.32

NM/NA > TM-A > TM-B > TM-C > 70% HP >> brine
 Detonable > 70wt% HP w/ 13.6wt% EtOH > 50wt% HP w/ 10.7wt% EtOH > 50wt% HP w/ 4.8wt% EtOH > non-detonable

Graduate Students:



Pat Bowden



Ryan Rettinger



Devon Swanson



Jon Canino

X-ray Bottle Screener Simulant Project
Jimmie Oxley; James Smith; Austin Brown
University of Rhode Island
with Lou Wainwright AS&E

Objective

The goal of this project is to develop non-hazardous liquids which to x-ray detection instrumentation simulate hazardous (explosive) liquids. These simulants can be used in locations where the actual explosives cannot, e.g. vendors' facilities, airports, personnel training.

Background

X-ray scanner response to a compound is based on density (ρ) and effective atomic number (Z_{eff}) of the sample as well as several constants related to the energy of the x-ray used for the scan (eq 1).

$$\text{X-ray response} = \text{gain} * (\rho * Z_{\text{eff}}) + \text{offset} \quad (1)$$

The development of simulants for x-rays has focused on creating a liquid that matches both the density and Z_{eff} of the hazardous liquid. The problem with this approach is that it is challenging to match these values, and more importantly the match is only good for the x-ray energy level for which it was created.

Approach

To approach this difficult problem URI formed a partnership with AS&E. URI provided the manpower; AS&E provided a Scatter Attenuation Tomography (SAT) tabletop bottled liquid scanner, a 50 keV x-ray detector and initial guidance. Based on many actual samples, AS&E believed that Z_{eff} could be calculated with the following formula:

$$Z_{\text{eff}}(E) = \{\Sigma [(f_H * Z_H^4) + (f_O * Z_O^4) + (f_C * Z_C^4) + (f_N * Z_N^4) + \dots]\}^{1/4} \quad (2)$$

where atomic number (i.e. # protons) of the elements involved are raised to the 4th power and the f-coefficients are related to the fraction of protons of a given element compared to the total protons available in a sample.

[Theoretically, the exponent should be 3 (for 3-dimensional space); and Wikipedia claims it is 2.94 (http://en.wikipedia.org/wiki/Effective_atomic_number).]

The SAT numbers identify a substances from the response of two detectors originally thought to be modeled by the following equations:

$$\text{SAT}_{\text{HE}} = (\rho * Z_{\text{eff}}) * 0.091 + 0.0017 \quad (3)$$

$$\text{SAT}_{\text{LE}} = (\rho * Z_{\text{eff}}) * 0.1661 - 0.1798 \quad (4)$$

Experiments were conducted to evaluate the accuracy of equation 2 in prediction of effective atomic number. They are summarized below as follows:

1. The SAT numbers of hydrogen peroxide (HP) concentrations (30wt% to 90wt%) were determined. Fifty runs at 11 different concentrations were collected and the data is presented in Figure 1 showing variations in instrument response.
2. Equations 2, 3 and 4 were used to calculate the theoretical instrument response for a number of liquids which are compared to instrument measurements of liquids in Figure 2. The SAT numbers diverged widely from theoretical values; this was ascribed to errors in the theoretical gain and offset values indicated in Equations 1, 3 and 4.

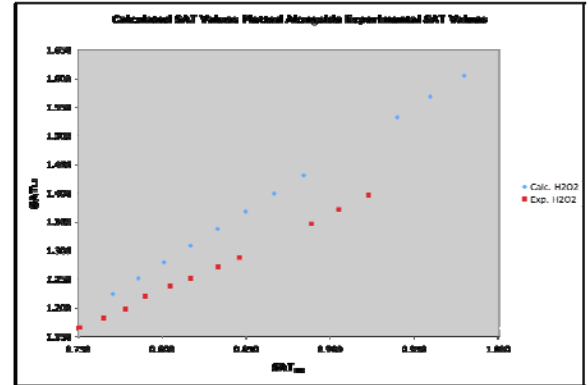
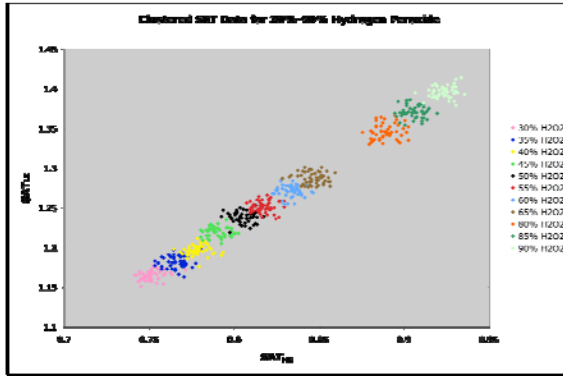


Fig. 1 SAT number with multiple runs of HP sample Fig. 2 Actual vs calculated by eq 3& 4 SAT numbers

3. Next we attempted to make simulants using a combination of sucrose and ZnSO_4 solutions to match the density and Z_{eff} for various concentrations of hydrogen peroxide (HP), assuming any error in the constants (equations 3 & 4) would cancel out. Figure 3 illustrates that this approach was flawed; thus, it was decided the exponent in equation 2 was not 4.

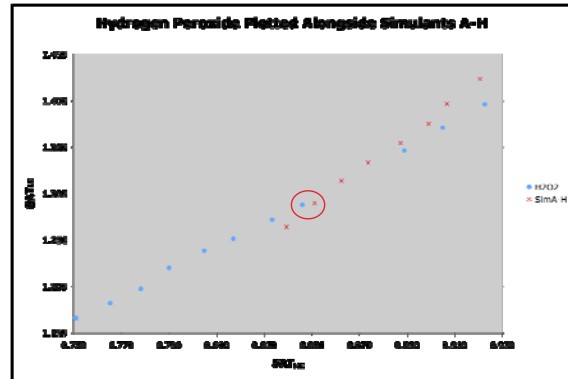
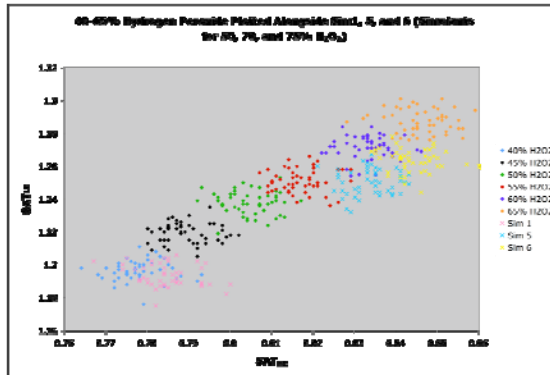


Fig.3 Simulants by approach 3 vs HP solutions

Fig. 4 Simulants by approach 4 vs HP solutions

4. AS&E had already questioned whether 4 was the correct exponent to use in Equation 2; we used our data to determine a more correct exponent. Z_{eff} was recalculated for all experimentally gathered data using Z_{eff} exponents ranging from 3-4 in increments of 0.01. The exponent determined for Z_{eff} SAT_{LE} was 3.23 and the exponent for Z_{eff} for SAT_{HE} was 3.30. The average value of 3.27 was used as the exponent in equation 2.

Unfortunately, a good match was not obtained for all solutions. Since the densities were matched, it was assumed that the Z_{eff} exponent was still the problem.

5. Z_{eff} exponents are not the same for high energy and low energy x-rays. Equation 5 takes into account that the n exponents are energy dependent leading to a more accurate description than equation 2.

$$Z_{\text{eff}}(E) = \{ \Sigma [(f_H * Z_H^{n(E)}) + (f_O * Z_O^{n(E)}) + (f_C * Z_C^{n(E)}) + (f_N * Z_N^{n(E)}) + \dots] \}^{1/n} \quad (5)$$

Z_{eff} was recalculated for all experimentally gathered data using Z_{eff} exponents ranging from 3-4 in increments of 0.01. Both high (HE) and low energy (LE) plots were prepared for each data set. This involved the creation of two hundred plots; two examples are shown in Figure 5. Essentially, the formula assumed is that

$$\text{SAT \#} = \text{gain}(\rho * Z_{\text{eff}}) + \text{offset}$$

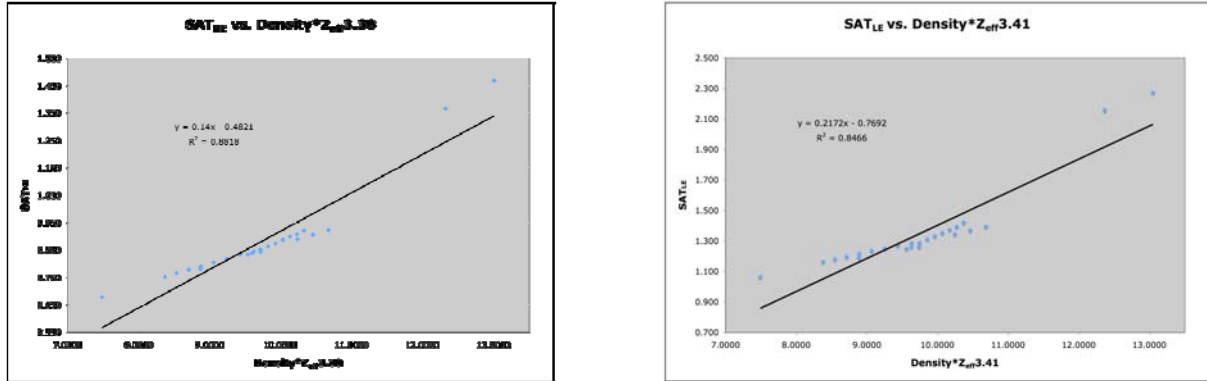


Fig. 5 High (left) and Low (right) Energy SAT values vs Density * Z_{eff} product with best exponent by approach 5

6. To achieve a better fit than attained by method 5, a new form of the equation was necessary. AS&E suggested that even the instrumental response to density and Z_{eff} varies with the energy of the x-ray, which could be expressed as follows:

$$\text{X-ray response} = \text{Gain}(E) * (\text{Density}^{C1(E)} * Z_{\text{eff}}^{C2(E)}) + \text{Offset}(E) \quad (6)$$

Solutions of constant density but varying Z_{eff} were prepared. Using equation 7 various iterations were tried to find the optimum Z_{eff} and $C2(E)$. The exponent $C1(E)$ for density could then be found for high and low energy.

$$\text{Ln}(\text{SAT}) = C2(E) * \text{Ln}(Z_{\text{eff}}) + \text{constant} \quad (7)$$

Where constant = $\text{ln}(\text{OffsetE}) + \text{ln}(\text{GainE}) + C1(E) * \text{ln}(\text{Density})$

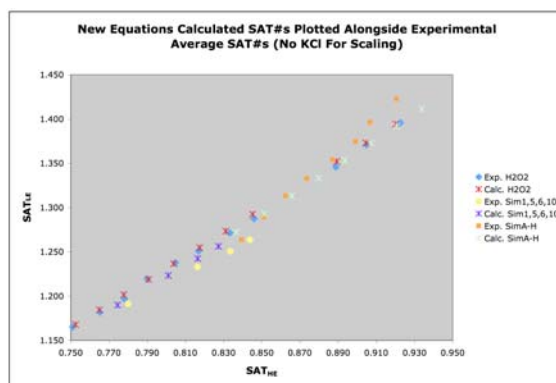


Fig. 7 SAT's calculated from eq 6 (calc.) & experimental (exp) for H₂O₂ & simulant solutions

7. The formula developed worked satisfactorily for hydrogen peroxide solutions but not for other hazardous solutions, e.g. sulfuric acid. Thus, we temporarily abandoned developing the theoretical model and took a top down approach to simulant development.

Simulant Development

The innocuous materials used to develop simulants were organic liquids with low density and inorganic salts: KBr, BaCl₂, KI, sugar, methanol, propanol and acetone. The low-density organic liquids were used to reach SAT numbers lower than water. Inorganic salts were used to simulate SAT numbers higher than those for water because they covered the widest possible range due to their large Z_{eff} .

Nitrobenzene (NB) was our first choice to simulate since we had samples in the lab to absolutely benchmark our results. Since nitrobenzene had SAT numbers lower than water several concentrations of aqueous methanol, 2-propanol, and acetone were run through the bottle screener. Average SAT numbers from 50 scans are plotted below (Fig. 8). When trend lines were fit to the plot of Ave SAT_{LE} vs. Ave SAT_{HE} to see if any concentration of these liquids would work as a simulant, it was noticed that the trend lines for aqueous acetone and 2-propanol intersected near water (red circle, Fig. 9). This led to the idea that water could be thought of as the origin of the trend lines representing a concentration of 0%. This was also true for aqueous solutions having higher SAT numbers than water (KBr, BaCl₂, and KI).

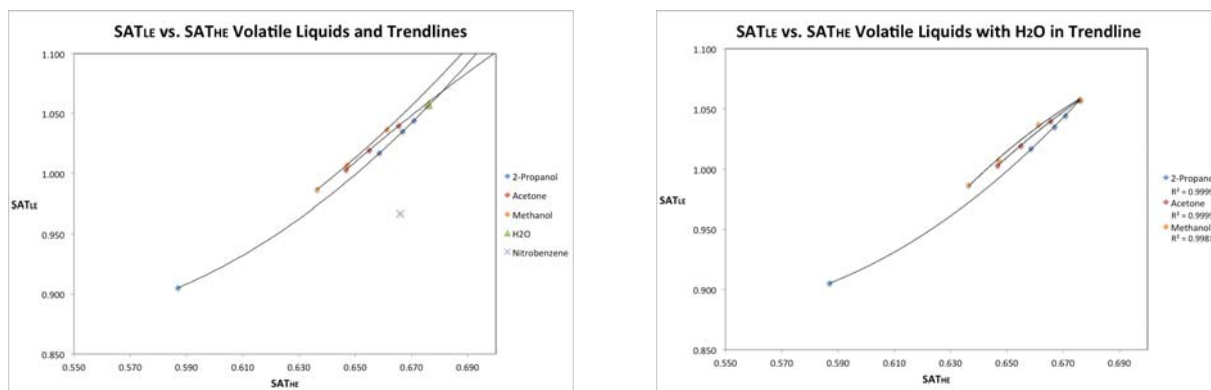


Fig. 8a SAT trendlines of organics with SAT < NB Fig 8b SAT trends of aqueous solution intersect at H₂O

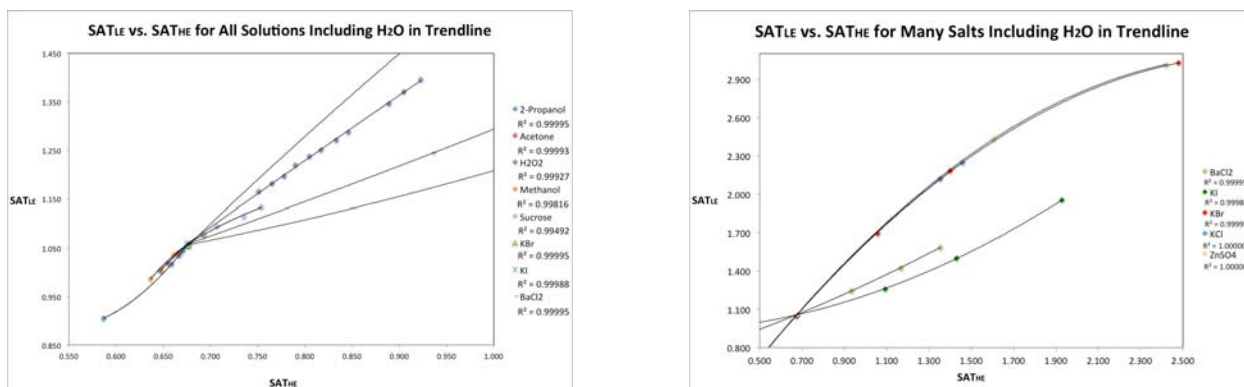


Fig 9: SAT trendlines originating from water for many aqueous solutions

It was observed that the SAT trendlines for many aqueous solutions intersected at the SAT of water (i.e. 0% solution). This observation led to the theory that when two aqueous solutions were mixed the SAT number trendlines would stack on one another with the origin of one component shifting from the SATs of water to the SATs the other component. Figure 10 shows the shift in SAT numbers when a BaCl_2 is mixed into a 40% 2-propanol solution. [The trendline for a BaCl_2 solution shifts its lower end from the SATs for water to the SAT of the appropriate concentration of propanol (40%).] This being the case a simulant for nitrobenzene was proposed that had origin SAT numbers lower than water from 2-propanol with barium chloride to shift the SAT numbers to match those of nitrobenzene.

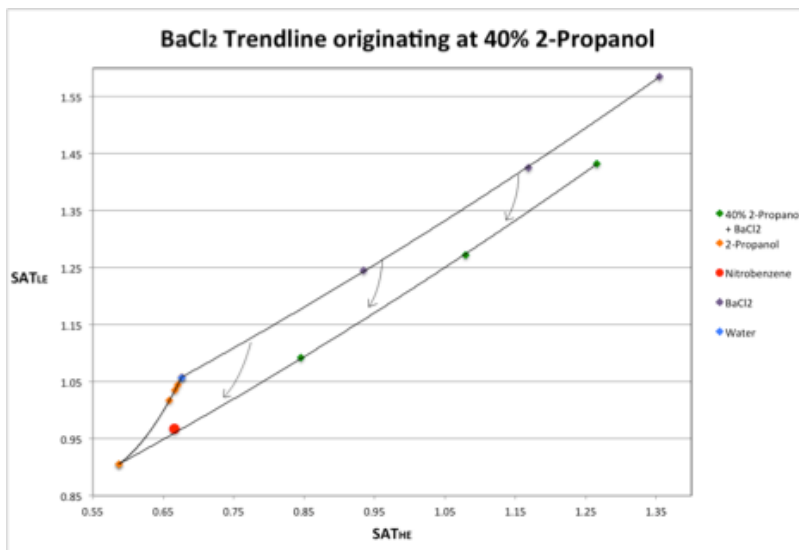
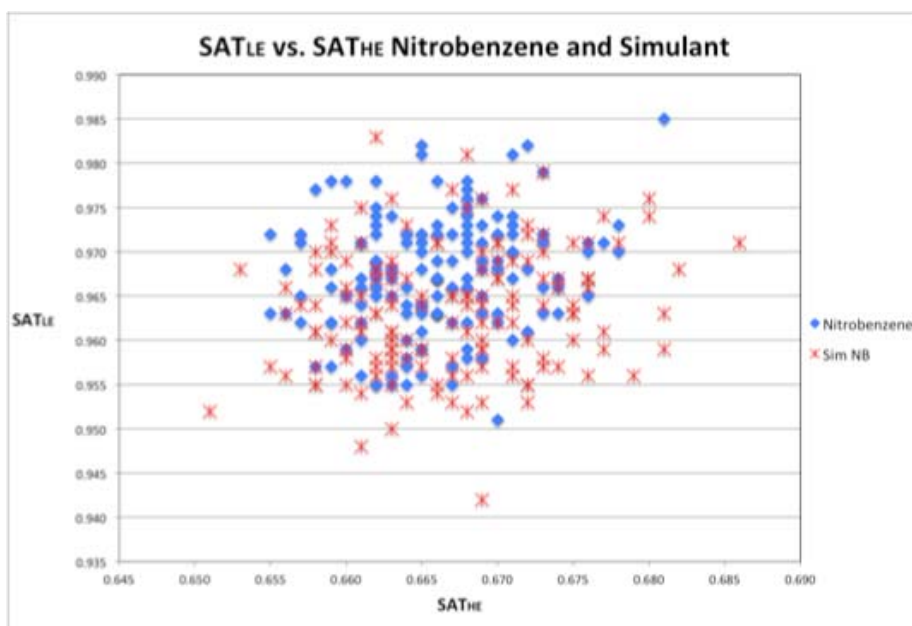


Fig 10: BaCl_2 SAT trendline shifted from origin of water to propanol passing through nitrobenzene SATs.

Based on Figure 10 a solution of approximately 40% 2-propanol was prepared with 0.2% barium chloride to act as a simulant for nitrobenzene. The solution was run and adjusted several times until the final simulant had a concentration of 40.1% 2-propanol and 0.3% barium chloride. Figure 11 illustrates that a successful simulant for nitrobenzene was made.



Way Forward

We plan to develop a mathematical formula to remove the visual guesswork from the graphical method described above. It may be possible to use a computer fitting program. Eventually, we hope to revisit equation 6 with the goal of developing a predictive tool for designing a simulant for any X-ray detection system.

Students



Austin Brown



Morgan Turanto



Sravanthi Vadlamannati

The simulants created thus far were not created by focusing on the density or Z_{eff} but instead on the instrument response to the individual components of the simulant. The two simulant components, barium chloride (BaCl_2) and potassium bromide (KBr), were chosen because BaCl_2 increases the high energy signal more than the low energy signal while KBr increases the low energy signal more than the high energy signal. By varying

the concentration of each component a wide range of responses can be simulated. Using this method simulants have been created for hydrogen peroxide (60%, 65%, 80%, 85%, and 90%), nitric acid (40%, 50%, 60%, and 70%), and nitrobenzene. Unfortunately due to the dependence of Z_{eff} on the energy of the x-ray these simulants only apply to the 50kV AS&E bottle screener. The current simulant development method has proven to be quite accurate but as it can only provide simulants for a specific instrument, and only then after running many samples both hazardous and benign through that instrument, a more comprehensive simulant development method is needed.

The first step to creating simulants for other x-ray systems is understanding how x-ray energy is related to the Z_{eff} exponent. If the Z_{eff} exponent can be predicted based on the energy of the x-ray system the simulant development method of matching the density and Z_{eff} of a hazardous solution becomes an option. The ultimate goal of this project is to develop a theoretical model that can be used to create simulants for hazardous solutions based on density, the energies of the x-rays in a system, and Z_{eff} at those energies. This would not only allow for simulants to be developed without requiring access to the instrument, but also make it possible to create a simulant for a hazardous solution without ever having to work with the hazardous solution itself.

Theoretical Projects within the Center of Excellence

Ronnie Kosloff; Yehuda Zeiri
Hebrew University Jerusalem, Israel

I. Objective

The goal is to establish and apply theoretical methods that will be able to predict the sensitivity and detonability of energetic materials. This is in response to the proliferation of the threat of improvised explosives and the growing threat of the proliferation of military type explosives. The list of threats has increased substantially. As a result it becomes very difficult and time consuming to study each of the variants experimentally. We therefore want to establish a comprehensive theoretical modeling protocol which will be able to predict the hazard of new materials. We want to calculate physical properties such as spectrum, density and energetics. Finally we intend to suggest methods to dispose safely such materials.

II. Accomplishments

We published a comprehensive study of the properties of the decomposition of liquid Nitromethane. Our study employed reactive (REAXFF) molecular dynamics simulations under various conditions of constant temperature and compression. We have identified a change of mechanism of decomposition between low and high density. In low density at elevated temperatures the first step in decomposition is the breakup of the nitrogen carbon bond. At high density there is a transition to bimolecular reaction with a proton transfer. This may explain the large difference between detonation in liquid and solid form of Nitromethane. This study is an important step in establishing a computational method for predicting the initiation and detonation properties of liquid explosives. We are currently extending these studies to liquid TNT.

We have published an extensive theoretical study on the disposal of TATP. This study is in collaboration with the experiments carried out of URI. The theory calculates the properties of ion TATP complexes with the purpose to identify a catalyst for safe disposal. We suggest an additional role of high ion concentrations as a means to screen van der Waals forces and allow dissolution of TATP.

III. Details

Decomposition of Nitromethane under the influence of temperature & compression.

Work of Dr. Naomi Rom

Nitromethane (H_3CNO_2 , NM), a high explosive (HE), has been studied intensively both experimentally, decomposition reactions were characterized using ab initio MD simulations and theoretically. These studies were carried out starting with a crystal or liquid phase. Our study focuses on reactive molecular dynamics (MD) simulations of NM in the hot and dense liquid phase. The main goal of the study was to identify and quantify the detailed chemical reactions that occur during detonation. These reactions initiate with the first molecular decomposition steps followed by the creation of final products. The calculations were performed under various temperature and compression conditions. These conditions simulate rapid laser heating experiments in diamond anvil cells, where the sample volume is held constant. The purpose of the study was to obtain insight on the reaction mechanisms governing the initiation and detonation process. The temperatures and compressions range examined include the conditions at the detonation wave front. Nitromethane is the most simple model of a nitro type liquid explosive. The understanding of its reaction mechanism will lead to understanding of other more complex liquid explosives such as liquid TNT. Currently we are working on the decomposition routes of TNT.

A sample of the possible NM unimolecular decomposition pathways suggested are:

- $\text{CH}_3\text{NO}_2 \rightarrow \text{CH}_3 + \text{NO}_2$
- $\text{CH}_3\text{NO}_2 \rightarrow \text{CH}_3\text{ONO} \rightarrow \text{CH}_2\text{O} + \text{HNO}$
- $\text{CH}_3\text{NO}_2 \rightarrow \text{CH}_3\text{NO} + \text{O}$
- $\text{CH}_3\text{NO}_2 \rightarrow \text{CH}_3\text{O} + \text{NO}$
- $\text{CH}_3\text{NO} \leftrightarrow \text{CH}_2\text{NOH}$
- $\text{CH}_3\text{NO}_2 \rightarrow \text{CH}_2\text{NOOH}$

The decomposition of solid NM was calculated using MD simulations with on-the-fly calculations of molecular forces with density functional theory. In these simulations, dense solid NM (1.97 g/cm^3 and 2.2 g/cm^3) was rapidly heated to 3000K and 4000K. The first step revealed in the thermal decomposition was *inter-molecular* proton transfer forming $[\text{H}_3\text{CNO}_2\text{H}]^+$ and aci ion $[\text{H}_2\text{CNO}_2]^-$. The second step observed was *intra-molecular* proton transfer forming aci acid $[\text{H}_2\text{CNO}_2\text{H}]$. Then, additional fragments were formed, such as: CH_2NO^+ , OH^- and H_2O . These reaction products were related to condensed phase reactions, whereas C-N bond break, being the weakest in the molecule ($D_0=60.1 \text{ kcal/mol}$ in the gas phase), prevails in gas phase or dilute fluid decomposition.

The hypothesis that hydrogen abduction is the rate determining step at pressure of 10 kbar and at temperature of 273°C , is supported by the measured time to detonation with deuterated NM which was found to be 10 time longer than with protonated NM **Error! Reference source not found.** However, interpolation to higher temperatures suggests that above 330°C the time to denotation of NM is shorter than that of deuterated NM. Thus, possibly H-transfer is more important at similar compressions and lower temperatures ($<330^\circ\text{C}$).

, the effect of pressure ($< 7 \text{ GPa}$) on thermal **Error! Reference source not found.**In decomposition of NM was studied in diamond anvil cell experiments where the samples were heated up to 450K. It was found that both pressure and temperature accelerate the rate of thermal decomposition, supporting a bi molecular decomposition mechanism. The suggested rate-controlling leading reaction, supported by quantum mechanical calculation, is:



with calculated activation energy of 32.5 kcal/mol

In the present study, we applied a MD approach based on the reactive force field REAXFF to study the decomposition of liquid NM at a wide range of compression values ($0.56 \leq V/V_0 \leq 1$) and temperatures (2500K-4500K). Three regimes of the reaction are identified and analyzed independently: Initiation step, intermediate reactions, and stable products creation. We found that the mechanism of the initial, rate determining step in NM decomposition depends strongly on its density (ρ): At ambient density and below 30% compression, C-N bond breakage is the first event, as in the gas phase. At higher densities, in the vicinity of the Chapman-Jouget (CJ) state (stationary detonation, fully reacted HE, products in chemical equilibrium), CH_3NO is the dominant initial decomposition product. The former process is unimolecular whereas the latter fragment is formed by various mechanisms.

Thermal rate constants were evaluated for the initial, endothermic decomposition stage for different initial densities. After some delay (temperature and pressure dependent), various intermediate reactions commence, including autocatalytic ones where NM reacts with its fragments. These reactions are presented in details in section **Error! Reference source not found.** The evolution of final products (H_2O , CO_2 , N_2 , H_2 , CO and OH) begins in the intermediate stage and ends when they reach stable amounts.

We are currently establishing a simulation of the thermal decomposition of TNT. This study is based on our experience in nitromethane. Our goal is to determine the activation energy of decomposition and the major reactions that take place. Figure 1 shows the change in potential energy of TNT as a function of time for different temperatures. These simulations were

carried out for liquid TNT at ambient pressure. The simulation sample included 80 molecules in a cell with periodic boundary conditions. Figure 2 shows the decomposition percentage as a function of time for different temperatures. From this data we can obtain the activation energy of decomposition to be 45Kcal/mol. This value is much lower than the gas phase value of 70Kcal/mol. Fig 3 shows the stable products of the decomposition reactions. We are currently enlarging the number of molecules to 160 to assist convergence. Comparison is made with reactions in solid crystal TNT.

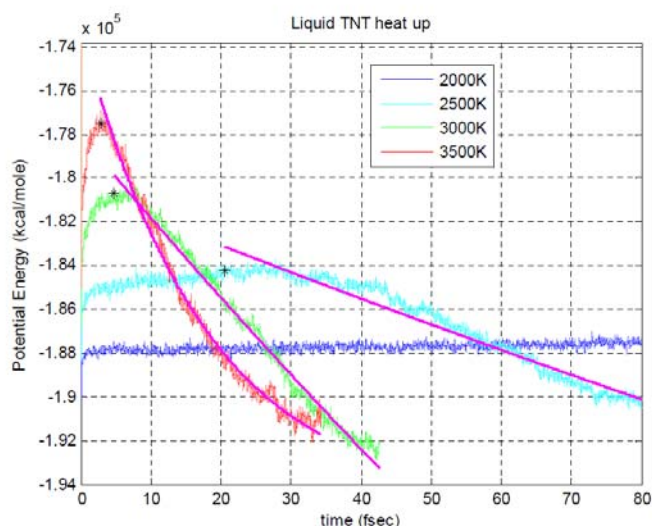


Figure 1: PE variation with time as a function of temperature.

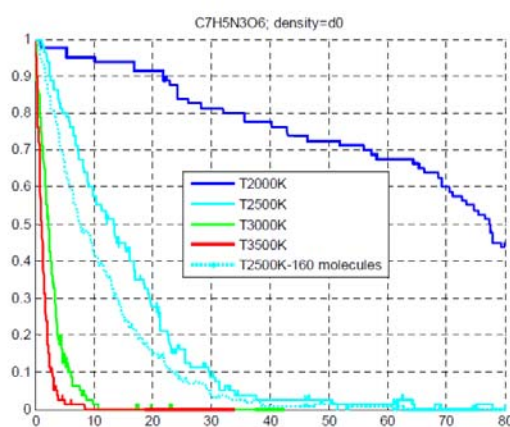


Fig2: Percentage of decomposition as a function of time for liquid TNT.

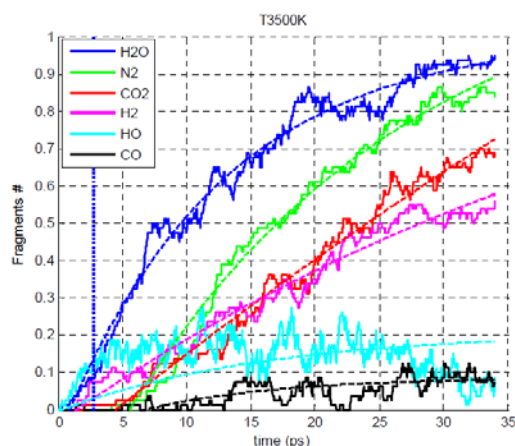


Fig 3: stable products of TNT decomposition

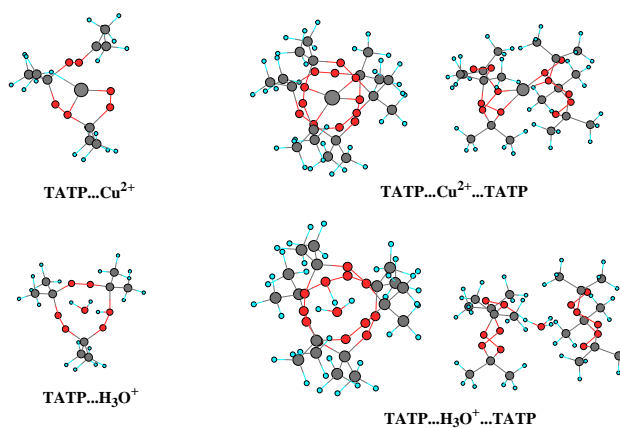
The role of metal Ions in the Destruction of TATP - theoretical considerations

Work of Dr. Faina Dobnikova in collaboration with Jimmie C. Oxley², James L. Smith

The safe decomposition of solid TATP (tri-acetone-tri-peroxide) explosive was examined theoretically. The route to destruction starts with formation of metal complexes between a metal ion and the TATP molecule. The second step is constituted of decomposition of the molecules into stable final products. We examined the structure and stability of both metal ion (including: Na^+ , Cu^+ , Cu^{2+} , Co^{2+} and Zn^{2+}) and Proton complexes with TATP using quantum chemical calculations at the DFT- PBE0 level. In addition, for each ion complex we determined the initial steps in the pathway to decomposition together with the associated transition states. We find that the products of decomposition, in particular acetone, are also stabilized by ion metal complexes. In agreement with experiment we find the best candidates for metal ion induced decomposition are Cu^{2+} and Zn^{2+} . For law enforcement agencies the problems are detection and destruction. The problem is made acute by their extreme sensitivity. Currently, the safest way to dispose illegal explosives is to detonate them on the spot. This procedure safeguards the law enforcement sappers from handling and transporting these highly sensitive materials. However, in some instances, relatively large quantities, one kilogram or more, of peroxide explosives are discovered, located in apartments and other high-population density areas. Blow-in-place protocols are impractical in such situations. Hence, there is an urgent need for suitable safe protocols that will safely destroy large quantities of peroxide-based explosives.

Early work on TATP destruction demonstrated the decomposition of small amounts of TATP using SnCl_2 solutions in water together with organic solvents in an acidic environment. These procedures allowed destruction of TATP in the range of few grams. In a recent study the destruction of both TATP and HMTD were examined utilized various metal ions in acidic water-organic solvent solutions as destroying agents. It has been shown that both Zn^{2+} and Cu^{2+} ions in Tetrahydrofuran (THF) in acidic conditions could lead to complete destruction of TATP and HMTD, but a large excess of ions was required for efficient destruction. Furthermore, destruction was violent if the reaction was attempted at the gram-scale or above.

To support the experimental effort to find a mode for gently destruction of peroxide explosives on the hundreds of gram scale, we initiated a theoretical analysis of the interaction of various metallic ions with TATP. First, we calculated and reported the binding of various metal ions to TATP. These quantum chemical calculations demonstrated that some metal ions bind to the TATP molecules to form complexes in which the TATP structure is not altered. However, a few ions bind to the TATP molecule and lead to destruction of the molecular ring. Other studies demonstrating the importance of the ion-TATP bond include those examining enhanced detection: the Na^+ -TATP interaction for electro spray ionization and the use of Zn^{2+} doped Titania nano-crystals.. The goal of the present work was to unravel the detailed chemical decomposition pathways of TATP induced by different ions. It is based on accurate quantum chemical calculations. The calculations incorporate, in an approximate manner, the effect of solvent as well as acid. We believe that this study will enable a rational design of more efficient and safe, destruction method of TATP. The figure shows sandwich type complexes of TATP.



IV. Students Supported

MoragAm Shalem:PhD. Subject: Molecular dynamics simulations of weak detonation waves.
 Ido Shefer: MsC. Subject: Molecular dynamics simulations of THz spectroscopy of TATP.

V. Conference & Journal Publications

- [1] Density-Dependent Liquid Nitromethane Decomposition: Molecular Dynamics Simulations Based on ReaxFF Naomi Rom, Sergey V. Zybin, Adri C. T. van Duin, William A. Goddard, Yehuda Zeiri, Gil Katz, and Ronnie Kosloff **J. Phys. Chem.** **115**, 10181 (2011).
- [2] **Role of Metal Ions in the Destruction of TATP: Theoretical Considerations**
 Faina Dubnikova, Ronnie Kosloff, Jimmie C. Oxley, James L. Smith, and Yehuda Zeiri,
J. Phys. Chem. **115**, xxx (2011).

Characterization of Non-Ideal Explosives

S. F. Son (PI), L. J. Groven, D. R. Guildenbecher, R. S. Janesheski
Mechanical Engineering, Purdue University

1. Objective

The goal of this experimental work is to characterize non-ideal explosives on a small-scale. The need of characterized non-ideal explosives has seen an increase due to the constituent materials used and relatively low costs that allow terrorist to obtain and use them. However, there is an insignificant amount of experimental data available due to the large-scale setup that is required for characterization. The main restraint is due to the large critical diameters needed to sustain a steady detonation in a non-ideal explosive. Previous work with neat ammonium nitrate (AN) showed a critical diameter of 41.2 mm [1]. We are performing small-scale experiments in tubes with small diameters relative to the expected critical diameter and anticipating unsteady detonations that are likely to fail in many cases. Using a microwave interferometer, a highly time resolved profile of the location of the detonation front is measured. The failure dynamics measured with the interferometer allows for the characterization of the non-ideal explosive over a wide parameter space (from overdriven to failure). A simulation of the experimental results is being pursued using CTH, a shock physics hydrocode, to calibrate a reaction model of the non-ideal explosive. The small-scale nature of the experiment allows for various parameters to be changed quickly that include chemical composition, non-ideal explosive density, and confiner thickness. The final goal of this work is to demonstrate that the calibrated model obtained from the small-scale experiment calibration is able to predict the results of large scale experiment.

2. Summary

A unique method for characterizing non-ideal explosives on a small-scale has been achieved. Successful experiments have been performed using the microwave interferometer to measure the detonation front's position profile of non-ideal explosives. Different compositions of AN with either diesel fuel, mineral oil, or sugar have been used as non-ideal explosives. The failure dynamics between the compositions were measurably different. The amount of fuel in the non-ideal explosive affected the distance the detonation was able to sustain itself as well as the rate at which it decreased in velocity and eventually reached complete failure.

Experiments also showed different failure dynamics among a single composition when the thickness of the confinement was changed. It was seen that lateral losses of energy occur in the thin-walled confiners and reduces the reaction zones ability to sustain the detonation. The thick-walled confiner sees minimal deformation, which allows for the much slower rate of deceleration of the detonation front as it is failing.

Future work is planned to measure the position profile of the non-ideal explosives using PMMA attenuators with different lengths. Detonation of the non-ideal explosive should occur as long as the shock transferring through the PMMA is relatively overdriven for the explosive. The goal is to see the initiation of the detonation within the non-ideal explosive from the overdriven shock and how the weakened shock through the attenuator affects the failure dynamics. Other potential tests also include changing the density of the non-ideal explosive and how it alters the failing detonation front. A very dense non-ideal explosive may limit the hot-spot formation that is required to sustain the reaction zone developed as the shock travels through the material. Material properties such as particle size are also of potential interest.

Modeling of the non-ideal explosives is underway using CTH. Working simulations have been developed and parameters are currently being tuned to fit the experimental data. Once the data has been fit, the calibrated model will then be compared to results reported from large scale experiments. If successful, this experimental technique will allow for a much cheaper and less time consuming method of calibrating currently needed models of non-ideal explosives.

3. Accomplishments

Highly time resolved measurements of the detonation front failing within non-ideal explosives have been successfully performed. Experiments have been completed that investigated the various factors such as composition and confiner thicknesses have on the failure dynamics of non-ideal explosives. Compositions of AN and diesel fuel were characterized with 2 wt.% and 10 wt.% diesel in thin-walled tubes. All tests utilized a steady detonation developed with Primasheet 1000 that would transition to the non-ideal explosives. Both compositions in the thin tubes showed the detonation completely fail before it reached the end of the confiner. However, the position trace between the two compositions showed that the detonation failed at different rates. AN/2 wt.% diesel fuel sustained the detonation for a longer period of time. The detonation velocity decreased at a slower rate compared to the AN/10 wt.% diesel. CHEETAH predictions showed higher C-J pressures for AN/2 wt.% diesel compared to AN/10 wt.% diesel. It is known that non-ideal explosives typically do not reach C-J conditions, however the trend in decreasing C-J pressure may correlate to the difference in failure dynamics between the two compositions.

Similar comparisons were evident with non-ideal explosives consisting of AN and sugar. Compositions of 15 wt.% and 50 wt.% sugar were investigated in thin-walled confiner. CHEETAH also predicted higher C-J pressure for 15 wt.% sugar which correlated to a slower deceleration of the measured detonation front. It is noted that differences between the positions profiles were also seen when the compositions had time to absorb water. The hygroscopic nature of sugar introduced water into composition that also increased the rate of failure for the detonation front.

The final tests that have been accomplished were of AN/2 wt.% mineral oil tested with two different confiner thicknesses. Thin-walled confiners showed a much faster deceleration of the detonation front compared to the thick-walled confiner. The detonation in the thick-walled confiner was seen to decrease in speed; however it never reached complete failure. Due to the deformation of the thin-walled confiner, much more energy is lost behind the detonation front. The non-ideal explosive already struggles to sustain itself due to having a smaller diameter than the critical diameter. The loss of energy further increases the rate of failure. This thick-walled confiner limits the lateral loss of energy behind the detonation front, allowing for the reaction zone to sustain the detonation for a longer period of time.

Velocity profiles of the experiments were also developed using a numerical differentiation technique using Fourier transforms [2]. The velocity profiles show a constant velocity through the ideal explosives, as expected. It can then be seen that the detonation is initially overdriven in the non-ideal explosive. Eventually the detonation front reaches a steady deceleration until complete failure occurs. The rate of deceleration is seen to change depending on the confinement thickness. The dynamics involved as the overdriven shock reaches the steady deceleration is seen to differ between different compositions tested.

All tests performed have showed the ability of the microwave interferometer technique to successfully measure different failure characteristics among different non-ideal explosive configurations. Simulating the experimental results using CTH has begun. It is our goal to use to tune the parameters of a suitable model to calibrate our experimental data.

4. Details

4.1 AN/Diesel Fuel in Thin Confiners

Figure 1 shows the position profile of the detonation front through the ideal and non-ideal explosives in a thin-walled confiner. To the right of the plot is a schematic of the confiner where the red portion represents the ideal explosive and the blue portion represents the non-ideal explosive. The red horizontal line also represents the location in the tube where the transition from ideal to non-ideal explosives occurs. The constant linear slope seen from below 3.8 cm represents the constant velocity of the detonation front through the ideal explosive. It is seen that the detonation front is overdriven for a few μ s before the slope decreases as the detonation speed is slowing down.

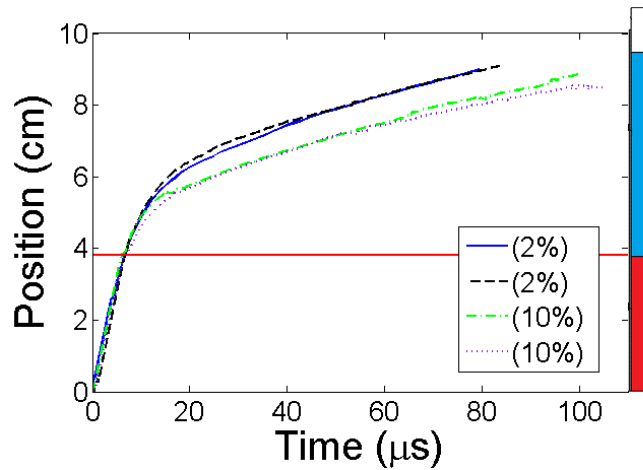


Figure 1. Position profile of the detonation front for AN/diesel at two different compositions.

It is seen in Fig. 1 that the AN/2 wt.% diesel sustained the detonation of the non-ideal explosive farther down the tube than the AN/10 wt.% diesel. This is also physically seen as more material was recovered after the test for the AN/10 wt.% diesel tests. The rate that the detonation slowed down from the overdriven state is also lower for the AN/2 wt.% diesel mixture. These results correspond with the higher C-J pressure predicted for the AN/2 wt.% diesel as well. It is hypothesized that the higher pressures that are possible for the AN/2 wt.% composition allow for the reaction zone to sustain the detonation front more efficiently.

4.2 AN/Mineral Oil in Thin/Thick Confiners

The difference between how the detonation front decelerates is much more pronounced due to the confinement of the non-ideal explosives. As seen in Fig. 2, the detonation front decreases in velocity very slightly in the thick-walled confiner compared to the thin-walled confiner. The horizontal lines represent the locations where the detonation front transitions to the non-ideal explosive where the red line represents the thin-walled confiner and the blue line represents the thick-walled confiner. The discrepancy is due to machining requirements of the thick-walled confiner. The non-ideal explosive also reaches the end of the thick-walled confiner and never completely fails where material was recovered in the thin-walled confiner. The thick-walled confiner limits the lateral losses behind the detonation allowing for the reaction zone to sustain the detonation much more effectively. Energy is lost behind the detonation front due to the deformation that occurs in the thin-walled confiner.

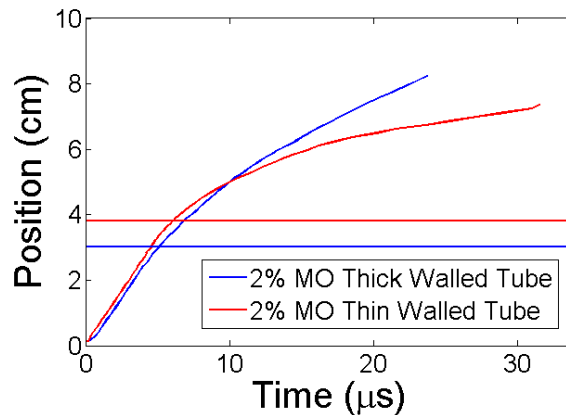


Figure 2. Position profile of the detonation front for AN/Mineral oil in thin and thick wall confiners

4.3 AN/Sugar

Experiments were performed with AN mixed with 15 wt.% and 50 wt.% sugar. Similar results were seen that were reported for the AN/diesel experiments. The higher wt.% of sugar did not sustain the detonation front as far as the lower wt.% through the non-ideal explosive and the detonation speed decreased much faster as seen in Fig. 3. It is noted that only the non-ideal segments are plotted. During testing, it was also seen that the sugar was absorbing water from the air during storage of the samples. Results show that after a few days, the AN/15 wt.% sugar composition failed to sustain the detonation as effectively as when the experiment was performed on the same day of preparing the non-ideal explosive. Urea was also considered as a fuel but it absorbed moisture at an even faster rate than sugar and consequently did not allow for reliable results.

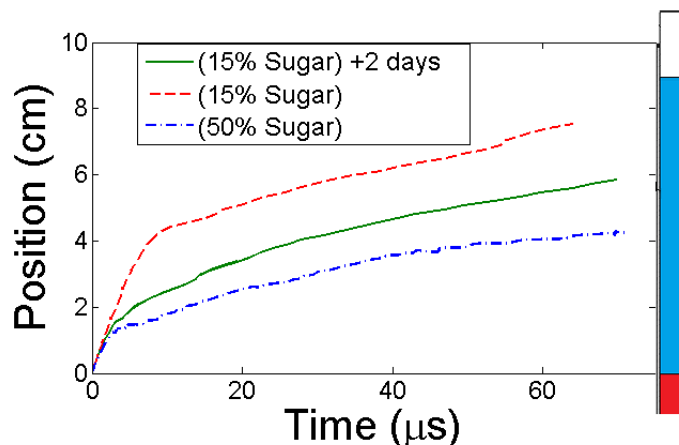


Figure 3. Position profile of the detonation front for AN/Sugar in thin confinements.

5. Students Supported

Robert Janesheski (Partially Supported)

6. Conference & Journal Publications

- R. S. Janesheski, L. J. Groven, S. F. Son, “Detonation Failure Characterization of Non-Ideal Explosives”, 17th Biennial International Conference of the APS Topical Group on Shock Compression of Condensed Matter, Chicago, Illinois on June 26-30, 2011. (Presentation)
- Journal article in progress

7. Works Cited

1. Miyake, A. “Non-Ideal detonation properties of ammonium nitrate and activated carbon mixtures.” International journal of modern physics b 22.9-11 (2008):1319-1324.
2. Levie, R.D., et al. “Numerical differentiation by Fourier transformation as applied to electrochemical interfacial-tension data.” Analytical chemistry 50.1 (1978):110-115.
3. Krall, A. D., B. C. Glancy and H. W. Sandusky. “Microwave interferometry of shock waves .1. Unreacting porous-media.” Journal of applied physics 74.10 (1993):6322-6327.
4. Burnside, Nathan. "Deflagration to detonation transition in granular HMX" MS thesis Brigham Young University, 1999. Print.

***Development of Simulants of Hydrogen Peroxide Based Explosives for use by
Canine and IMS Detectors***

José Almirall,
Chemistry Dept, Florida International University

Objectives

The objective of this effort is to develop an improved field instrument system for the detection of explosive odors based on ion mobility spectrometry (IMS). The PI and co-workers have previously described the composition of the volatile and semi-volatile chemical compounds that are characteristic of several drugs of abuse and chemical explosives in order to assist the design and application of canine detection training aids. The PI has also developed ***pre-concentration*** and ***sampling*** devices based on Solid Phase Microextraction (SPME) for the capture of extremely small quantities of the volatile compounds (on the order of ng) for subsequent detection using IMS using an in-house developed interface (patent pending). The current effort investigates home-made explosives (HME) detection, particularly explosives based on hydrogen peroxide (HP). This proposal aims to characterize the odor signatures of a set of samples from HP-based explosives, some of which will be provided by the University of Rhode Island Center of Excellence, in order to improve the detection of this threat using IMS instruments. The existing large installed base of > 12,000 IMS instruments make this technology viable as a crime scene detection tool and the already proven use of detection canine teams also makes this approach a viable alternative to instrumental detectors. The project team will continue to characterize the odor signature compounds of HP-based explosives and provide the chemical data to the URI center collaborators. The results will also be used to target compounds that can be used for 1) IMS detection and 2) canine detection. The identification of these compounds will assist future researchers interested in detection of HP-based explosives. Additionally, the effort will continue to develop a planar-SPME device specifically designed and optimized to extract the volatile odor signature compounds associated with HP-based explosives. Finally, the existing IMS operating parameters will be investigated to work towards an unambiguous identification of the target compounds of the HP-based explosives by coupling an IMS instrument with a mass spectrometer of high sensitivity to better investigate the composition of the ion swarms in the IMS experiment. An already existing ESI-IMS-MS instrument in our laboratory will be used in this research along with the more traditional techniques of SPME-GC-MS and SPME-IMS already developed in our lab.

Accomplishments

TATP is highly volatile explosive readily from easily available reactants making it accessible for illicit uses. In this study, fast detection of TATP is achieved using a novel planar solid phase microextraction (PSPME) as a preconcentration and sampling device for headspace analysis, offering improved sensitivity and reduced sampling time over the conventional fiber-based solid phase microextraction (SPME) when followed by IMS detection. Quantitation and comparison of the retention capabilities of PSPME as opposed to the commercially available SPME were determined using TATP standards and analyzed using gas chromatography-mass spectrometry (GC-MS) for SPME analysis and a commercial IMS with no instrumental modification for PSPME. Static and dynamic headspace extractions were used and compared for PSPME extractions, in which low mg quantities of TATP

were detected within 30 seconds of static mode and less than 5 seconds in the dynamic mode for PSPME.

Details

Triacetone triperoxide (TATP) was first discovered and prepared in 1895 by . Its extreme sensitivity to friction, shock and impact makes it ¹Wolffenstein ; however, the ease of synthesis ¹unfavorable for many commercial or military use from readily available chemicals, the simple requirements of preparation and the . Thus, ²⁻³detonation effect attract much interest in criminal and terrorist activities development of fast, on-site, contact-free and reliable method for detection of TATP ⁴⁻⁵has received increasing attention within the last decade .

Since TATP lacks in nitro group and aromatic functionalities, well-established detection methods for the nitro-containing explosives such as 2,4,6-trinitrotolulene (TNT), nitroglycerin (NG) and 1,3,4-trinitro-1,3,5-triazacyclohexane (RDX) are not suitable for this peroxide-based compound⁶⁻⁷. Various analytical methods have been developed for the separation and detection of TATP for different purposes. Liquid chromatography (LC)⁸ and gas chromatography (GC)⁹ are used for separation of TATP and Infrared⁶ and Raman spectroscopy^{6, 10} techniques have been used to detect TATP in the laboratory. In addition, TATP can also be detected by either mass spectrometry which includes desorption electrospray ionization (DESI)¹¹ and selected ion flow tube (SIFT)¹² or other sensor based techniques such as luminescence¹³⁻¹⁴, electrochemical¹⁵⁻¹⁷, and biological¹⁸ sensors; however, none of these techniques can fully accomplish both purposes, time-efficient on-site analysis with unambiguous identification and low limit of detection from post-explosion debris with high selectivity. Ion mobility spectrometer (IMS) is another robust tool for the detection of TATP^{6, 19-22}. Ion mobility spectrometry has been used by the law enforcements in airports, government buildings, and at border crossings to detect explosives for several decades in which fast detection, high sensitivity, ease of use and on-site analysis makes this instrument superior to the other techniques²³; however, IMS has not been widely exploited in detection of TATP and limited research has been published due to the lack of efficient sampling method coupled to this instrument.

In 2010, a novel preconcentrator and sampling technique, planar solid phase microextraction (PSPME)²⁴, for rapid field air sampling developed by Guerra-Diaz et al. helps overcome the conundrum of sampling TATP encountered by IMS. The PSPME devices can be easily made in the laboratory which has similar chemistry characteristics as solid phase microextraction (SPME) fiber²⁴. The increased surface area of PSPME significantly shortens the extraction time and increases the extraction efficiency. Analytes extracted on the PSPME device can be directly thermally desorbed into a commercial IMS instrument. PSPME extractions can be accomplished in two different methods: static sampling and dynamic sampling. Static sampling is similar to the SPME extraction in which sampling is performed in a steadily constructed headspace. Dynamic sampling, assisted with a continuous pumped flow of air through the PSPME device, has been shown to be beneficial at shortening the sampling time. Unlike SPME which suffers from fragility and limited adsorption/absorption capacity²⁵⁻²⁶, the use of a commercial pump with PSPME allows reduced sampling time for large volumes²⁴.

In this study, we describe a fast method of sampling of TATP from headspace followed by detection of IMS within time scale of seconds. In addition, a comparative study between SPME and PSPME was performed to demonstrate the increased retention capability and faster sampling time as a result of increased surface

area and phase volume. This sample collection and detection method reduces the sampling time which allows the police to unambiguously identify explosives in time in the concern of public safety. At the same time, this portable PSPME device and IMS instrument allows on-site analysis with high sensitivity and selectivity. Furthermore, this is a contact free air sampling method which benefits both operators for safety concern and protecting the sample from contamination.

Instrumentation. Headspace sampling of TATP in the form of a solid carried in the University of Rhode Island (URI) were performed using a GE Ion Track (Wilmington, MA) ITEMIZER 2. GE N-mode (positive mode) calibration traps containing cocaine were used to calibrate the instrument in the N-mode. Further TATP detection experiments were performed in our laboratory in Florida International University (FIU) using the Smiths Detection IONSCAN®-LS (Smiths Detection, Warren, NJ) Ion Mobility Spectrometer. For this instrument, two different dopants were used, nicotinamide (original dopant in the positive mode this instrument) and isobutylramide purchased from Smiths Detection²⁷. The IMS operating conditions for these instruments are shown in Table 1. Activated charcoal strips (ACS) were analyzed using a Varian (Palo Alto, CA) CP 3800 gas chromatograph coupled to a Saturn 2000 ion trap mass spectrometer and equipped with an 8200 auto sampler (Varian Inc., Walnut Creek, CA). The GC-MS conditions are listed in Table 2. The MS was operated in electron ionization mode (-70 eV) with a scan range of 40-450 m/z and a delay of 3.5 minutes.

Smiths Detection IONSCAN®-LS	GE Ion Track ITEMIZER	IMS operating conditions
Positive (+)	Positive (+)	Polarity
250	175	Desorber temperature (°C)
235	195	Drift tube temperature (°C)
200	500	Sample flow (mL min ⁻¹)
351	350	Drift flow (mL min ⁻¹)
Nicotinamide/ isobutyramide	Ammonium carbonate	Reagent gas

Table 1: Conditions for the IMS instruments used in this experiment.

Restek 30 m x 0.25 mm ID x 0.25 um Rxi-5Sil fused silica	Column type
Helium at a flow rate of 1.0 mL min ⁻¹	Carrier gas
5:1	Split ratio
110 °C	Injector Temperature
40 °C, hold for 1 min. 100 °C at 5 °C min ⁻¹ , hold for 6 mins. 250 °C at 10 °C min ⁻¹ , hold for 5 mins.	Column oven parameters
280 °C	MS Transfer Line temperature
180 °C	MS Ion Trap Temperature

Table 2: GC-MS conditions

Chemicals and methods. TATP explosives were synthesized and prepared in the laboratory of URI²⁸. Cocaine standards were purchased from Cerilliant (Round Rock, TX) for the positive mode IMS calibration.

PSPME sampling devices were prepared by spin-coating a sol-gel PDMS solution on an activated glass fiber filter as stated previously²⁴ [ENREF 24](#) and used for both static and dynamic extractions. Approximately 10 mg of solid TATP explosive were placed in a half gallon glass jar and was allowed to equilibrate for 30 minutes. For static extractions, the PSPME devices were suspended over the sample at the opening of the jar. Various sampling times and temperatures (25 °C and 40 °C) were tested in triplicates to determine the minimum amount of time required for the detection of TATP using PSPME devices. For dynamic extractions, the PSPME device was inserted into a handheld vacuum sampler (Barringer) in order to allow flowing sample air through the PSPME device at a rate of 0.17 L s⁻¹. All dynamic extractions were equilibrated at the desired temperature; however, dynamic sampling was performed at room temperature due to the inability to fit the handheld vacuum sampler in the temperature-controlled oven.

Further headspace extraction was achieved by using activated charcoal strips (ACS)²⁹. A full activated charcoal strip was suspended in the headspace of 10 mg or 100 mg TATP explosives in the half gallon glass jars for overnight (16 hours) extractions at constant temperatures (25 °C and 40 °C). Half of the activated charcoal strip was then eluted with 100 µL of carbon disulfide (Spectrophotometric grade 99.9%, Acros Organics, New Jersey, USA) and analyzed with the GC-MS.

Static extractions and TATP calibrations completed in our laboratory were performed using certified TATP standards of 0.1 mg mL⁻¹ (AccuStandard, New Haven, CT) in acetonitrile (ACN) due to the inaccessibility of solid TATP. The TATP stock solution was diluted to concentrations 5, 10, 15, 20, 25 and 30 ng µL⁻¹ using methanol or ACN of optima grade (Fisher Scientific, Fair Lawn, NJ) for absolute mass quantitation in the GC-MS and PSPME devices.

Equilibrium time was obtained by performing static extractions at different extraction times. This was performed in triplicates with fresh spikes in new quart can for each replicate. Once the optimized equilibrium time was achieved, 5 µL of standard solutions of known concentration ranging from 5 to 30 ng µL⁻¹ were spiked into a quart-sized can containing a suspended PSPME filter and sealed immediately for 5 min static extractions. The signals were recorded and plotted to give a quantitative mass calibration of TATP in the PSPME devices.

Evaluation of the extraction efficiency of SPME and PSPME was achieved by spiking the desired amount of TATP on a quart can and extracting immediately without headspace equilibrium development. Detection of TATP extracted by SPME was performed using the Varian GC-MS, using the same method applied for ACS extraction analysis. Detection of TATP extracted by PSPME was analyzed with Smiths Detection IONSCAN®-LS without further modifications.

Detection of TATP in University of Rhode Island. Various static extraction times were performed at room temperature to determine the shortest extraction time for the detection of TATP. This experiment was also conducted at an elevated temperature (40 °C). Detection of TATP can be achieved within 1 minute extraction of the headspace of a half-gallon glass container at room temperature (Figure 1). By one minute of static extraction, the pool of protonated clusters associated as reactant ion

peak (RIP) in IMS was depleted by TATP on a PSPME device, giving two strong signals at 4.3 ms and 4.7 ms separately. TATP was identified in the GE Ion Track by using a 100 ppm TATP/hexane standard (peak at approximately 4.3 ms) as previously reported¹⁹. Similar results were obtained at elevated temperatures with faster extraction time and higher signal. Detection for TATP was achieved within 10 seconds of static extractions at 40 °C.

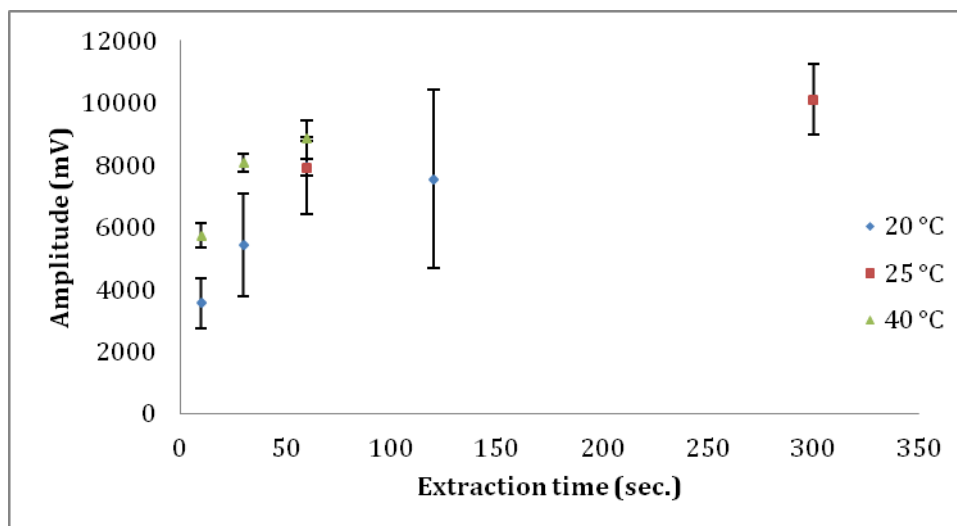


Figure 1: Signal observed at 4.3 ms at different static extraction times of TATP at different temperature profiles.

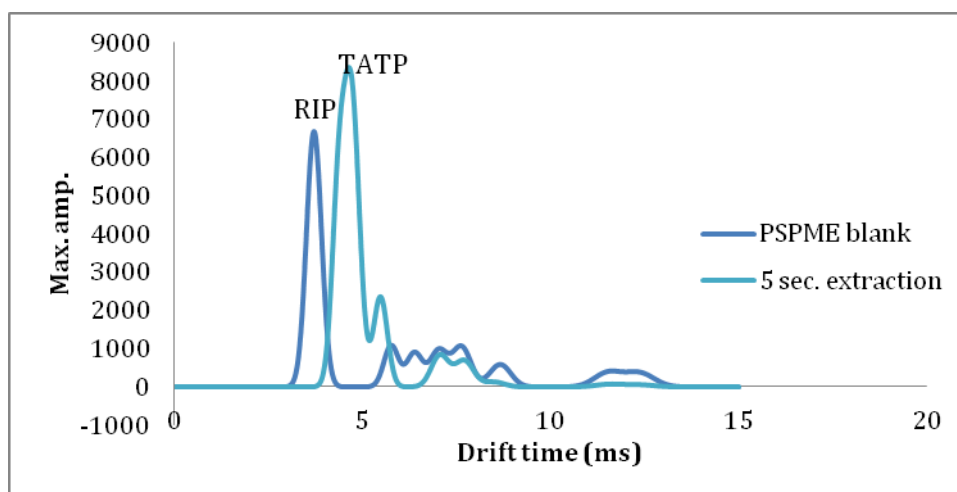


Figure 2: Dynamic PSPME extraction of 10 mg TATP for 5 seconds (0.85 L). TATP detection at 4.3 ms, depleting the reactant ion peak (RIP).

Dynamic extractions further confirmed the retention capabilities of the PSPME devices. Minimum of 5 second extraction produced high intensity signal of TATP (Figure 2) after sampling a total volume of 0.85 L. Similar to static PSPME sampling, TATP peak was evident at approximately 4.3 ms. Further sampling at elevated temperatures was unnecessary since fast detection of TATP was achieved.

Activated charcoal strip extraction analysis. Activated charcoal strips extractions were studied to adsorb and analyze all the volatile chemical compounds found in the headspace of TATP. The majority of the headspace was observed to be TATP (having a retention time of 11.2 minutes and a mass spectra in close agreement with

other reported value³⁰⁻³¹) [ENREF 10](#), resulting in a prominent signal in the GC-MS analysis. Other impurities observed in the headspace include straight-chain alkanes could come from the glass jar or from the precursor chemicals used in synthesis of TATP in laboratories³² [ENREF 12](#) [ENREF 12](#). Some peaks from TATP impurities were not observed in the ACS analysis of 10 mg TATP; however, these peaks were evident when sampling 100 mg of TATP (Figure 3 (b)).

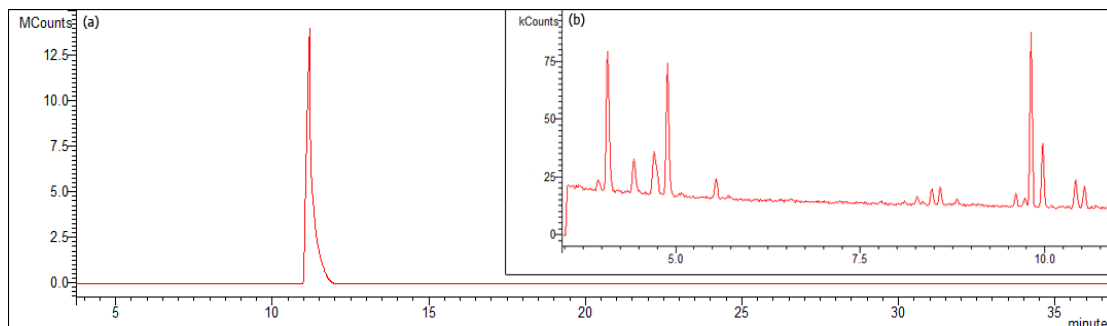


Figure 3: (a) Full chromatogram of ACS extraction of 10 mg TATP; TATP is the most significant peak having a retention time of 11.2 minutes. (b) Zoomed chromatograph to display other impurities seen from ACS extractions from 100 mg of TATP.

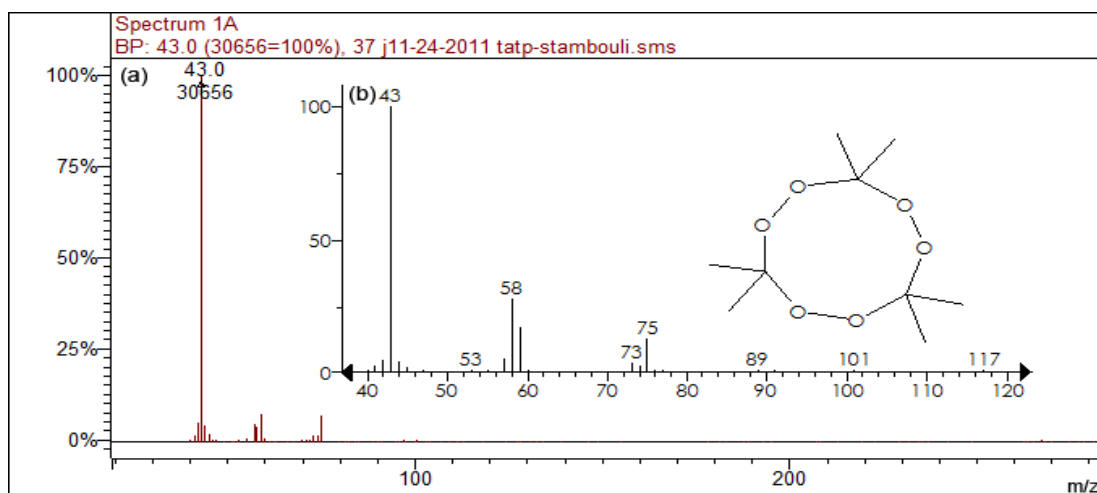


Figure 4: Observed spectrum (a) at retention time 11.2 ms and reference spectrum (b) of TATP³⁸.

Detection of TATP in FIU Laboratory. Alarm for TATP was observed within 1 minute of static extraction with 0.5 μ g spike of a TATP standard in the quart container, generating a peak with drift time of 6.7 ms and a reduced mobility (K_0) of 2.57 in close agreement with previously stated reduced mobility of TATP⁶. This reduced mobility is different from other reported values³³⁻³⁴ which could be due to the shift in equilibrium in the IMS drift tube from the increase in temperature. Increased temperatures result in formation of less hydrated proton clusters thus resulting with a smaller collisional cross-section and increase in reduced mobility^{23, 35}. Also, the use of nicotinamide dopant has shown to reduce the amount of peaks associated with the analyte ions most commonly used in narcotics and illicit drug detection³⁶, further reducing the reduced mobility observed.

Absolute mass calibration of TATP in PSPME filters. A response curve was generated (Figure 5) using the observed maximum amplitude (d.u.) from Smiths IONSCAN resulting in the following linear regression line:

$$(y) = 190.05 (x) - 229.72, r^2 = 0.984 \quad (1)$$

From this method, the minimum detectable amount of TATP was determined to be 1.4 ng.

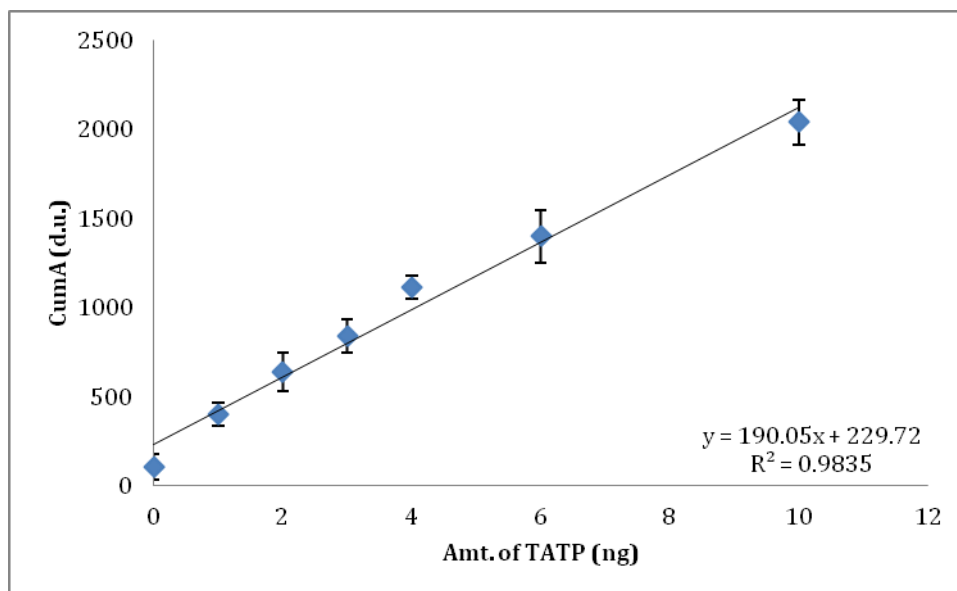


Figure 5: TATP mass calibration obtained by spiking 2 μL TATP of the following concentrations: 0.5, 1.0, 1.5, 2.0, 2.5, 3.0, 5.0 $\text{ng } \mu\text{L}^{-1}$.

Since PSPME extraction is an equilibrium technique similar as SPME, this technique can be used for quantitation analysis. Headspace calibration was achieved by spiking a known amount of TATP into a closed system and headspace sampling using PSPME at the equilibrium time of 5 minutes (Figure 7). Calibration of TATP was performed using two dopants to evaluate the performance of isobutyramide for peroxide-based explosive detection²⁷. Dopant selection is essential for optimal instrument performance in order to form stable and identifiable analyte ions and suppressing ionization of unwanted analytes. Response curves from the Smiths IONSCAN using the nicotinamide and isobutyramide are given in equations (2) and (3) respectively:

$$(y) = 20.04 (x) - 272.3, r^2 = 0.986 \quad (2)$$

$$(y) = 22.58 (x) - 384.5, r^2 = 0.986 \quad (3)$$

The response signals observed in the IMS were similar using either the nicotinamide or the isobutyramide dopant, thus majority of the experiments were performed using the initially installed nicotinamide dopant. After 5 minutes of static PSPME extractions, the minimum amount of spiked TATP in the can using both dopants was determined to be approximately 19 ng, as shown in Figure 6. When evaluating the extraction efficiency of the PSPME devices (percentage between the mass detected and the amount available), the dynamic PSPME devices showed an extraction efficiency of 14%. This significant extraction efficiency shows the preconcentration power of the PSPME devices within minutes of static extraction.

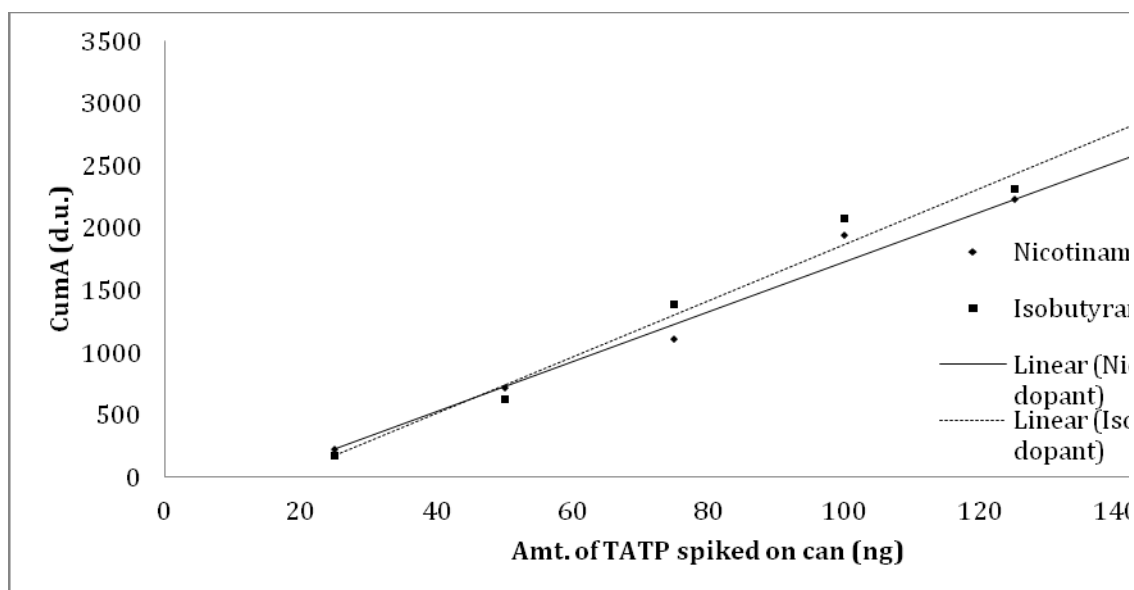


Figure 6: TATP headspace calibration obtained from 5 minute static PSPME headspace extraction of TATP (spiking 5 μL of solutions of the following concentrations: 5, 10, 15, 20, 25, 30 $\text{ng } \mu\text{L}^{-1}$)

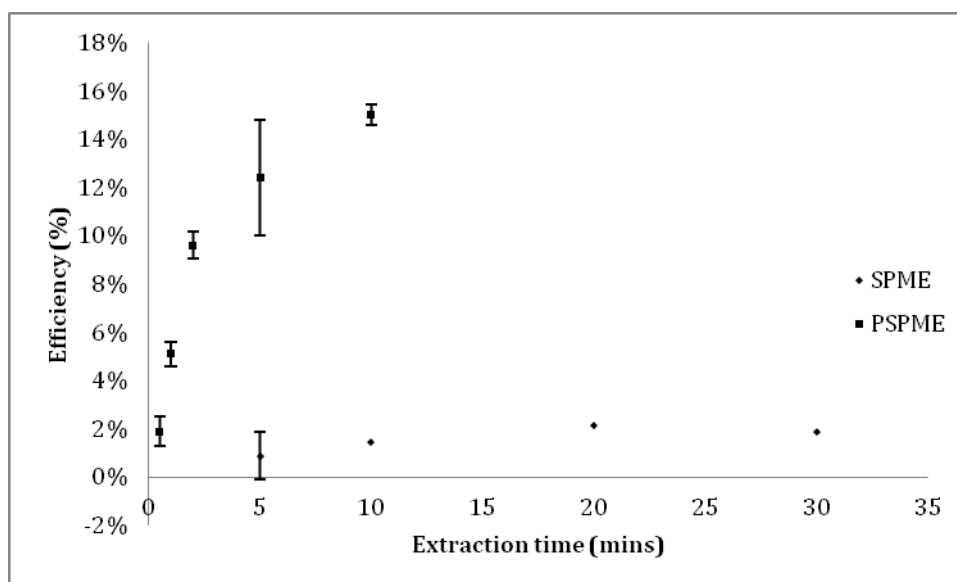


Figure 7: Percent recovery comparison of PSPME and SPME by different static extraction time (0.5 – 30 minutes) of 100 ng TATP.

Headspace extraction efficiency comparison of PSPME and SPME. The extraction phase volume of a planar SPME disk is calculated to be approximately 35 mm^3 , compared to the commercial fiber SPME with a maximum phase volume of 0.6 mm^3 ³⁷, offering greater than 50 times more volume capacity and a surface area of ~ 1000 greater than that of fiber SPME. Minimum amount of extraction time for detection of 100 ng of TATP for PSPME was observed to be 0.5 minutes compared to 5 minutes using SPME (Figure 7). Comparison of the extraction efficiency by varying concentration of TATP was performed by spiking different nanogram-level of TATP standard and extracting for five minutes. The amount of TATP recovered using PSPME was calculated by using an external calibration curve with the

regression line in Equation (1). For SPME analysis on the GC-MS, the following linear regression curve was used:

$$(y) = 2302 (x) - 1661, r^2 = 0.964 \quad (4)$$

Extraction efficiency of TATP on PSPME and SPME was determined to be approximately 15% and 1% respectively as shown in Table 3. Thus, the increased surface area and phase volume of PSPME offers much greater extraction efficiency and faster detection in comparison to the commercially available fiber-based SPME.

SPME		PSPME		Amt. spiked in can (ng)
Recovery %	Amt. of TATP recovered (ng)	Recovery %	Amt. of TATP recovered (ng)	
		5.16%	2.58	50
		6.17%	4.63	75
1.22%	1.22	9.00%	9.00	100
0.85%	1.27	14.0%	21.0	150
0.75%	1.50	17.5%	35.1	200
0.79%	2.36	20.6%	61.8	300
0.85%	3.39	19.8%	79.2	400

Table 3: Percent recovery comparison of PSPME and SPME by 5 minutes static extraction of different amount of TATP.

In conclusion, due to the increased surface area and phase volume in PSPME, TATP was sampled and preconcentrated on a PSPME device in less than 30 seconds by both static and dynamic extractions followed by detection using a COTS IMS which does not require any modification to the instrument. When using IMS as the detection method, the sampling and detection time of TATP was significantly shortened; thus indicates the potential use of this method in field analysis for both time efficient and high selectivity detection. The total sampling and detection time of TATP was significantly simplified and shortened (~ 35 sec.), in comparison with fiber-based SPME sampling and analysis in GC-MS (~ 22 min). Compared with fiber-based SPME, the extraction efficiency is increased from approximately 1% to approximately 15% when using PSPME. The extraction efficiency for SPME reached a maximum of 2% at 20 min, while PSPME can easily obtain 1.9% with only 30 sec. extraction. These results suggest that PSPME devices can be coupled with various commercial IMS systems to provide high through-put, sensitive detection of different explosives in the field. Future work will develop receiver operator characteristic (ROC) curves to evaluate the utility of PSPME-IMS in real-world environments.

IV. Students Supported

Mimy Young: PhD in Chemistry

Wen Fan: PhD in Chemistry

V. Conference Presentations & Journal Publications

Presentations:

1. June 2011. Performance Evaluation and Calibration of Planar Solid Phase Microextraction (PSPME) Using Vapors of Standards Followed by Ion Mobility Spectrometry (IMS) Detection, Gordon Research Conference, Lucca, Italy (Poster)

2. June 2011. Headspace Profiling of Volatile Compounds from Explosives Using Planar Solid Phase Microextraction (PSPME) Followed by Ion Mobility Spectrometer (IMS) Detection Gordon Research Conference, Lucca, Italy (Student Poster)
3. June 2011. Improved Sampling and Preconcentration of Volatiles from Explosives using Planar Solid Phase Microextraction (PSPME) in Comparison to Fiber SPME, Gordon Research Conference, Lucca, Italy (Student Poster)
4. April 2011. Sampling and Detection of Volatile Chemical Signatures from Explosives, Trace Explosives Detection Conference, Portland, OR (**Invited Tutorial, PA**)
5. April 2011. Fast Detection of Triacetone Triperoxide (TATP) from Headspace using Planar Solid Phase Microextraction (PSPME) Coupled to an Ion Mobility Spectrometer Detector, Trace Explosives Detection Conference, Portland, OR (Poster, PA)
6. April 2011. Planar Solid Phase Microextraction- Ion Mobility Spectrometry for Rapid Field Air Sampling and Analysis of Explosives and their Associated Volatile Chemical Signatures, Trace Explosives Detection Conference, Portland, OR (Poster, P. Diaz-Guerra)
7. March 2011. Development of Simulants of Hydrogen Peroxide Based Explosives for use by Canine and IMS Detectors, ALERT Conference, Rhode Island Department of Homeland Security Center of Excellence, Boston, MA (Invited Poster, SP)

Publications:

1. Fast Detection of Triacetone Triperoxide (TATP) from Headspace using Planar Solid Phase Microextraction (PSPME) Coupled to an Ion Mobility Spectrometer Detector. In preparation.

Explosive Particles Sampling & Detection

Ben Gurion University

Yevgeny Zakon, Arcady P. Gershanik and Yehuda Zeiri

Objective

During the passing year the research at BGU was pursued in mainly two directions. The main objectives in the research were measurement and analysis of adhesion forces between explosive particles and various substrates using the method based on AFM force measurements. The main goal in these measurements was to gain understanding the importance of chemical interactions in the particle-substrate adhesion process.

Another direction we pursued this year included the study of the sublimation of PETN and RDX micro-particles. These experiments were carried out using a Quartz Crystal Microbalance (QCM) apparatus to follow the sublimation process. This was a continuation of the study reported last year related to TNT sublimation.

Accomplishments

AFM measurements: A very large number of measurements were carried out. These examined the adhesion of: TNT, PETN, RDX and HMX particles onto self assembled monolayer (SAM) positioned on a gold thin film. In addition, we carried out experiments where the SAM was positioned on the AFM tip and the interaction force between the tip and explosive particle was measured. All of the measurements were carried out at both ambient room conditions and under water. In addition to the evaluation of the adhesion forces we also calculated the Hamaker constants for these systems.


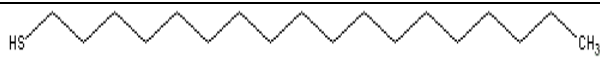
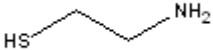
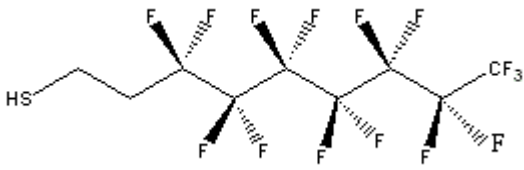


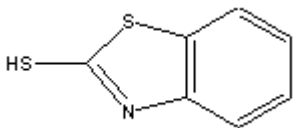
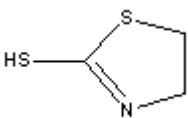
QCM measurements: Reliable measurements of non-uniform PETN and RDX micro-crystals layer sublimation rate was carried out using quartz crystal microbalance (QCM). The micro-crystal layer was precipitated from solution of PETN or RDX on the QCM electrode. It was shown that for these explosives too the kinetics of sublimation is controlled by the molecular diffusion in air. The simple model that was developed last year for TNT to describe the sublimation process was shown to well describe the sublimation of PETN and RDX. Based on the diffusion controlled model, expressions to describe the particle size evolution in time were derived including particles with size comparable to the mean free path in the gas phase.

Details

AFM measurements:

The contribution of chemical interaction to the adhesion force of different explosive particles was studied by force measurements of explosive particle with SAMs. Two types of experiments were performed, in the first The adhesion force between an explosive particle and a SAM covered thin gold films on glass was measured. In the second type of experiments the SAM was deposited on the AFM tip and the cantilever was used to measure the adhesion between the tip and explosive particle surface. To construct the SAM we used different molecule that had on one side -SH group and various functional groups on their other end. The Thiol group binds spontaneously to gold substrates, hence, the SAM is formed. We did not examine the structure of the SAM but used preparation methods described in the literature to form the SAM. The contact angle of water with the SAM was measure and compared to the literature. The molecules used to generate the various SAMs are presented in Table 1.

Table 1: List of molecules used to construct the different SAMs investigated in this study.

Published contact angle [°] and reference	Measured contact angle [°]	Molecular structure	Molecule used (symbol in figures)	End Group
75.9 [16]	75		Au layer (Au)	none
26.1 [16]	27		11-mercapto-1-undecanol (OH)	hydroxide
108.9 [16]	102		Octadecane thiol (CH3)	methyl
34 [17]	38		Cysteamine (NH2)	amine
150 [18]	150		Perfluorodecanethiol (CF3)	Fluoride
40-50 [19]	45		3-mercaptopropionic acid (C3COOH)	Carboxyl
40-50 [19]	52		8-mercaptooctanoic acid (C8COOH)	Carboxyl
65 [20]	65		4-Phenylthiazole-2-thiol (Phenyl)	Phenyl
	85		2-mercapto-2-thiazolin (SN)	C ₃ H ₄ SN

The adhesion forces between SAM covered tips and the four explosives as measured in ambient air and under water are shown in Figs. 1 and 2 respectively. The adhesion force measurements in the two media yield similar values. In the air measurements the strongest adhesion of the tip is obtained for SAMs with OH and Phenyl end groups. Under water the SAM with Phenyl end group is still the largest but the results for OH are comparable to those of other end groups. The

measurements in water eliminate contributions of capillary forces. As the data presented in Figs. 1 and 2 suggest, the contribution of capillary forces to the tip adhesion is rather small. The results clearly indicate that there is a contribution due to chemical interactions to the adhesion forces measured. It should be noted that in this case the contact area between the tip and the substrate is rather small, it depends on the tip curvature. For all end groups the HMX seem to have the strongest adhesion in air while the weakest adhesion is in most cases for TNT. This behavior is less pronounced in the measurements performed in water.

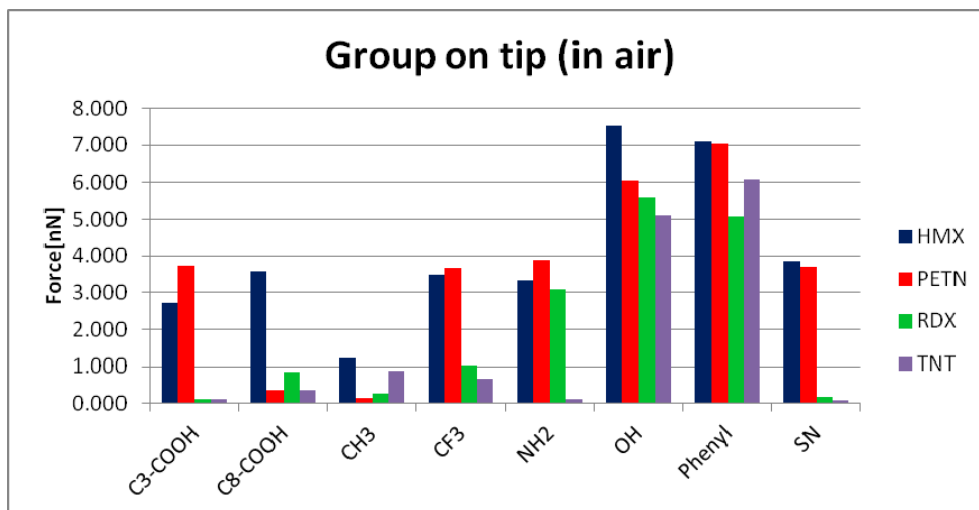


Fig. 1: Adhesion force between different explosive and end groups of the SAM deposited on the tip measured in ambient air.

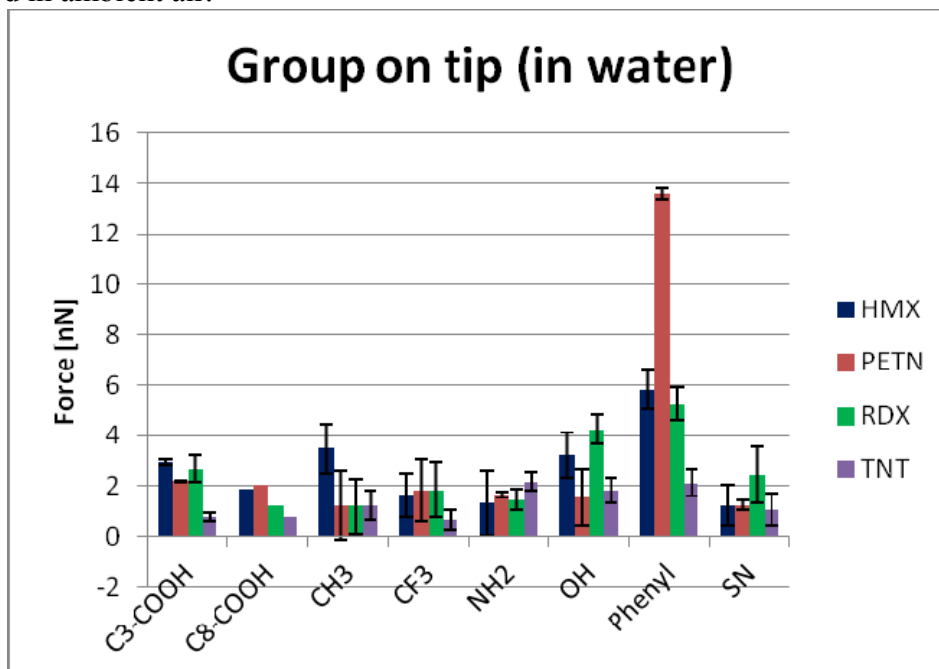


Fig. 2: Adhesion force between different explosive and end groups of the SAM deposited the tip, measured under water.

The adhesion forces obtained in the second set of experiments, adhesion of explosive particle to a SAM on a thin gold film, are shown for air and water media in Figs. 3 and 4 respectively. Inspection of these results shows that for air measurements again the adhesion to SAM with OH or Phenyl end groups is the strongest. Similar to the data in Fig. 1, HMX seems to yield the largest adhesion for all end groups. This behavior changes markedly for measurements in water, here, the CH₃ end group seems to exhibit the largest adhesion forces while those for OH and Phenyl are less pronounced. Comparison of the adhesion forces in air and under water shows that the latter are two orders of magnitude smaller. This very large difference is attributed to the large contribution of capillary forces. The explosive particles used had irregular shapes and their size was about 20 μm . Thus, the contact area between the particle and the SAM surface can vary dramatically from one particle to the other. Each particle may have multiple contact points with the substrate, each one contributing capillary forces provided there is enough humidity in the air (measurements were performed at approximately 60% relative humidity).

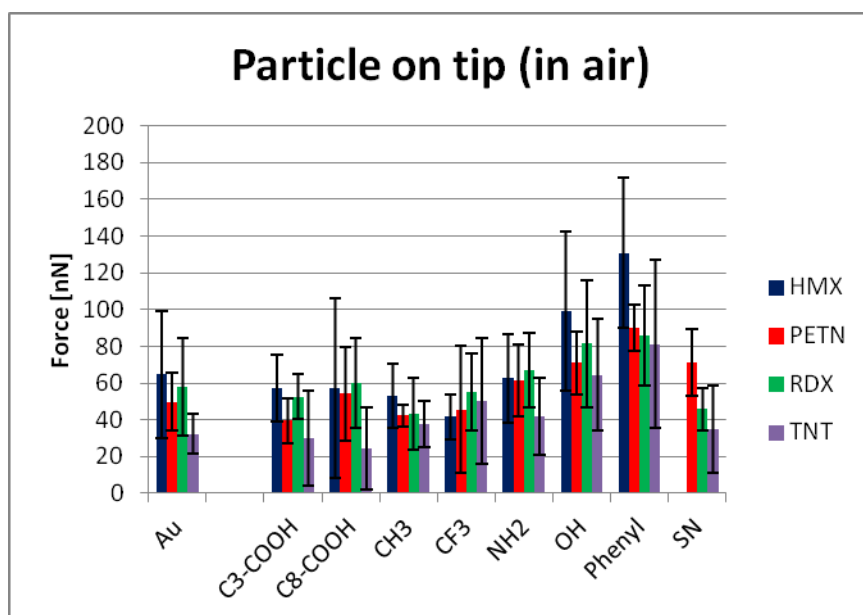


Fig. 3: Adhesion force between different explosive particles and end groups of the SAM deposited on a glass substrate measured in ambient air.

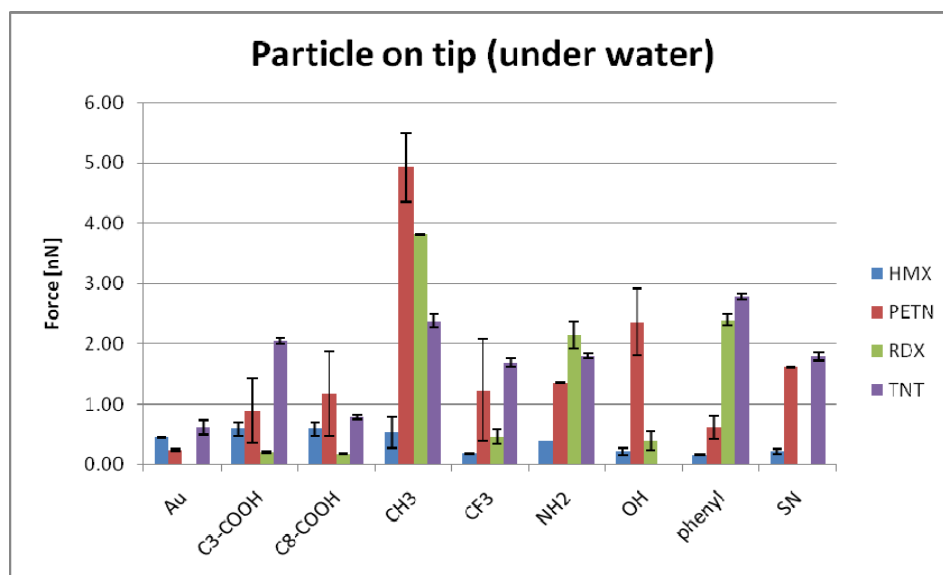


Fig. 4: Adhesion force between different explosive particles and end groups of the SAM deposited on a glass substrate measured under water.

The force measurements for all systems were also analyzed to obtain the Hamaker constants. The results described above together with the Hamaker constant values are being summarized at present in a paper to be published. The data reported last year, together with additional measurements to allow detailed comparison between different systems is being summarized in another paper at present.

QCM measurements:

To be able to estimate the life time of explosive particles in ambient conditions we carried out sublimation experiments of explosive particles by following the variation in their weight using a QCM. The first explosive studied was TNT, reported last year. This year we carried out similar experiments for PETN and RDX. The samples were prepared by the deposition of a well defined volume of PETN or RDX solutions in acetonitrile (2 mg/ml) onto the QCM sensor surface and evaporation of the solvent. The sample obtained constituted of well separated micro-crystals of PETN or RDX. In the case of PETN we obtained well separated micro-crystals with hemi-spherical shape and average diameter of 35 μ m, see optical microscope picture in Fig. 5. In the case of RDX, a nearly uniform layer of small micro-crystals was formed, see Fig. 6.

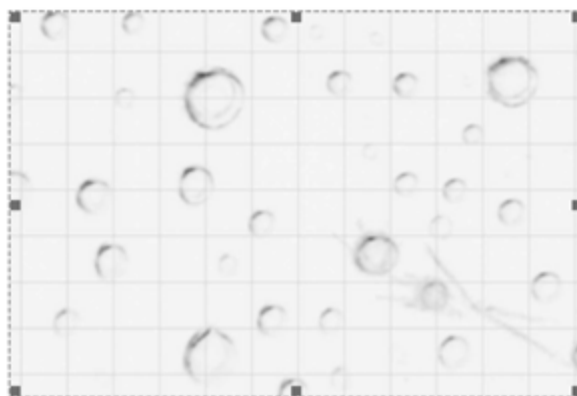


Figure 5. Typical optical microscope image of the PETN sample. Image taken following precipitation of the PETN from 10-20 μ l of 1.0g/l solution. The grid cell size is 50 μ m.

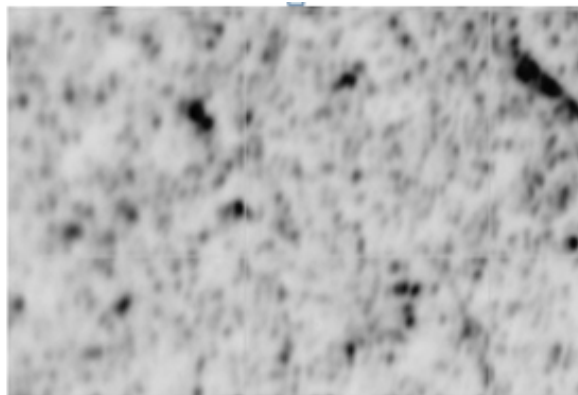


Figure 6. Typical optical microscope image of the RDX layer on the QCM electrode. The layer obtained by precipitation of 40 μg RDX from a solution of 1g/l. The sample seem to be composed of a nearly uniform thin film. The grid size in the picture is 50 μm .

All the experiments were carried out in an oven with fixed temperature whose variation was up to 0.1 degrees and with air flow during the measurements. During the experiments we followed the sample weight variation.

The sublimation rates we obtained for PETN and RDX at different temperatures are shown in Figs. 7 and 8 respectively.

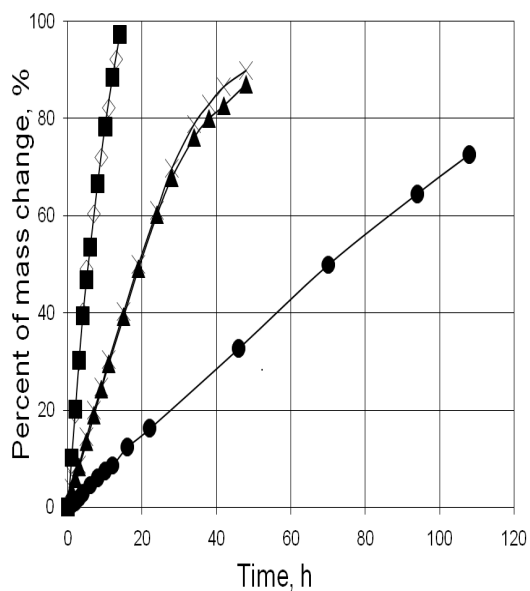


Fig. 7: Variation of PETN sample mass fraction as a function of time. The three groups of lines correspond to different temperatures at which sublimation was monitored: diamonds and filled squares – at 70°C, crosses and filled triangles - at 60°C and filled circles - at 50°C.

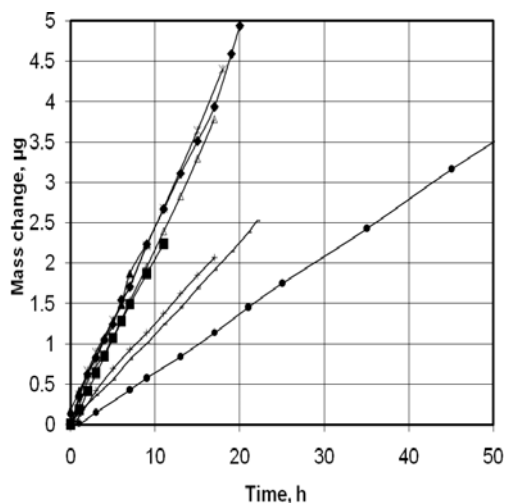


Figure 8. Sample mass change during RDX Sublimation at three different temperatures: leftmost group - at 70°C, middle group – at 65°C and right line with filled circles – at 60°C.

These results were analyzed using the simple diffusion model described last year to obtain the Arrhenius curves for the two explosives. These results are shown in Fig. 9 and 10 for PETN and RDX respectively.

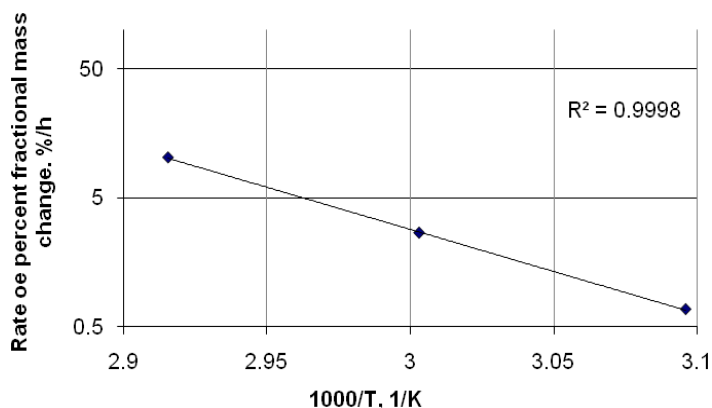


Fig9 Arrhenius plot of experimental data for PETN. Activation energy obtained is 125±13 kJ/mol

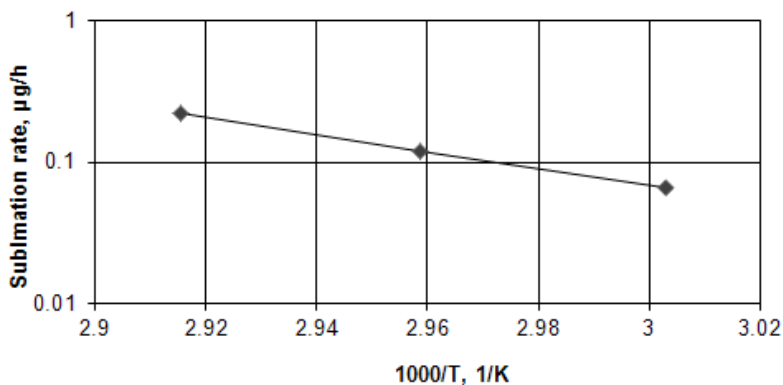


Fig 10. Arrhenius plot of experimental data for RDX. Activation energy is 114±22 kJ/mol.

The data describing the sublimation of PETN and RDX particles was used together with the diffusional model to obtain the disappearance curves of such particles. These curves for two initial particle sizes of each explosive are presented in Fig. 11 below.

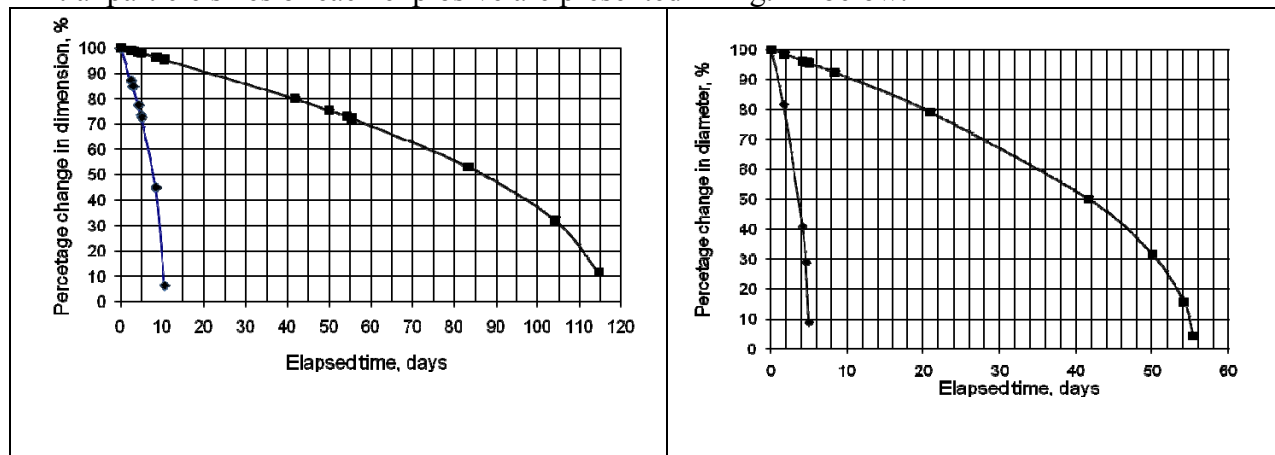


Figure 11. Left side: RDX hemispherical particle size evolution in time at 30 °C: diamonds represents particle of 6 μm initial diameter, squares is for particle of 20 μm initial diameter; Right side: PETN hemispherical particle size evolution in time at 30°C: diamonds represents particle of 6 μm initial diameter, squares corresponds to the time evolution of a particle with 20 μm initial diameter.

This type of data allows one to estimate the life time of various size particles on a substrate.

Students Supported

Yevgeny Zakon – is a M.Sc. student who was partially supported during the last two years. He finished his Master's thesis that was approved about 4 months ago. He carried out most of the AFM.

Raya Zach – A retired technician who works in my laboratory 2-3 days a week. She is involved in the preparation of explosive coated particles. Raya is seen below near the stand alone DMS system.

Pas Elia – is a PhD student who started his graduate studies 18 months ago and is partially supported. Pas is mainly involved in extension of the Aerodynamic approach to be used with sub micron particles, and is involved in HPLC, IMS and DMS measurements started a few months ago.

Arcady P. Gershanik – Retired physicist who works 2-3 days a week and is partially supported. Arkady carried out all the QCM measurements described.

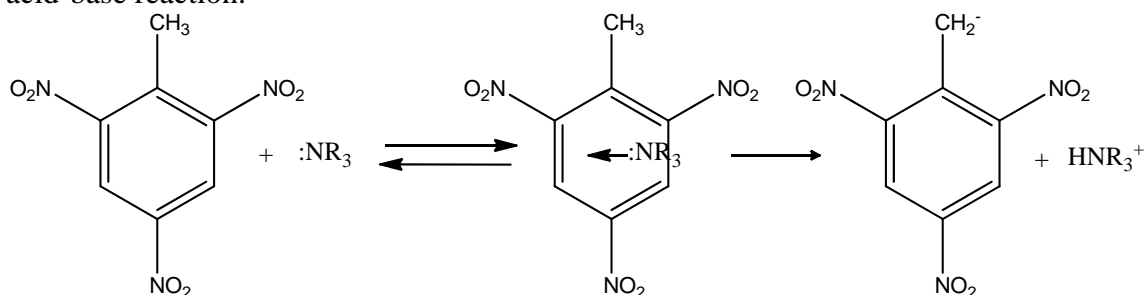
Sigal Ragol - is an undergraduate student working (2 days a week) on the aerodynamic approach to study adhesion.

Conference & Journal Publications

1. I participated and presented a poster in the "Detecting Illicit Substances: explosives & Drugs" Gordon conference, June 2011, Italy.
2. The paper on PETN and RDX sublimation was sent for publication in PEP, it is in press.
3. Two papers related to the AFM measurements are being written at present.

New Sensors for Explosives Detection
William B. Euler
Chemistry Dept.; University of Rhode Island

One of the common approaches to detecting TNT is to use the reaction between TNT and amines to give a colored product, which is then detected optically. We decided to use this approach coupled to our porous materials to improve the detection limits for TNT detection. Upon investigation of the reactivity of amine bases with TNT we found that the assumption that the Meisenheimer complex was responsible for the colored species was wrong. Our kinetic data suggest that the mechanism is the fast formation of a charge-transfer complex followed by an acid-base reaction.



The visible spectrum for the reaction between amines and TNT evolve from a spectrum with a higher energy maximum (~ 485 nm) in the first few seconds to a spectrum with a lower energy maximum (~ 510 nm). An example of this for the reaction between TNT and butylamine is shown in Figure 1.

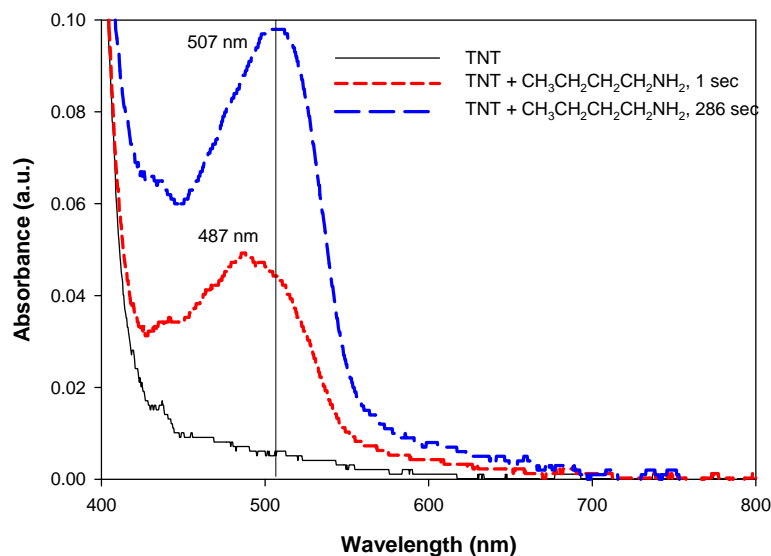


Figure 1. Visible spectra of TNT (black line), TNT plus equimolar butylamine after 1 sec (red dashed line), and TNT plus equimolar butylamine after 286 sec (blue dashed line). All reactions are run in THF. The vertical line shows the peak maximum at longer times, showing the low energy shift from the short time spectra.

The spectrum with the 487 nm maximum is assigned to the charge-transfer complex and the spectrum with the 507 nm maximum is assigned to the deprotonated TNT.

Owing to the multiple reactions and the two reactant stoichiometry, extraction of the rate constants is complicated. Assuming that the formation of the charge transfer complex reaches steady state after a few minutes, the long time rate constant can be found. Figure 2 shows the fits for several different bases. While the long time component is well fit, the initial kinetic changes still need to be modeled.

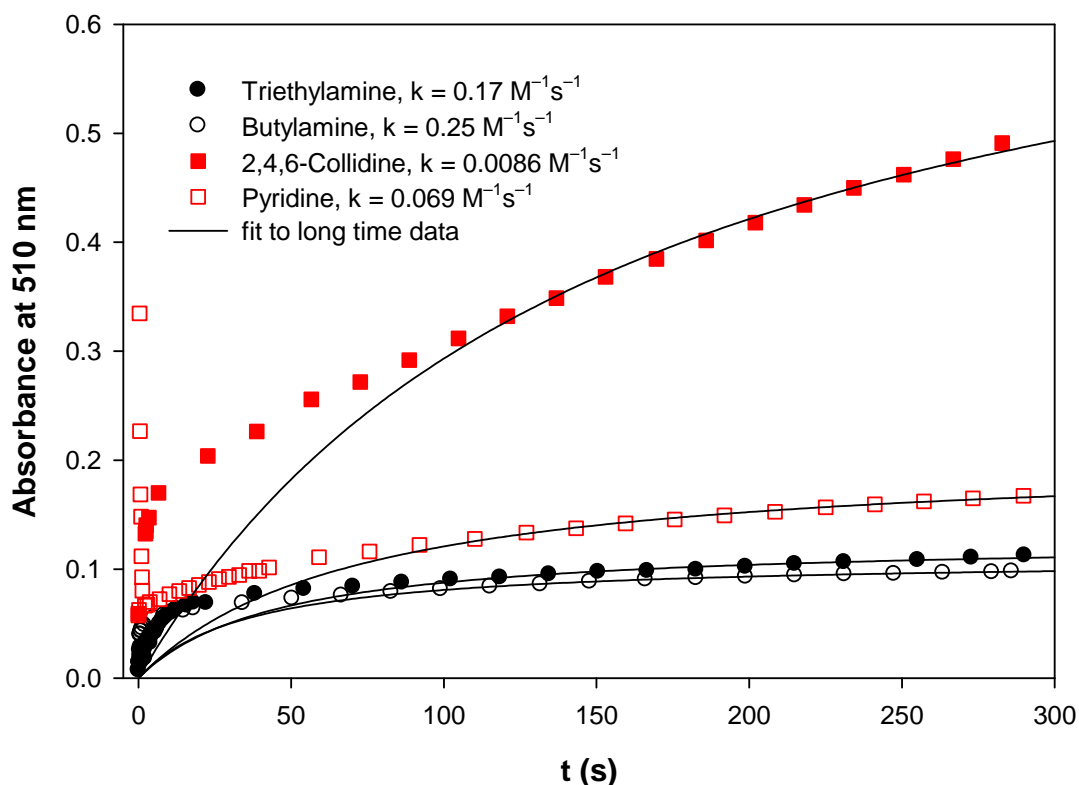


Figure 2. Absorbance at 510 nm for the reaction of TNT with triethylamine (filled black circles), butylamine (open black circles), 2,4,6-collidine (filled red squares), and pyridine (open red squares). All reactions are run in THF.

Even after many hours of reaction, there is little evidence of a Meisenheimer complex, as suggested by the ^1H NMR spectra shown in Figure 3. After 103 min of reaction there is little change in the NMR spectrum with the exception of migration of the NH_2 peak (initially at 1.027 ppm) from butyl amine (1.566 pm), which is exchanging with NH_3^+ from protonated butylamine. In the very long time spectrum, the exchanging peak has moved to 5.64 ppm. The TNT peaks at 2.667 ppm and 8.997 ppm have diminished considerably in the 62 hour spectrum and three new peaks are found at 1.620, 2.266, and 2.897 ppm, which are consistent with a deprotonated TNT anion.

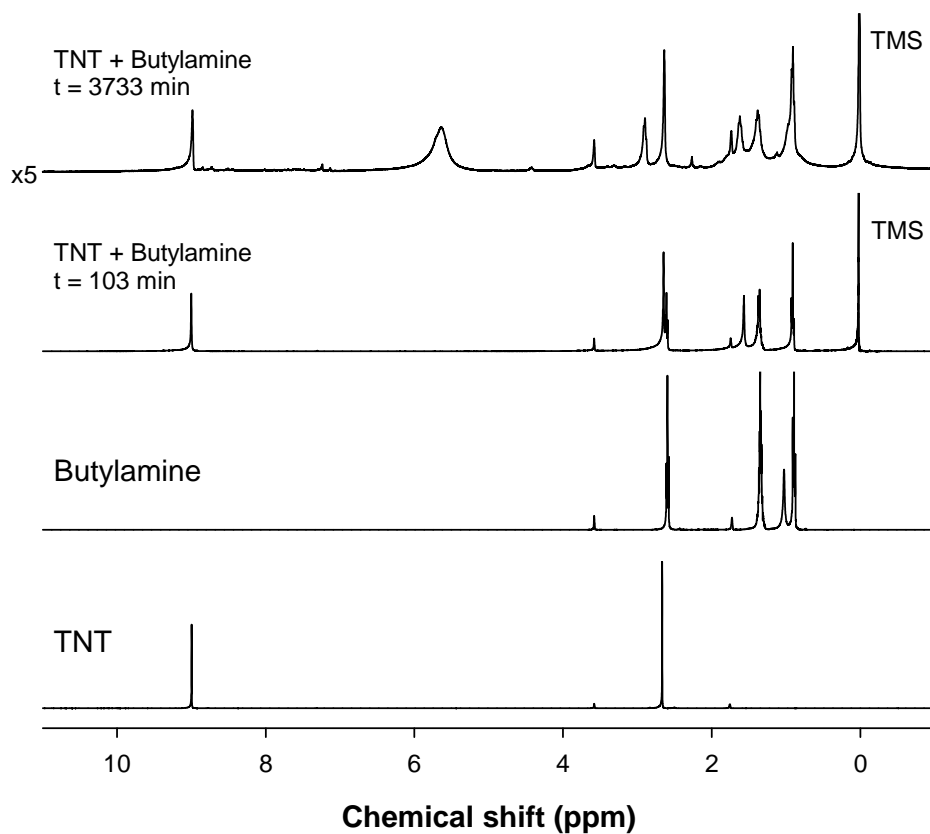


Figure 3. NMR spectra of TNT (bottom spectrum), butylamine (second from bottom), the reaction between TNT and butylamine after 103 min (second from top), and the reaction between TNT and butylamine after 3733 min (top spectrum, intensity multiplied by 5). All spectra were taken in THF-d₈.

Understanding that the reaction of amines with TNT leads to acid/base reactivity will allow us to tune the reaction to maximize the absorption response in the visible spectrum. This will lead to more sensitive and more selective sensors.

Graduate Students: Christopher Latendresse, Meredith Matoian
Undergraduate Students: Syrena Fernandes, JungMin Hwan, Jessie You

Development of Resonating Nanocantilever Chemical Vapor Sensors and Thiol Encapsulated Gold Nanoparticle Chemiresistors

Nathan S. Lewis

California Institute of Technology

I. Objective

We aim to develop new classes of chemiresistive sensors capable of detecting light gases and vapors, including explosives. These cheap to fabricate and easy to multiplex chemiresistive sensors will improve sensitivity and range of electronic noses, enabling them to detect a wider range of threats to security. Further, we are working toward the realization of a nanoscale electronic nose, which could be embedded in everyday devices like cell phones or incorporated into lab-on-a chip systems such as micro-gas chromatographs, through the development of resonating nanocantilever sensors.

II: Accomplishments

We published two detailed studies on thiol capped Au nanoparticle chemiresistor sensors. In one study, it was found that for a homologous series of thiol capping agents with variable chain length, resistance change upon exposure to chemical vapors increased with increasing chain length, and that interparticle distance and/or morphology change dominates the response. We also produced two conference presentations on using surface initiated polymerization to grow thick sorptive films on nanocantilever chemical vapor sensors. Masking and passivation were used to localize polymer growth to specific areas of the nanocantilevers, elucidating the role of competing response mechanisms in observed frequency shifts. Growing polymers of varying glass transition temperature revealed that polymers with low glass transition temperatures led to greatly increased sensitivity and linearity, as well as reduced response time.

III: Details

Progress Toward Nanoscale Electronic Nose

Heather McCaig, Ed Myers, Derrick Chi, Xinchang Zhang, Nathan S. Lewis, Michael L. Roukes

1) Ultrafast GC with Nanocantilever Detectors

Micro-gas chromatography systems could be tailored for explosive detection by use of proper stationary phases and backend detector functionalization. Currently, the lack of optimal back-end detector technology is a major roadblock to realizing these systems. Recently resonating nanocantilevers have demonstrated mass sensitivities below the attogram scale (10^{-18} g) at atmospheric pressures.¹ Combining an ultrafast GC with two nanocantilever sensors as backend detectors, chromatographic analysis of 13 chemicals was performed within a 5-second time window.² Nanocantilevers offer potential benefits for developing fully integrated portable analysis systems where sample collect, GC separation, and detection stages could be combine on a single substrate.

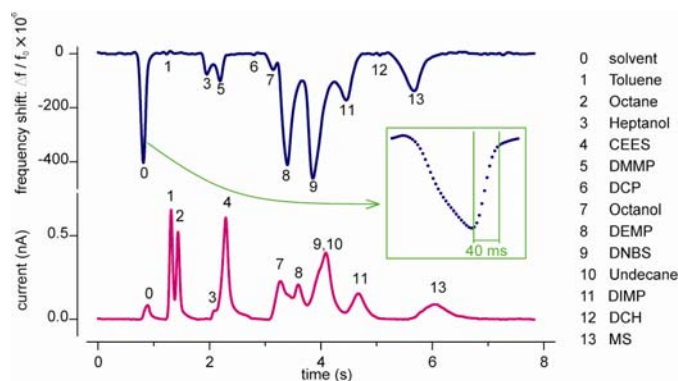


Fig. 1: Rapid chromatographic separation and nanomechanical detection of thirteen mixed chemical compounds.² Chromatograms from a NEMS resonator (top, blue) and a downstream FID detector (bottom, red) acquired simultaneously for comparison. The DKAP polymer-coated NEMS resonator showed high selectivity to organophosphate compounds such as DMMP, DEMP, and DIMP, as shown by the correspondingly strong peaks. Inset: Expanded view of the solvent peak, showing a 90% sensor recovery time of 40 ms.

1) Mo Li, H.X. Tang, M.L. Roukes. *Nature Nanotech.* **2007**, 2, 114-120.

1) Mo Li, E. B. Myers, H. X. Tang, S. J. Aldridge, H. C. McCaig, J. J. Whiting, R. J. Simonson, N. S. Lewis, M. L. Roukes. Nanoelectromechanical resonator arrays for ultrafast, gas-phase chromatographic chemical analysis. (2010) *Nano Letters*. **10** (10), 3899-3903.

2) Nanocantilever and Chemiresistor Sensor Array Performance Comparison

The miniaturization of electronic noses must not come at the cost of performance degradation. To determine if the chemical specificity imbued by polymer coatings remains adequate when employed on the nanoscale, an array of five nanocantilevers coated with different polymers spanning a range of chemical functionalities was shown to perform equivalently to an array of macroscale polymer/carbon black chemiresistors utilizing the same set of polymers. The vapors were exposed at 0.02 P/Po (vapor pressure / saturated vapor pressure) and in random order. The difference in data spread is indicative of the difference in sensing mechanisms between nanocantilevers and chemiresistors. The minimum chemiresistor footprint required to maintain a signal to noise ratio (SNR) equal to that of a nanocantilever (1.5 μm^2 capture area) was 1.17 mm^2 .

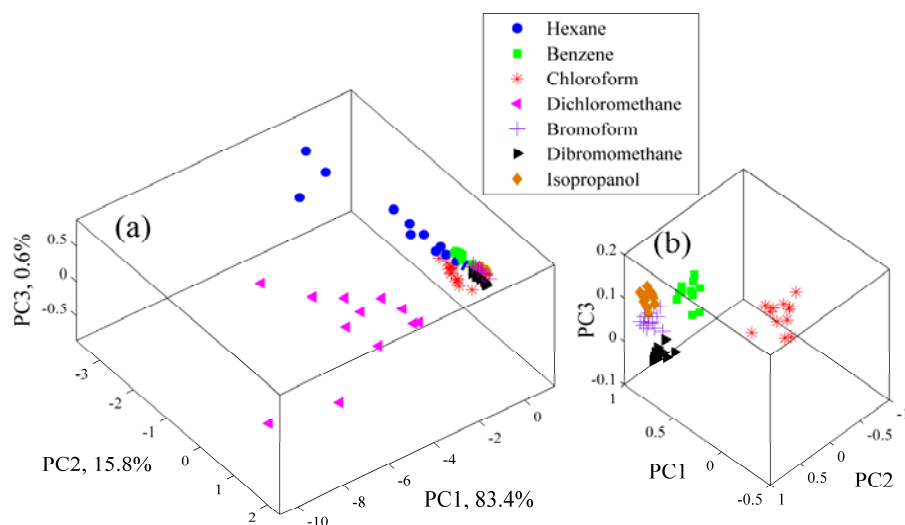


Fig 2: Principal Components Analysis (PCA) of nanocantilever sensor array responses to a series of chemical vapors with a background of dry nitrogen. (a) All analyte vapors. (b) Zoom in of analyte vapor cluster in (a) shows perfect separation of nearly all vapors.

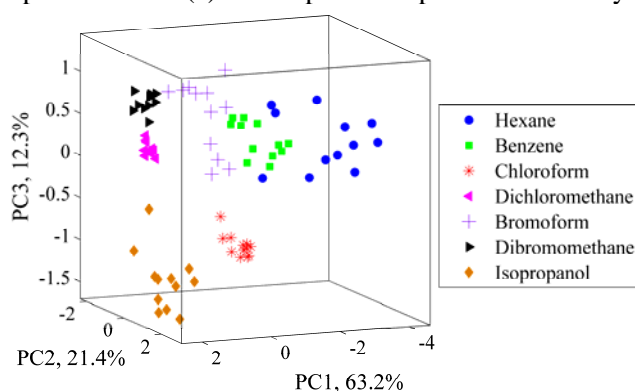


Fig 3: Principal Components Analysis (PCA) of chemiresistor sensor array responses to a series of chemical vapors with a background of dry nitrogen.

3) Enhancing Sensitivity of Nanocantilever Chemical Vapor Detectors Through Localized Surface Functionalization

Nanocantilever chemical vapor sensors respond to the presence of analyte vapor through multiple competing mechanisms including mass loading, which induces a negative shift in resonance frequency, stiffening, which induces a positive shift in resonance frequency. To investigate these mechanisms and enhance sensitivity, we have developed a method to grow thick polymer films on isolated areas of the nanocantilevers. Sections of the cantilever were masked by chromium, and then thiol chemistry along with atom radical polymerization (SI-ATRP) of polymethylmethacrylate (PMMA) was used to produce films as thick as 80 nm on the gold portions of the nanocantilevers. Polymer films of this thickness sorb significant quantities of vapor and overwhelm the effect non-specific physisorption of vapor molecules onto non-gold surfaces.

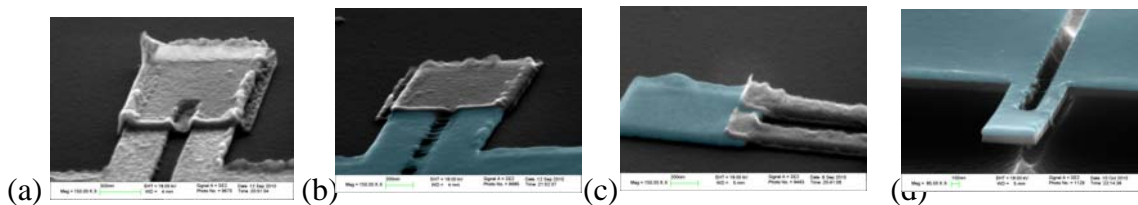


Fig 4: SEM images of (a) bare unsuspended nanocantilever; gold legs and chromium masked tip. (b) PMMA growth is isolated to exposed gold areas of an unsuspended nanocantilever. (c) PMMA only film isolated to Au tip of a Cr-masked cantilever. (d) PMMA grown on the entire surface of an unmasked, suspended cantilever.

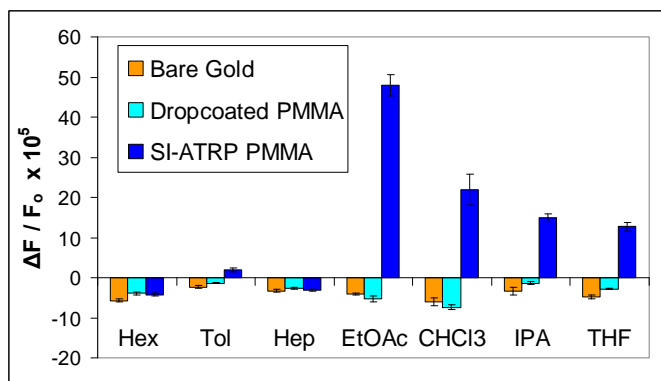


Fig 5: Unmasked nanocantilevers coated 80 nm thick SI-ATRP grown PMMA film shows enhanced sensitivity to polar vapors. Vapors were exposed at 0.02 P/P⁰.

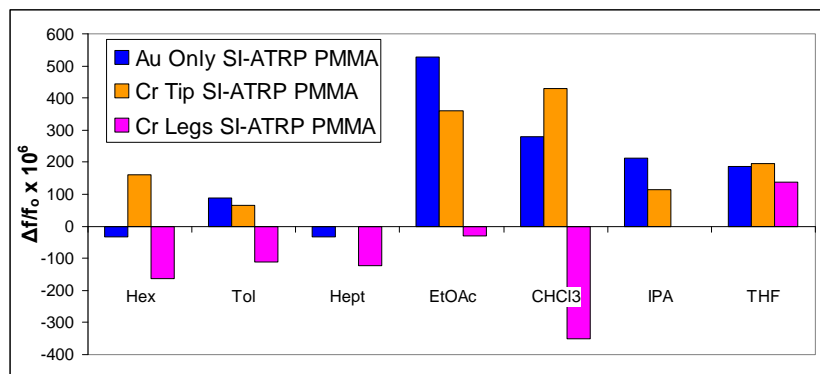


Fig 6: Comparison of unmasked and Cr-masked nanocantilevers coated with approximately 80 nm SI-ATRP grown PMMA films. Preventing polymer growth at the clamped end (cantilever legs) changes response pattern. Placement of polymer film can be used to enhance sensitivity of particular poly/analyte pairs.

4) Enhanced Sensitivity of Nanocantilever Chemical Vapor Detectors through Surface Initiated Polymerization of Thick Polymer Films with Low Glass Transition Temperatures

Vapor sorption onto nanocantilevers affects both the mass and the stiffness of the sensors, leading to shifts in the resonance frequency. Mass accretion drives resonance frequency lower while an increase in effective spring constant (due to polymer film swelling or other surface stress changes) drives the resonance frequency higher, such that these two response mechanisms are capable of cancellation under certain conditions. Even if frequency shifts are observed upon exposure to a chemical vapor, the magnitude of the response can be depressed by these competing mechanisms. By utilizing a polymer that maintains a very low glass transition temperature (T_g) in a surface-bound 100 nm thick film, the affects of polymer-induced mechanical strain on the nanocantilever sensor is minimized. Thus the observed response is strongly enhanced.

In this study the performance of nanocantilevers functionalized with SI-ATRP grown films of poly(methyl methacrylate) (PMMA, bulk $T_g \sim 70^\circ\text{C}$), poly(methyl acrylate) (PMA, bulk $T_g \sim 10^\circ\text{C}$), and polymer(butyl methacrylate, bulk $T_g \sim 15^\circ\text{C}$) were compared. Films ranged from approximately 40-90 nm thick, and were grown from the top, Au coated, surface of the nanocantilevers. The sensors were then exposed to a series of analyte vapors at concentrations ranging from 0.005 – 0.08 P/P^0 (where P and P^0 are the partial pressure and saturated vapor pressure, respectively). The two methacrylate polymers produced smooth films, while the acrylate polymer produced thinner, rough films. The PBMA coated nanocantilevers exhibited greatly improved sensitivity and response relative to the previously tested PMMA coated nanocantilevers. The PMA coated nanocantilevers did not exhibit enhanced sensitivity and only moderately improved response time, which is believed to be caused by an increase in T_g relative to the bulk, as has been shown to occur for some thin films of polymer brushes.

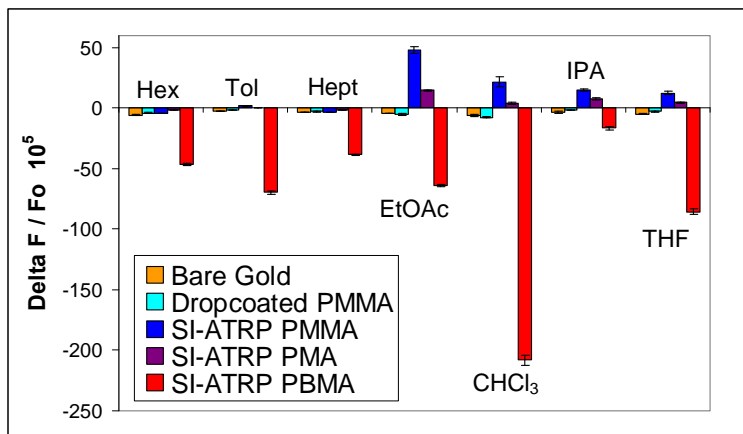


Fig 7: PBMA coated nanocantilevers show strongly enhanced sensitivity to all analyte vapors tested.

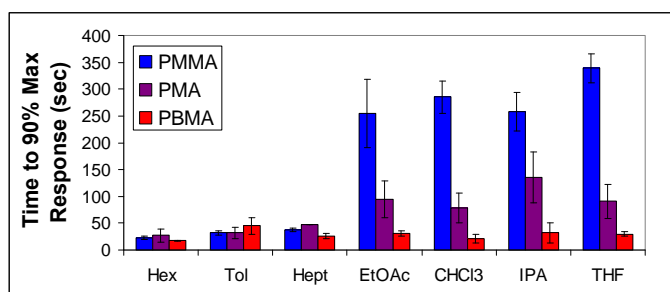


Fig 9: PMBA coated cantilevers show greatly reduced response time due to low Tg and thus high coefficient of diffusion for vapors absorbing into the film.

Synthesis of π -Conjugated-Thiol Encapsulated Au Nanoparticles for Chemical Sensing

Edgardo Garcia-Berrios, Nathan S. Lewis

Our laboratory have been exploring alkylthiol-capped Au nanoparticles as chemiresistive organic vapor sensors to investigate whether the sensitivity to a given vapor increases or decreases as the chain length of the capping agent is increased, and elucidate the mechanisms of vapor detection by such capped nanoparticle chemiresistive films. Passivated Au nanoparticle films have been exposed to a variety of organic vapors, where their response (e.g. change in conductivity) is induced by sorption of the organic vapor into the organic interparticle matrix, which results in an increase in the interparticle spacing. The electronic conductivity, of organothiol-capped Au nanoparticles can be related to the rate constant for electron transfer between metal nanoparticles separated by a dielectric medium. The electronic conductivity has been shown to be given by:

$$\sigma = \sigma_0 \exp[-\delta\beta] \exp[-\Delta G^\circ/kT] \quad (1)$$

where δ is the interparticle distance that is proportional to the number of methylene units; β the electron transfer coupling coefficient, which is a function of the potential barrier height and the permittivity of the chemical environment between the metal cores; and ΔG° is the activation energy for transfer of an electron between two metal particles.¹

Upon exposure to organic vapors, analyte diffuses into the film, producing changes in the core-to-core distance and the dielectric permittivity of the medium, thus changing δ , β and ΔG° . Sorption of analyte is assumed to take place at the passivating organic layer of the metal particles, thus affecting the chemical environment surrounding the metal particles.

The electronic coupling term, β , describing tunneling through the alkylthiol layer is an important electronic parameter when considering the participation of the passivating ligand in the electron transfer. In principle, the lower the value of β , the higher the degree of participation of the passivating ligand in the electron transfer. For vapor detectors, and lower values of β , one would expect that sorption of analyte into the passivating layer would cause a higher change in the conductivity of such films. The proposed materials are oligo(*para*-phenylenevinylene) methyl thiols (OPPT) ($\beta = 0.4$).² OPPT have been synthesized with different lengths and functionalities by using wet chemical techniques, and showed long term stability. Au nanoparticles capped with OPPT will be developed in order to study their sensing performance.

References

- (1) Terrill, R. H.; Postlethwaite, T. A.; Chen, C. H.; Poon, C. D.; Terzis, A.; Chen, A. D.; Hutchison, J. E.; Clark, M. R.; Wignall, G.; Londono, J. D.; Superfine, R.; Falvo, M.; Johnson, C. S.; Samulski, E. T.; Murray, R. W. *Journal of the American Chemical Society* **1995**, *117*, 12537-12548.
- (2) Liang, T. T.; Azebara, H.; Ishida, T.; Mizutani, W.; Tokumoto, H. *Synthetic Metals* **2004**, *140*, 139-149.

IV. Students Supported

Heather McCaig: PhD Subject: Resonating nanocantilever chemical vapor sensors.

Edgardo Garcia Berrios (defended May 2011): PhD Thesis Title: Investigation of Composites of Carbon Black and Metallocycles, and Functionalized Transition-Metal Nanoparticles as Chemiresistive Vapor Sensors.

V. Journal Publications

- 1) Mo Li, E. B. Myers, H. X. Tang, S. J. Aldridge, H. C. McCaig, J. J. Whiting, R. J. Simonson, N. S. Lewis, M. L. Roukes. **Nanoelectromechanical resonator arrays for ultrafast, gas-phase chromatographic chemical analysis.** (2010) *Nano Letters*. **10** (10), 3899-3903.
- 2) E. Garcia-Berrios, T. Gao, J.C. Theriot, M.D. Woodka, B.S. Brunschwig, N.S. Lewis. **Response and Discrimination Performance of Arrays of Organothiol-Capped Au Nanoparticle Chemiresistive Vapor Sensors.** (2011) *Journal of Physical Chemistry C*. **115** (14), 6208-6217.
- 3) . Garcia-Berrios, T. Gao, M.D. Woodka, S. Maldonado, B.S. Brunschwig, M.S. Ellsworth, N.S. Lewis. Response versus Chain Length of Alkanethiol-Capped Nanoparticle Chemiresistive Vapor Sensors. (2010) *Journal of Physical Chemistry C*. **114** (50), 21914-21920.

VI. Conference Presentations

- 1) H.C. McCaig, E. Myers, E. Chi, X. Zhang, N.S. Lewis, M.L. Roukes **Enhanced Sensitivity of Resonating Nanocantilever Chemical Vapor Sensors via Localized Sorptive Film Deposition.** American Institute of Chemical Engineers Annual Meeting 2010.
- 2) H.C. McCaig, E. Myers, E. Chi, X. Zhang, N.S. Lewis, M.L. Roukes. **Effect of Polymer film Glass Transition Temperature on Resonating Nanocantilever chemical Vapor Sensor Response.** American Chemical Society Spring Meeting 2011.

A Persistent Surveillance Technique for Detection of Explosives and Precursors

Otto Gregory & Michael Platek

Chemical & Electrical Engineering Depart, University of Rhode Island

Objective: The detection of explosives and explosive precursors in suspected “bomb labs” and other enclosed areas that terrorists may target for the deployment of improvised explosives (IED) is the goal of this project. The significance of this work has been highlighted by the failed attempt of "Shoe Bomber" Richard Reid to deploy a triacetone triperoxide (TATP) based IED, to initiate an explosive device containing PETN. The ability to detect energetic materials and their precursors at low concentrations in relatively confined spaces is of particular importance in such scenarios. A robust detection system must be sensitive enough to respond to minute concentrations of the target gas and not generate false positives. The early detection of specific gas molecules without interference effects from background gases continues to be our goal. TATP exhibits a sufficiently high vapor pressure that it can be detected directly in the gas phase. Therefore, our main focus this past year (2010-2011) has been to detect TATP and its precursors, hydrogen peroxide, acetone using our thermodynamic based sensor. Due to its relatively simple synthesis and available starting materials, TATP is the explosive of choice for many terrorists, including suicide bombers thus, the early detection of TATP and isolation of such individuals is essential to the security of the general population.

Accomplishments Year 3: The unambiguous detection of TATP using our current thermodynamic sensor platform is being reported for the first time. Since high purity, crystalline TATP has been recently synthesized and made available by Prof.'s Oxley and Smith at URI's Center for Explosive Detection, Characterization and Mitigation, controlled experiments using TATP as the target molecule in our laboratory are now possible. Nanogram quantities of TATP were fixed in filter paper to enable the safe handling of the explosive vapor at concentrations as low as 8 ppm (gas phase) range. Since we recently demonstrated that we can detect hydrogen peroxide at comparable levels using the same metal oxide catalysts, we compared the TATP and hydrogen peroxide responses to determine if the TATP was decomposing into hydrogen peroxide in the vicinity of the microheater. These results suggested that the catalytic decomposition TATP was occurring in the vicinity of the microheater. The response of a tin oxide catalyst and a tungsten oxide catalyst to TATP and hydrogen peroxide are shown in Fig. 1. It appears that the response of tin oxide and tungsten oxide catalysts to TATP and hydrogen peroxide occur at the same temperature and that the overall peak shape is the same in both cases.

Our detection technique employs a digital control system and a thin film micro-heater coated with a metal oxide catalyst, which enables the heater to be scanned over a selected temperature range. The electrical power difference due to catalytic reaction; i.e. the power difference between the micro-heater in air and in the presence of the target molecule was measured as a function of temperature for several metal oxide catalysts. Ultimately, by using arrays of micro-heaters, each with different catalysts, allows us to uniquely identify TATP in real time, while simultaneously minimizing false positives. The average amount of heat generated or absorbed by the catalyst in the presence of the target gas was calculated as the change in power required to maintain the sensor at a constant temperature and the percent response was the fraction of total power generated by the catalyst. These tests were conducted using both a dynamic pulsed gas and static gas scheme. When using the dynamic pulsed gas scheme, the sensor is initially run in air, followed by three minutes in various concentrations of the target gas, followed by an additional air flow, all without changing temperature. Static gas testing was performed by determining the power dissipation in air at each temperature, cooling the sensor to room temperature and running again in a target gas. Using the static test protocol, the sensitivity of electronics and drift in the resistance of the thin film micro-heaters allow for power differences greater than 8 mW to be

reliably detected, while the dynamic response technique allows for power differences as low as 1 mW to be reliably detected.

Fig. 2 shows the response of a CuO-Cu₂O and Cu₂O catalyst to 8 ppm acetone and 8 ppm H₂O₂ at 330°C. From this figure it can be seen that the relative response to acetone is considerably greater than that of H₂O₂. This can be explained by the significant exothermic heat effects observed for hydrocarbons by other investigators reporting on similar thermodynamic based gas sensors. Not only is the magnitude of the response to acetone for CuO-Cu₂O significantly greater (28 mW) than that of hydrogen peroxide (-2.5 mW) but it is also of opposite sign. This suggests that not only is the sensitivity of the thermodynamic sensor platform to acetone significantly greater than that of the other possible target gases derived from TATP, but the heat effect is also of opposite sign which implies that heat is being generated in the first case and being absorbed in the second. Since we do not see any evidence of acetone in the output signal when using TATP as the target gas, we can conclude that the TATP is detected as hydrogen peroxide through the catalytic decomposition of TATP, which is a much more specific reaction than the decomposition of TATP in air to form acetone. This has been extensively cited in the literature and the presence of this specific mechanism should help eliminate false positives by using this sensor platform. A number of other metal oxide catalysts were successfully used to detect TATP at similar concentrations, shown in Fig. 3. Each of the five oxide catalyst (WO₃-TiO₂, V₂O₅, SnO, Nb₂O₃ and ZnO) responses shown in Fig. 3, as a function of temperature, indicate characteristic signatures or features ranging from almost no peak response (of Nb₂O₃) to well defined peaks (of ZnO).

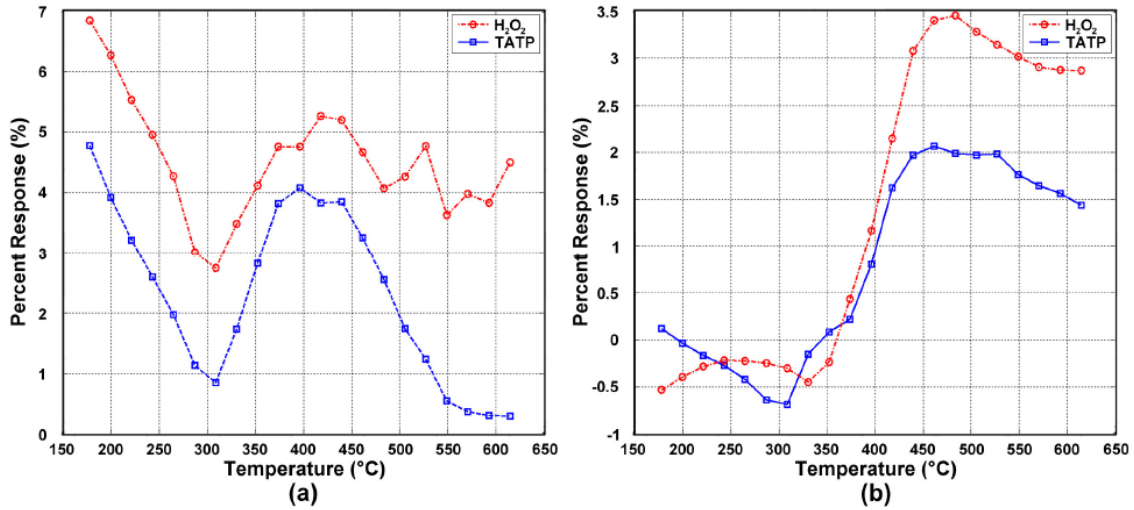


Fig. 1 Percent response in 8 ppm TATP and 9 ppm H₂O₂ as a function of temperature for (a) tin oxide and (b) tungsten oxide catalysts, measured using the static testing approach.

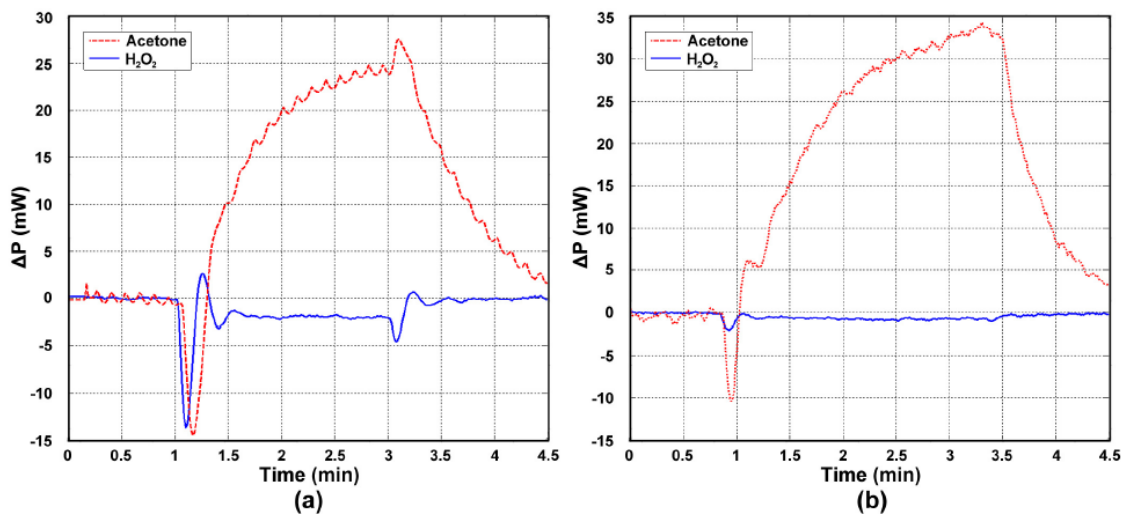


Fig. 2 Response of (a) CuO-Cu₂O and (b) Cu₂O in acetone and H₂O₂ at 330°C, measured using the manual testing approach.

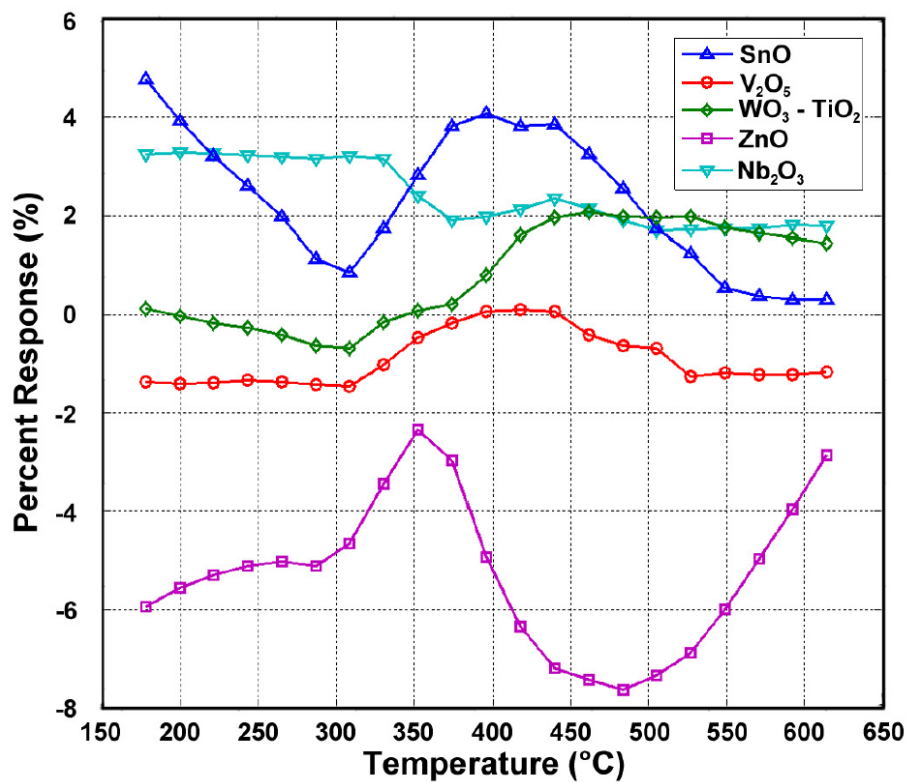


Fig. 3 Response as a function of temperature using several catalysts to detect TATP (8 ppm) measured using the static testing approach.

Most of the catalysts developed for the thermodynamic based gas sensors were prepared by sputtering and reactive sputtering from ceramic targets. In some instances, metal targets were employed and thus, in those cases the oxide catalysts were prepared by reactive sputtering in argon/oxygen plasmas. The oxidation states of the copper oxide catalysts prepared from ceramic and metallic targets were determined by XPS (Fig. 4). In figure 4, the Cu 2p spectra of those copper oxide films prepared by reactive sputtering in an Ar/O₂ plasma from a metallic target (dashed line) were compared to copper oxide films prepared by sputtering in an Ar plasma from a CuO target (solid line). The significant difference between the spectra is that the films prepared from ceramic targets contain satellite peaks which are typically found 7 to 10 eV above the main peaks associated with the copper 2p_{3/2} and 2p_{1/2} electrons respectively for Cu²⁺ compounds, and correspond to shake-up electrons with 2p3d⁹ character. In this film, the copper 2p_{3/2} and 2p_{1/2} peaks were found at 929.65 and 952.65 eV (Cu⁺), respectively, furthermore curve fitting of the main 2p_{3/2} peak revealed a second peak with lower amplitude at 931 eV (Cu²⁺). The broadening of the 2p_{3/2} peak towards higher binding energies combined with the presence of the satellite peaks suggests that these copper oxide films prepared by sputtering from ceramic targets in an Ar plasma have mixed oxidation states. On the other hand, by sputtering in Ar/O₂ plasma from an oxide target, a narrow 2p_{3/2} peak at 929.65 eV was observed and no satellite peaks were present, indicating that the film is largely composed of Cu₂O.

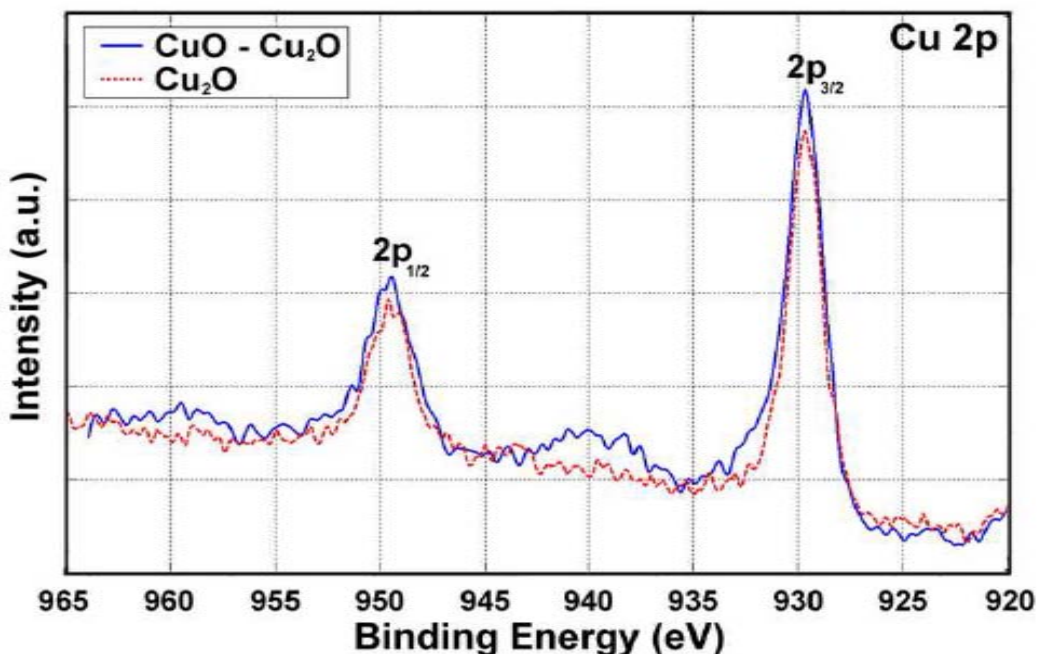


Fig. 4. XPS spectra of Cu₂O films prepared by sputtering in an Ar/O₂ plasma from a metal target (dashed line) and CuO-Cu₂O films prepared by sputtering in an Ar plasma from a CuO target (solid line).

Fig. 5 shows the microstructure of several oxide catalysts sputtered from metallic and ceramic targets in different Ar/O₂ partial pressures. CuO-Cu₂O films with mixed oxidation states, which were sputtered from a ceramic target in argon plasma, show surfaces devoid of any fine structure and exhibit relatively smooth rounded protuberances and small surface area, typical of an as-deposited film (Fig. 5 a). However, the Cu₂O films reactively sputtered from a metallic target in Ar/O₂ mixtures, exhibited a microcrystalline surface morphology within the rounded protuberances of the as-deposited films, unlike those films prepared using a ceramic target (Fig. 5 c)

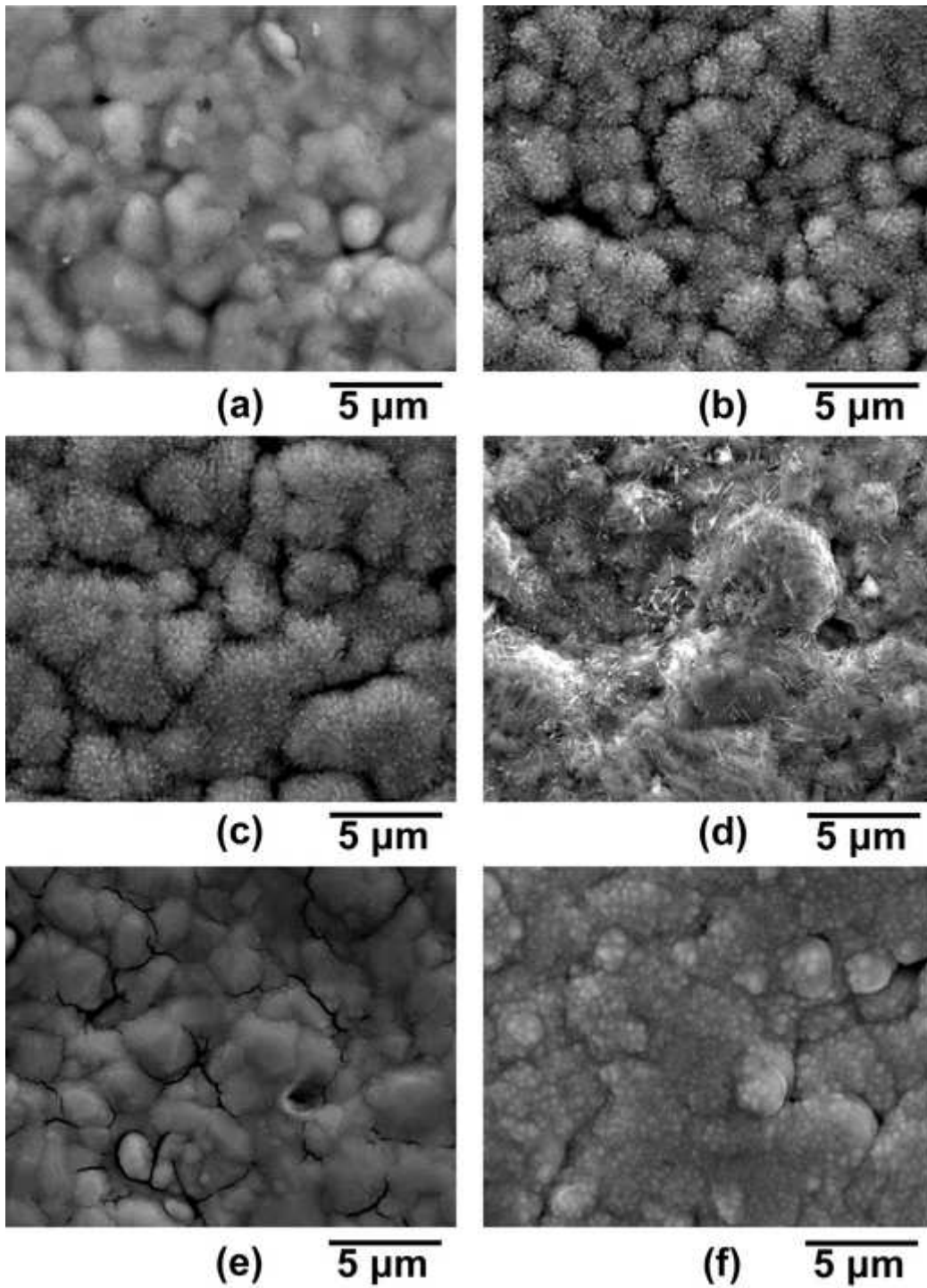


Fig. 5. SEM micrographs of (a) $\text{CuO-Cu}_2\text{O}$ after testing, Cu_2O (b) before and (c) after testing and (d) V_2O_5 , (e) ZnO and (f) SnO after testing

Catalyst development for existing sensor platforms was also a major focus of the project over the past year and was particularly important as new sensor platforms were developed (next section) to improve sensitivity, selectivity and response times. Even though the bulk of the catalysts were prepared from ceramic targets, we could control the oxidation state of the oxide to some extent by controlling the oxygen partial pressure in the plasma during sputtering. For example, the oxidation states of two different tin oxide catalysts prepared from the same ceramic target is shown in Fig. 6; one tin oxide catalyst was prepared by reactive sputtering in an oxygen/argon plasma and the other was prepared in an argon plasma. This result demonstrates that the catalyst oxidation state can be “tweaked” by adjusting the sputtering parameters to obtain the desired sensitivity, selectivity and response. In all instances the sputtered oxide catalysts require a post deposition heat treatment. In addition, this result also provides insight into the small changes in oxide chemistry by changing the gas phase during sputtering and that small changes in oxide chemistry are possible by co-sputtering, which is related to our catalyst discovery efforts using combinatorial chemistry. Using combinatorial chemistry techniques, we have continued to develop novel oxide catalysts for our various sensor templates.

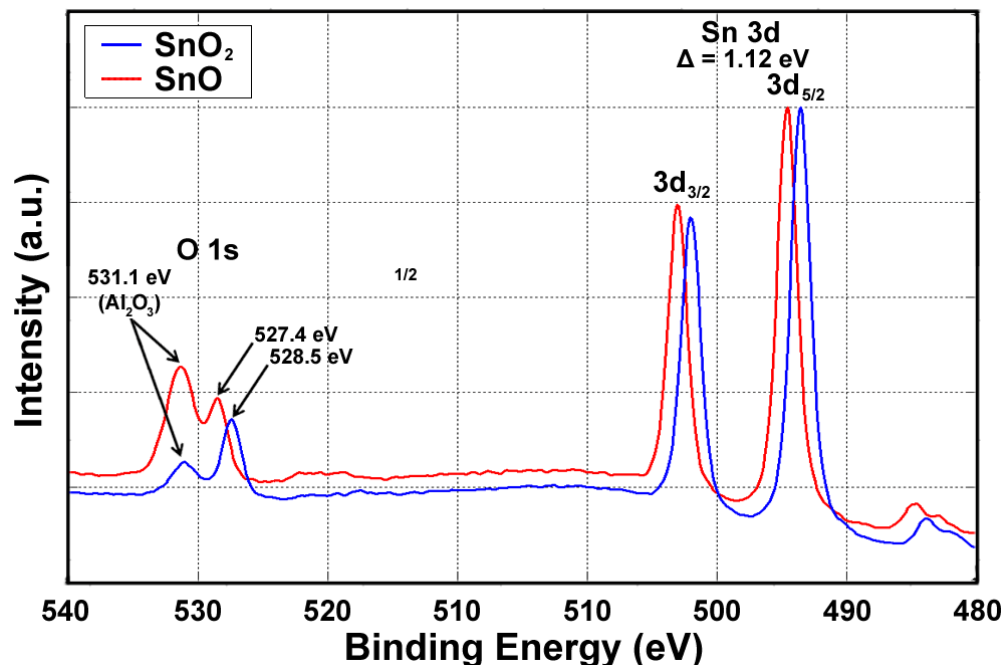


Fig. 6. XPS spectra of a SnO₂ film prepared by sputtering in an Ar/O₂ plasma from a ceramic target (blue line) and a SnO film prepared by sputtering in an Ar plasma from a SnO₂ target (red line).

Sensor Templates: Over the past year, we have developed several versions of a MEMS based sensor platform with the overall goal to build arrays of microheaters that would employ multiple catalysts and combine the characteristic response curves to uniquely identify the target molecules of interest. This would add a second independent variable to minimize false positives and improve long term stability of our existing gas sensor template. In addition, the reduced thermal mass afforded by these MEMS based sensor platforms would greatly improve the sensitivity, selectivity and response time for the detection of explosives and explosive precursors. These MEMS efforts are described in detail below and represent a combination of in-house fabrication efforts and foundry efforts to deliver the desired final sensor platform. We have been developing several MEMS based sensor platforms in parallel and now have three platforms in various states

of completion; our Generation 0 MEMS platform is farthest along followed by our in-house MEMS platform and finally the Generation 1 MEMS platform which is only in the design stages.

MEMS Development Efforts: The next logical step in the development of gas sensors was to move the platform from a ceramic chip (substrate) to an integrated circuit based on silicon. In this way the die sizes could be considerably reduced to levels on the order of 2mm x 2mm, allowing for a practical realization of a sensor array with multiple catalysts. Other obvious advantages to a MEMS based sensor platform are portability, low cost fabrication and the possibility of forming large arrays of microheaters in a small footprint sensor. Currently, we are developing a micro-heater based sensor platform in a standard CMOS process. The goal is to integrate electronic components for measurement, automatic detection and even communication onto a substrate which is shared by the sensor. The IC can be organized in such a way to facilitate additional processing steps such as catalyst deposition as well as bulk and surface micro-machining. These steps can be performed once the integrated circuits are fabricated (e.g. post processing).

Our first CMOS IC fabrication effort, Generation 0, was prepared as a simple proof of concept. A platform consisting of a simple heater (metal serpentine resistor) in a pad frame was fabricated. Fifty die were fabricated during the spring of 2011 and we have prepared the die for testing in our existing setup (Fig. 7). This includes masking steps to prevent the catalyst from covering the bond pads and catalyst deposition via rf sputtering. The Generation 0 testing will proceed through the Fall 2011 semester and we are expecting to reproduce the results of experiments performed using our current alumina substrates with nickel thin film microheaters.

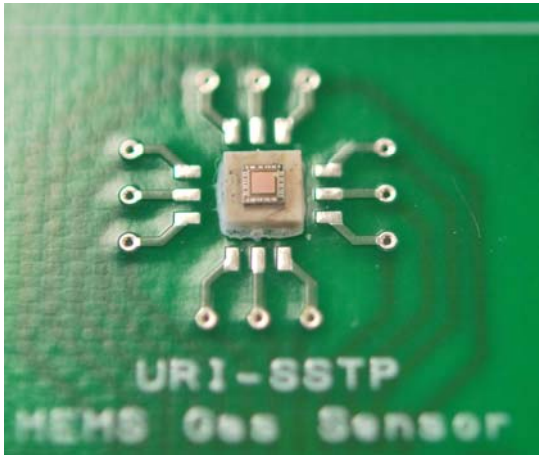


Fig. 7. Photograph of a Generation 0 MEMS chip (sensor element) ready for wire bonding and then testing. The chip measures 1.5 mm x 1.5 mm and consists of fine microheater elements covered with an oxide catalyst and bond pads that will be connected to the PCB carrier.

Our next generation CMOS IC design (Generation 1) is already complete, and is being prepared for fabrication. These die will incorporate multiple temperature sensors and 4 micro-heaters implemented via a suspended trampoline (Fig. 8). The trampoline and microheater will be fabricated using polycrystalline silicon, where the bulk silicon under each trampoline will be etched away using a TMAH etchant. The etching step used here has already been perfected in our in-house MEMS effort, described in the next section. We should take delivery of a small set of these die in the spring of 2012. Furthermore, these new sensors will be compatible with the masking, mounting, and bonding steps already used for the generation 0 devices. Additional

Generation 1 efforts include the development of infra-red temperature measurement capability and at some point during the current year we will be submitting prototypes of MEMS ICs which will incorporate these IR sensors.

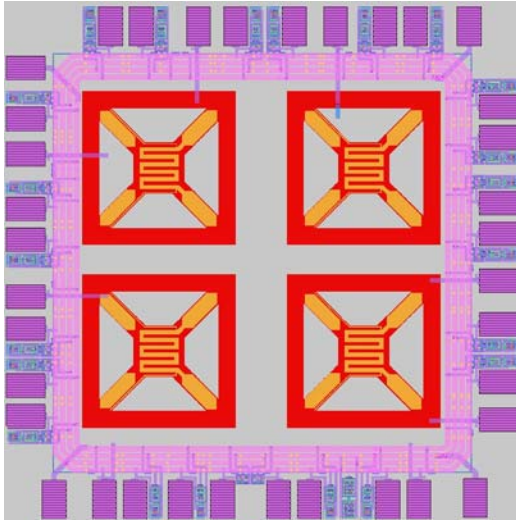


Fig. 8. MAGIC Layout of the generation 1 MEMS sensor, containing four polysilicon heaters with supports that will be micro-machined to for suspended membranes at after fabrication.

We are also working on an in house MEMS sensor which will be formed by back etching of a double side polished silicon wafer. As shown in Fig.9, these devices will be fabricated by etching thin (10-20 micrometers in thickness) silicon membranes in an oxidized silicon wafer (Fig.10), which is then anodically bonded to a second pyrex wafer for mechanical support. Thin film microheaters and temperature sensors will subsequently be deposited on the membranes.

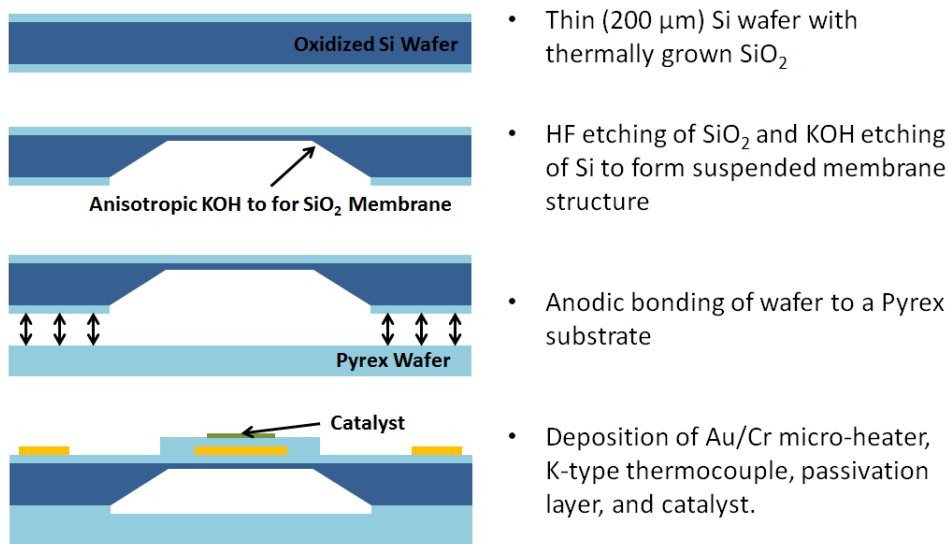


Fig. 9. Process chart for preparing a simple internal MEMS based gas sensor.

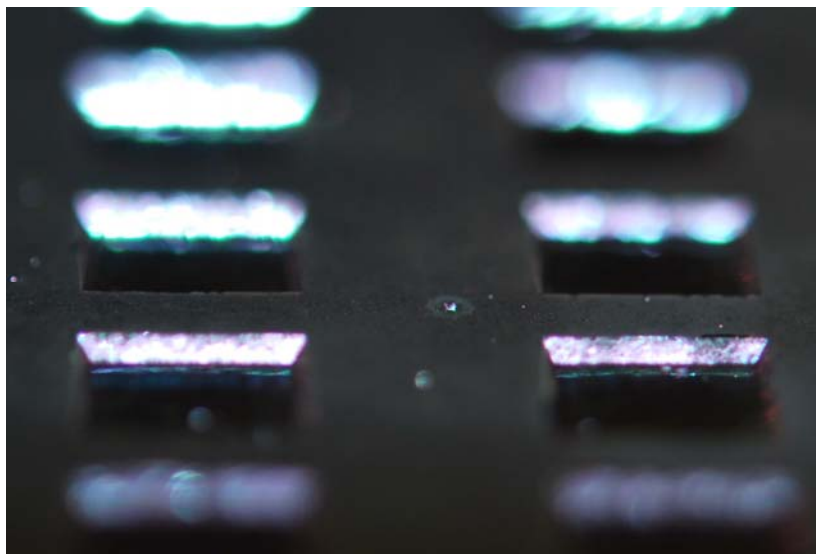


Fig.10. Photograph of etched membranes on the back side of a silicon wafer, used to reduce the thermal mass of the support used for the microheater.

During CMOS processing only a select number of materials (doped/undoped polysilicon and aluminum) are used as interconnects and due to the relatively low melting point and recrystallization temperature of aluminum, its use as an electrode or heater material is rather limited ($T < 450^{\circ}\text{C}$). In our internal MEMS platform, we have choice over metallization, and are fabricating devices capable of acquiring both thermodynamic and chemoresistive signals from the catalysts, which should provide us with two independent measurements for each catalyst and help reduce the risk of false positives.



Undergraduate Students Supported by the DHS Project

Caitlin Hurley; Chemical Engineering major

Kellie Waterman; Chemical Engineering major

Joe Ferro; Chemical Engineering major

Hope High School, Providence RI (Summer 2011 supported by the DHS Project)

Anthony Fascia; Chemistry and Physics teacher

Graduate Students Supported by the DHS Project

Matin Amani; Electrical Engineering MS; Chemical Engineering undergraduate student

Yun Chu; Chemical Engineering PhD student

Carson Pryde; Chemical Engineering MS student

Papers, Posters and Presentations

Matin Amani, Yun Chu, Kellie Waterman, Caitlin Hurley, Mike J. Platek and Otto J. Gregory, "Detection of Triacetone Triperoxide (TATP) Using a Thermodynamic Based Gas Sensor", **Sensors and Actuators B: Chemical**, in press.

219th Electrochemical Society Meeting, Montreal Canada, May 2011, "Detection of TATP Using Thermodynamic Based Gas Sensor with Metal Oxide Catalyst", Y. Chu, K. Waterman, C. Hurley, M. Amani and O.J. Gregory.

2011 DHS Center of Excellence for Explosives Characterization, Mitigation and Detection Review, March 2011, "TATP Detection Using a Thermodynamic Based Gas Sensor", Yun Chu, Kellie Waterman, Matin Amani, Caitlin Hurley, Mike Platek and Otto Gregory, March 2011, Northeastern University, Boston, MA

URI Graduate Symposium –May 2011 Department of Chemical Engineering, Kingston, RI 02881, "Catalyst Discovery Using Combinatorial Chemistry Techniques", K. Warterman, Y. Chu, M. Amani, M. J. Platek and O. J. Gregory

URI Graduate Symposium –May 2011 Department of Chemical Engineering, Kingston, RI 02881, "Detection of TATP Using Thermodynamic Gas Sensors", Y. Chu, K. Waterman, M. Amani, C. Hurley, M. J. Platek and O. J. Gregory

RICC R2R Conference 2011, Northeastern University, Boston, MA, "Thermodynamic Based Sensors for the Detection of Explosives and Explosive Precursors", Otto J. Gregory

URI Patent Disclosure August 2011

"A Thermodynamic Based Gas Sensor for the Detection of TATP", Otto J. Gregory, Michael J. Platek, August Cote III and Matin Amani

References

H. Nanto, T. Minami, and S. Takata, K. J., "ZnO thin film ammonia gas sensors with high sensitivity and excellent selectivity", J. Applid Physics, 60(2), 15 p.482 (1986).

M.S. Wagh, G.H. Jain, D.R. Patil, S.A. Patil, L.A. Patil, "Modified zinc oxide thick film resistors as NH₃ gas sensor", Sensors and Actuators B, 115, p. 128–133, (2006)

M. Aslam, V.A. Chaudhary, I.S. Mulla, S.R. Sainkar, A.B. Mandale, A.A. Belhekar, K. Vijayamohanan), "A highly selective ammonia gas sensor using surface-ruthenated zinc oxide", Sensors and Actuators, 75, p.162-167 (1999)

G.S. Trivikrama Rao 1, D. Tarakarama Rao, "Gas sensitivity of ZnO based thick film sensor to NH₃ at room temperature", Sensors and Actuators B, 55, p.166-169 (1999)

G. Uozumi, M. Miyayama, H. Yanagida, "Fabrication of CuO-infiltrated ZnO composite and its

gas sensing properties”, J. Mater. Sci., 32, (11) 2991–2996 (1997).

E. E. Crisman, J. S. Derov, A. Drehman, O. J. Gregory, “Large Pyroelectric Response from Reactively Sputtered Aluminum Nitride Thin Films”, J. Electrochemical Society, Electrochemical and Solid State Letters, Vol. 8, Issue 3, pp A141-L1, (2005).

“Gas Sensor Apparatus”, August 5, 2008, O.J. Gregory, A.H. Mengel, D.R. Flanders and M.B. Feick, US Patent No.7,408,158

Gas Phase Ion Chemistry
Gary A. Eiceman
Chemistry Dept New Mexico State University
575-646-2146; geiceman@nmsu.edu

Overview

Instruments that are used as trace detectors of explosives at airports worldwide today are based on ion mobility spectrometry (IMS) and these analyzers provide high-speed response (<8 s) to nanogram and sub-nanogram amounts of high explosives. Apart from concerns surrounding the actually step of collecting sample, the performance of these instruments is governed by a combination of gas phase ion-molecule chemistry and characterization of ions for mobility in a drift tube at ambient pressure. Significant deficiencies exist in both the technology and in our understandings of principles. Such deficiencies limit the practice of trace detection with the current generation of analyzers, hinder new and next embodiments of these principles, and limit long-range vision for how these principles might be favorably arranged for new capabilities in explosives detection. The overall objective of this work has been to clarify the central and fundamental issue in ion based methods of explosive determinations, namely, the stability and lifetime of ions of explosives in air at ambient pressure. A second and essential aspect of trace detection concerns sample collection and we wish to explore a new concept in surface sampling which might provide a next generation capability for automated screening of items, some of which may have irregular surfaces.

In Year 1, a refined design to measure the stability of gas phase ions was constructed and demonstrated and shown to provide kinetic information on the decomposition of gas phase ions without the failures of all prior designs where entry of sample neutrals into the kinetic region corrupted measurements.

In Year 2, the gas chemistry of explosives or explosive related materials nitrotoluene (NT), dinitrotoluene (DNT), trinitrotoluene (TNT) and Pentaerythritol tetranitrate (PETN). Of these substances explored using a kinetic IMS, the following behaviors were observed:

- a. negative ions for DNT and TNT undergo decomposition at temperatures as early as 110°C suggesting this that gas phase ions of was more unstable than anticipated. These studies were made using chloride ion chemistry as practiced in current trace detector technologies. There was clearly a temperature dependence below 150°C suggesting first a decomposition of M^+Cl^- to $(\text{M}-\text{H})^-$ and later a loss of $(\text{M}-\text{H})^-$ through a yet unidentified pathway. The initial reaction of M^+Cl^- and then $(\text{M}-\text{H})^-$ appeared to occur at rates faster than 5 to 10 ms at all temperatures. Consequently, the expected elevation of baselines, normally used to derived rate constants in air at ambient pressure with our method, were not observed and ion decomposition kinetics were not measurable. A next step is to seek shorter ion residence times with greater electric fields and smaller dimensions.
- b. negative ion chemistry for NT was comprised of more than few product ions which complicated measurements and confused interpretation. These patterns were attributed to impurities in the sample and not to complex ion chemistries. This and other experiments with substances with comparable complex patterns, suggested that sample pre-fractionation before the kinetic IMS was necessary and in 2011 we added a gas chromatograph as an inlet for the kinetic IMS. Studies with NT, DMNB, EDGN, and NG are underway with the GC-kinetic IMS instrument and will be continued.

Results & Discussion

Ion Kinetic Studies with DNT and TNT

In Figure 1, the results of a temperature study for DNT with the kinetic IMS are shown and the shift in peak area from the product ion (at right between 18 and 24 ms) to reactant ion (at left from 10 to 14 ms). The loss of intensity (or peak area) for the product ions and gain in reactant ion tells of chemistry occurring in the measurements. In this plot, the first ion shutter was active and the second ion shutter (used for kinetic time scales) was inactive or "opened"; thus, the spectra with the flat baseline between the reactant and product ions discloses that the gas phase reactions occurred rapidly in the ion source region, under 10 ms.

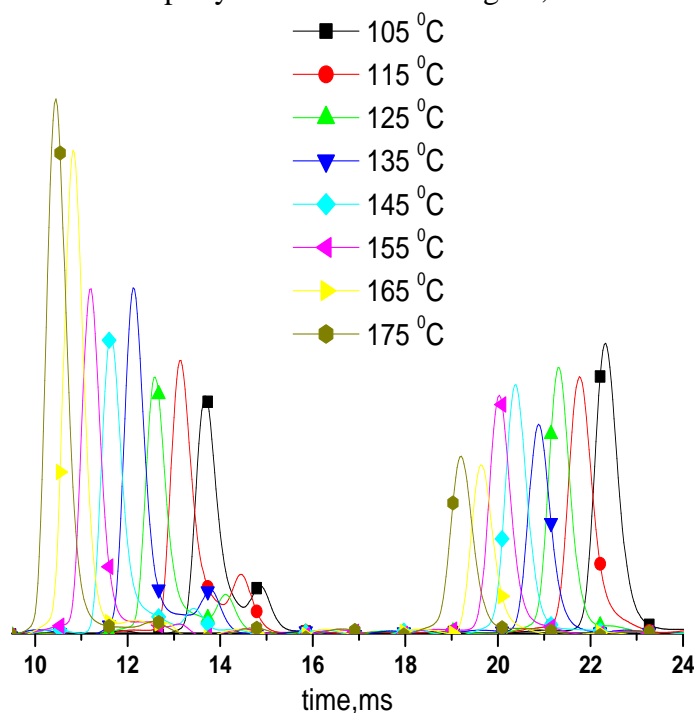


Figure 1. Ion patterns for DNT in mobility spectra, overlaid for all temperatures, using a kinetic IMS at ambient pressure (660 torr) in an air atmosphere. The lack of baseline distortion tells that the reaction chemistry occurred within the reaction region, providing insufficient time to directly observe decomposition and obtain kinetic rate constants.

A comparable conclusion was reached for the behavior of TNT although temperature ranges were higher. Even more interesting, the product ion for TNT was stable up to temperatures of 250°C without serious loss in ion intensity. We will confirm with API MS or IMS MS however the product ion for TNT is well-accepted as (M-1)-. This stability is illustrated for TNT in Figure 2 where a mobility spectrum is shown with symmetric peaks and a flat baseline. These two spectral details indicate stable ions at this temperature (255°C and 16 ms).

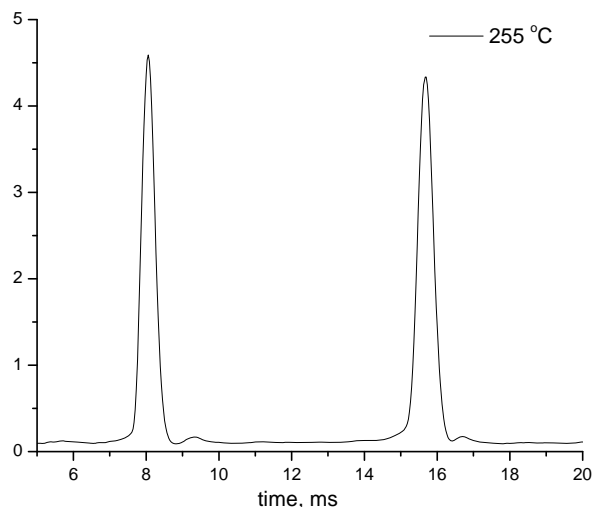


Figure 2. Ion mobility spectrum in kinetic IMS for TNT using a single ion shutter measurement. The reactant ion (Cl^-) is seen at 8 ms & product ion for TNT, at 15.8 ms. The relatively flat baseline & clean symmetry of the peaks tells of stable ion chemistry and no observable ion decomposition.

In Figure 3, the intensity of product ion for TNT, normalized for total ion intensity, is shown versus temperature and illustrates the effect of temperature on ion stability leading to decomposition of TNT, perhaps first as the M^+Cl^- and then as $(\text{M}-\text{H})^-$. Clearly, chemistry is occurring but we are not observing directly the decomposition for yet undiscovered reasons. We plan to attack this using an API MS with temperature regulated ion source region and perhaps IMS MS when our instrument is in suitable condition. Finally, we are considering a rebuild of the kinetic instrument with lower ion residence times.

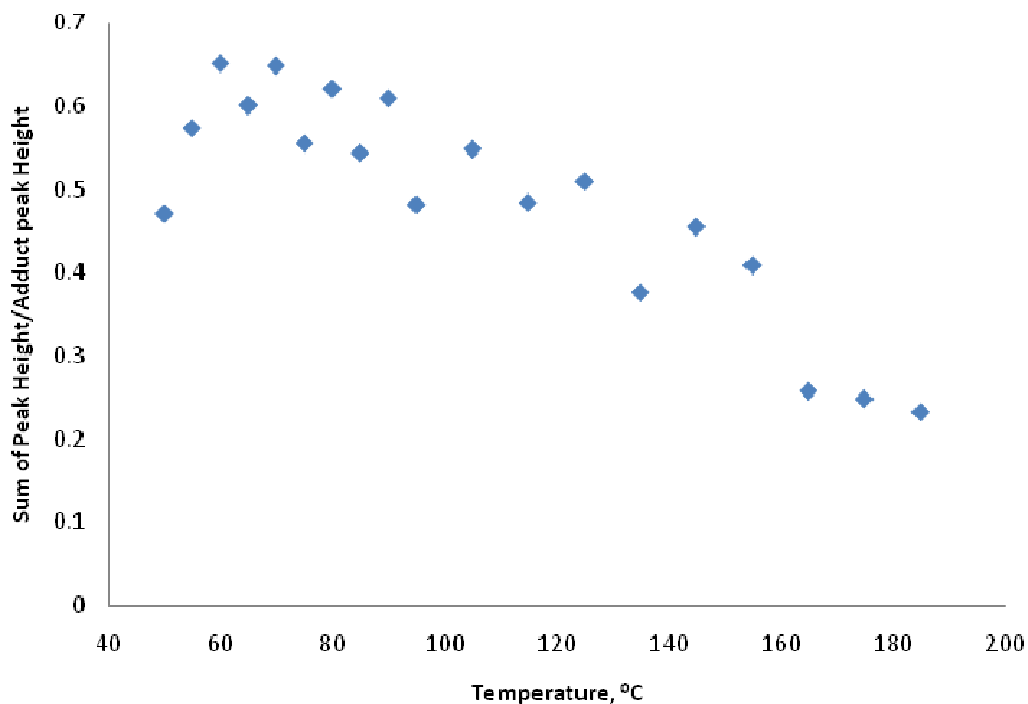


Fig 3. Ion intensity for product ion of TNT versus temperature. The decrease, normalized for all ions shown, suggests puzzling ion chemistries. Kinetics appear to be much faster than previous chloride adduct dissociations studied in this lab.

Studies with PETN

Ion chemistry with PETN is well known as complex and as recently as this year still under study (see Choi, et al, Bull Korean Chem Soc. 2011, 3, 1055-1058). We also have known that PETN when heated undergoes thermal decomposition as fast as vaporization and yet vapors do form and we thought we could isolate the product ion for kinetic studies. As seen in Figure 4, we obtained a spectrum with two nearly identical product ions. While the spectrum in Figure 4 seems promising (sample at 50°C and drift tube at 100°C); increases in temperature of either the drift tube or the sample or both led to highly complex mobility spectra....too complex for use. For this reason, a gas chromatograph has been added to the kinetic IMS (Figure 5) to pre-separate constituents and provide clean or unequivocal mobility response.

PETN-Cl Adduct

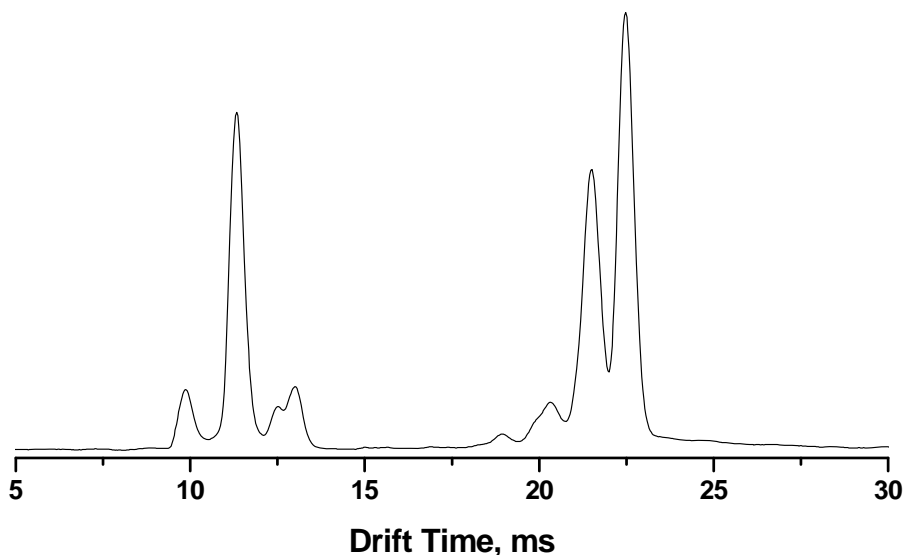


Fig. 4. Mobility spectrum of PETN in kinetic IMS. The product ions for PETN are seen at drift times greater than 20 ms. Chloride reactant ion peak is seen at 11 ms.



Fig. 5. The combination of gas chromatograph with kinetic IMS (inside oven) to obtain rate data free of impurities of sample. This work was started late in summer 2011 and is now in-progress.

Conclusions

Negative gas phase ion chemistry of explosives has exhibited rate constants faster than 10 ms for conversion of adducts to hydrogen abstracted species eluding heretofore direct observation of the reactions with a kinetic IMS. Reactions are seen with absolute peak area methods and we may need to revert to such indirect measures to obtain rate data. However, direct measurements are preferred and reduced residence times will be sought in 2011-2012 and supplemented with API MS studies. Other materials such as PETN have demonstrated our need to pre-fractionate before measurements and a gas chromatograph was added to the kinetic IMS for this purpose.

Both of these experiences demonstrate that the chemistry of negative ions of explosives is elusively and deceptively complex both in ion kinetics and sample handling. We will document and publish with permission findings from these and from NG, EGDN, and DMNB in the next year.

Solution-Based Direct Readout Surface Enhanced Raman Spectroscopy (SERS) Method for Detection of Ultra-Low Levels of Explosives Using Dogbone Shaped Gold Nanoparticles

Dr. Radha Narayanan

Chemistry Dept; University of Rhode Island

Objective

The overall objective of my research is to use nanoparticles of different shapes as colloidal SERS substrates for a direct readout and solution-based detection of ultra-low levels of different explosives.

Summary

We have synthesized dogbone shaped gold nanoparticles of two different sizes. The surface plasmon band of the nanoparticles red-shifts with increasing size of the dogbone shaped gold nanoparticles. We have successfully acquired the SERS spectra for dicyanodiamide and picric acid using the dogbone shaped gold nanoparticles as colloidal SERS substrates. We have also used gold nanoparticles as colloidal SERS substrates for detection of TNT. We have obtained calibration curves for detection of TNT.

Accomplishments

- Successfully synthesized two different sizes of dogbone shaped gold nanoparticles
- Obtained the UV-Visible spectra of the two sizes of dogbone shaped gold nanoparticles
- Acquired the SERS spectra of dicyanodiamide and picric acid using the dogbone shaped gold nanoparticles as colloidal SERS substrates
- Acquired the SERS spectra of TNT.
- Obtained the calibration curves for SERS based detection of ultralow levels of TNT

Details

The dogbone shaped gold nanoparticles is synthesized using the seed-mediated growth method which consists of two steps: preparation of the gold nanoparticle seeds and growth of the seeds in a growth solution. Systematic variation of the concentration of the different components as well as a variety of different synthetic parameters results in gold nanoparticles of different shapes and sizes. We have synthesized two different sizes of dogbone shaped gold nanoparticles. Figure 1 and 2 show the TEM image and size distribution plot for two different sizes of dogbone shaped gold nanoparticles.

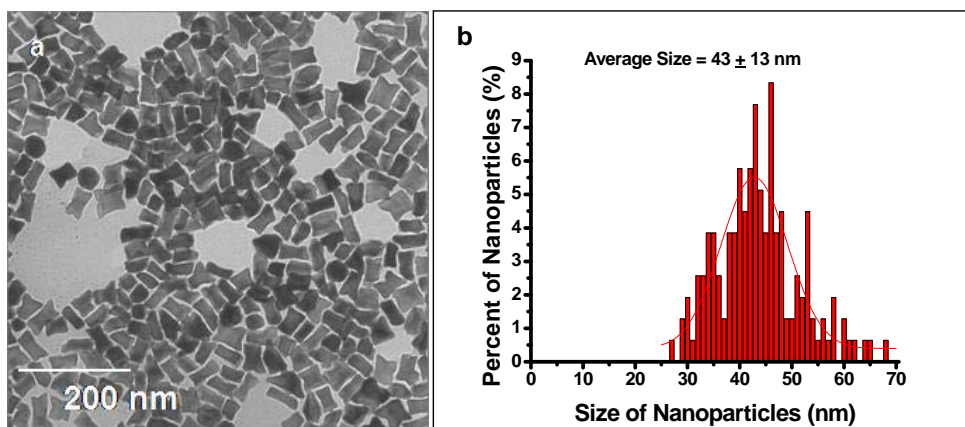


Fig 1. TEM image and size distribution plot of the smaller dogbone shaped gold nanoparticles.

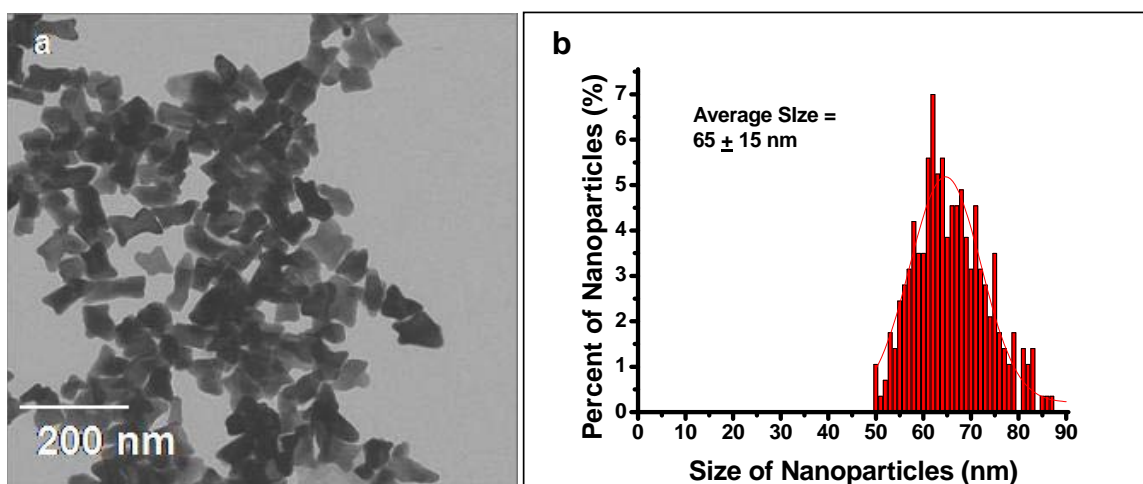
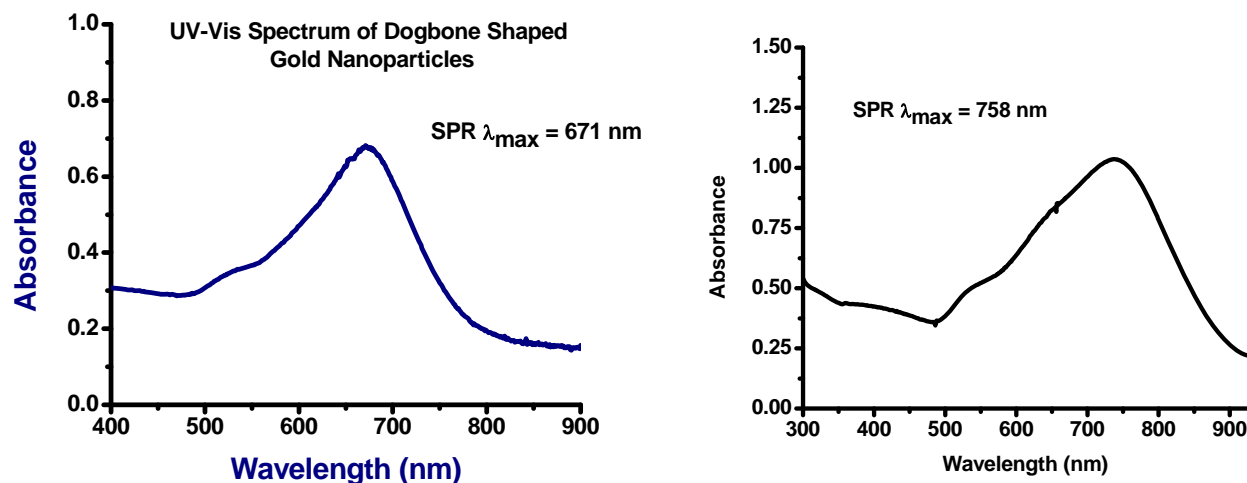


Fig 2. TEM image and size distribution plot of the larger dogbone shaped gold nanoparticles.

We have obtained the UV-Visible spectra of the two different types of dogbone shaped gold nanoparticles. It was observed that the larger dogbone shaped gold nanoparticles result in a higher SPR lambda max which would result in higher SERS enhancements compared to the smaller dogbone shaped gold nanoparticles. Figure 3 and 4 show the UV-Visible spectra of the two types of dogbone shaped gold nanoparticles.



Figs 3 & 4 UV-Visible spectra of small (left) dogbone-shaped & large (right) gold nanoparticles

We have obtained the SERS spectra of different concentrations of dicyanodiamide using the larger dogbone shaped gold nanoparticles. Figure 5 shows the SERS spectra of dicyanodiamide that we have obtained. We have also obtained the SERS spectra of different concentrations of picric acid using the larger dogbone shaped gold nanoparticles. Figure 6 shows the SERS spectra of picric acid that we have obtained.

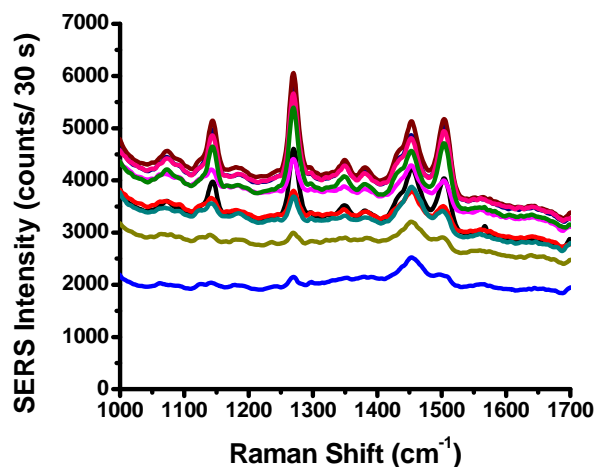


Fig 5. SERS spectra of dicyanodiamide obtained using large dogbone shaped gold nanoparticles

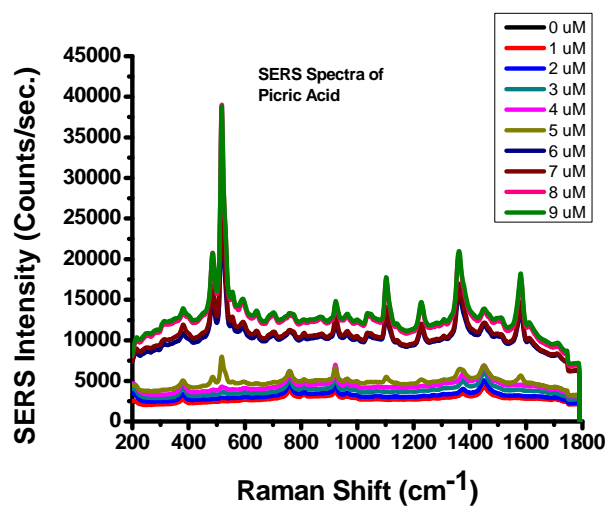


Fig 6. SERS spectra of picric acid obtained using larger dogbone shaped gold nanoparticles

We have also used SERS for detection of TNT. Figure 7 shows the calibration curve for SERS based detection of TNT.

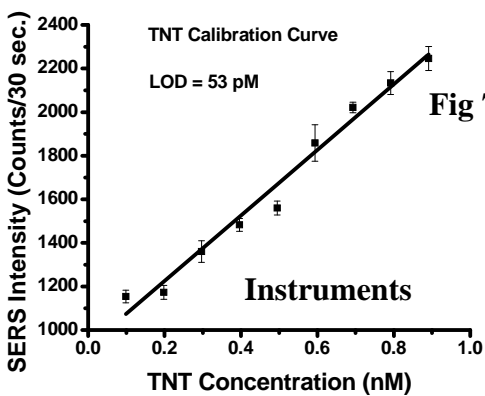


Fig 7. Calibration curve of detection of TNT using SERS



RamanSystems Raman Spectrometer



Agilent UV-Visible Spectrometer



Malvern ZetaSizer Nano



Agilent HPLC

Students Supported



Benjamin Saute (Ph.D. student) Alison Alix (undergraduate) Nicole Cook (undergrad)

Conference and Journal Publications

1. URI Explosives Workshop Poster Session, October 7-9, 2009, Kingston, RI, **Poster**, “Metal Nanoparticles of Different Shapes as Colloidal Substrates for Solution-Based SERS Detection of Environmental Pollutants and Explosives”, Benjamin Saute, Nicole Cook, and Radha Narayanan
2. DHS Center Review, March 24-25, 2011, **Poster**, “Nanotechnology for Detection of Ultralow Levels of Explosives”, Benjamin Saute and Radha Narayanan

Future Plans

We plan to continue to use the dogbone shaped gold nanoparticles as colloidal SERS substrates for detection of dicyanodiamide and picric acid. We will obtain the SERS spectra at different concentrations of dicyanodiamide and picric acid and obtain the calibration curve. The minimum distinguishable signal will be obtained and plugged into the best-fit equation for the calibration curve. This will result in the limit of detection for the two types of explosives.

We will work on synthesizing gold nanoparticles with lambda max as close as possible to 785 nm, which is the laser excitation wavelength. This should result in the highest SERS enhancements and we will harness this for achieving lower limits of detection for dicyanodiamide and picric acid. In addition, we will harness the effect of hot spots and lightning rod effect to achieve even lower limits of detection. We will also harness the effects of greatest contributions of the SERS electromagnetic enhancement effect, hot spots, and lightning rod effect for studies related to detecting ultralow levels of TNT, DNT, NB, and TATP. We will compare the SERS limits of detection obtained previously with TNT to those obtained using gold nanoparticles that harness the highest amount of electromagnetic enhancement effect, hot spots, and lightning rod effect. We will also obtain the limits of detection that can be achieved for DNT, NB, and TATP.

We will use a chemisorption scheme of secondary amines bound to CS₂ anchoring units on gold nanoparticle surfaces to increase the SERS response when compared to those assembled on planar surfaces. Furthermore, several explosive materials including methylnitroguanidine and dicyandiamide contain secondary amine functionalities, which makes them ideal candidates for detection by dithiocarbamate/ gold-nanoparticle assembly. We will obtain the SERS spectra and limits of detection of dicyanoamide and methylnitroguanidine bound to the CS₂ anchoring units on the gold nanoparticles.

Shaped Femtosecond Pulses for Remote Chemical Detection

Yaron Silberberg

Weizmann Institute of Science

I. Objective

Our goal is to develop nonlinear spectroscopic methods for the remote detection of hazardous materials in general and explosives in particular, using the vibrational spectrum of molecules as a fingerprint for chemical species identification. The main approach we have been taking employs carefully tailored ultrashort laser pulses for Stimulated Raman Scattering (SRS) and Coherent Anti-stokes Raman Spectroscopy (CARS).

II. Accomplishments

- a) We have demonstrated a “Shaper-less” standoff remote detection from distance of up to 50 meters, using femtosecond pulses shaped by a photonic crystal filter [4], thereby surpassing the current record detection distance with a far simpler, cheaper, and attractive experimental technique.
- b) We have investigated for the first time SRS as a standoff detection scheme. We have shown that SRS can be used for standoff detection, yet we have not been convinced that it offer significant advantages over the various CARS techniques.

III. Details

Shaperless CARS technique. Prior to joining this project, our group has successfully demonstrated several pulse-shaping techniques [1] allowing remote detection and identification of minute amounts of chemicals at standoff (>10m) distances, using a single laser source and a single-beam of shaped femtosecond pulses [2-4]. In our single-beam techniques, a single broadband femtosecond laser pulse supplies both the 'pump', 'Stokes' and 'probe' photons simultaneously [5,6]. Through careful spectral-phase shaping using a pulse shaping apparatus (See Fig. 1c) a narrowband probe is selected within the pulse wide spectrum, and a spectroscopic resolution more than 30 times better than the pulse bandwidth is obtained, allowing for species identification. Using this technique we have succeeded in rapidly resolving the vibrational spectrum of trace amounts of contaminants, such as explosives and nitrate samples, from the weak *backscattered* photons under ambient light conditions, from a distance of 12 meters [2-3] (Fig.1).

One of the drawbacks of this approach is the need for an expensive and complex pulse shaping apparatus, and our first goal was to develop schemes that could be simpler to use. Indeed, in a recent work [4], we have presented a novel scheme for performing single-beam, single-pulse CARS spectroscopy without the need of a 4-f pulse-shaper apparatus, considerably simplifying the experimental setup. We have utilized a resonant photonic crystal slab (RPCS) filter, as a miniature, robust, and tunable pulse shaping element (Fig.2), and demonstrated high resolution vibrational spectroscopy and microscopy. We have recently tested this method in standoff detection geometry, and were able to extend our previous distant records significantly.

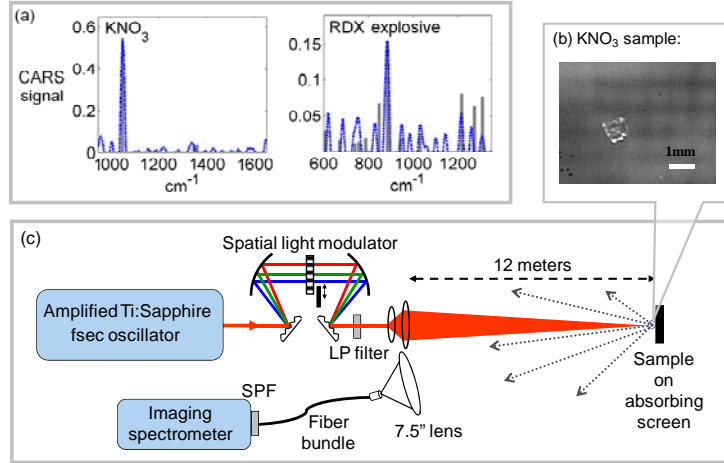


Fig. 1: (a) Resolved femtosecond CARS vibrational spectra for two trace samples obtained at a standoff distance of 12m: $<1000\mu\text{g}$ crystallized KNO_3 particle, and RDX explosive particles with a total mass of $<4\text{mg}$; Each spectrum was resolved from a single measurement with an integration time of <3 seconds. The known vibrational lines of the samples are plotted in gray bars for comparison. (b) Image of the KNO_3 contaminant sample, placed 12m from the measuring system. (c) The experimental setup. The laser source is an amplified femtosecond Ti:Sapphire laser (0.5mJ, 30fs, 1KHz repetition rate). The pulses are phase-shaped in a pulse shaper using an electronically controlled liquid-crystal spatial light modulator. The beam is focused on a distant sample through a telescope, and the backscattered radiation is collected to a spectrometer with a 7.5" diameter lens.

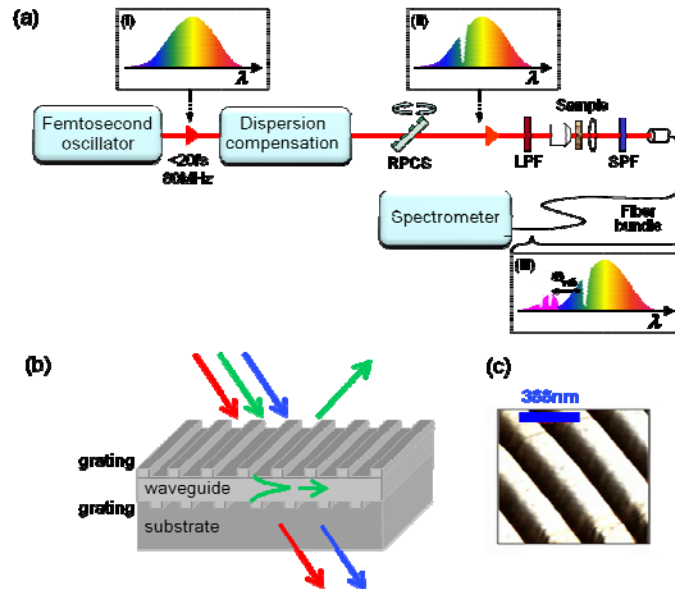


Fig. 2: (a) Schematic description of the experimental setup for single-pulse shaperless CARS using a resonant photonic crystal slab (RPCS): The wideband excitation pulse (i), is shaped with a tunable narrowband notch feature by the RPCS filter (ii). The narrowband notch serves as a probe for the CARS process, generating narrow well-defined features in the CARS spectrum, which are blue-shifted from the probe

by the sample vibrational frequencies (iii). (LPF - long-pass filter, SPF - short-pass filter); (b) A schematic diagram of the RPCS double grating waveguide structure; For a given beam incident angle total reflection occurs for the resonant wavelength and a tunable narrow dip in the transmission spectrum is obtained. (c) Atomic force microscopy measurements of the RPCS surface sub-wavelength grating.

The beam from an amplified femtosecond laser was filtered by the RPCS, expanded by a telescope and sent to distances of up to 50 m to illuminate a target, which was composed of powder spread over scattering background. The backscattered radiation was collected by a second telescope and the spectrum was measured. To extract the CARS spectra, the process was repeated for two slightly different angles of the RPCS filter, which lead to slightly shifted CARS spectra, enabling subtraction of background and laser spectral noise. The results are shown in Fig. 3.

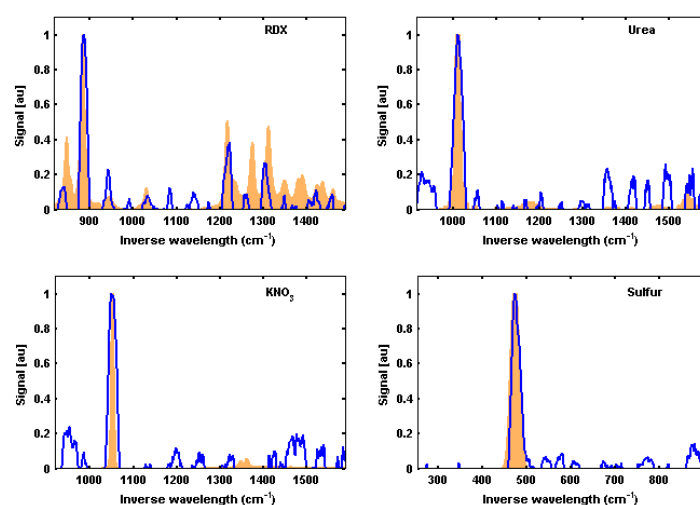


Fig 3. Standoff spectra of various powders. RDX was measured at 5m, Urea, potassium nitrate and sulfur were measured at arecord 50m. Blue lines are extracted spectra, orange shows the main vibrational lines of the various target materials.

SRS vs. CARS for standoff detection.

In recent years there has been a debate on the relative advantages and disadvantages of CARS spectroscopy vs. SRS. While the physical processes are identical, each method offer certain advantages that may be important depending on the specifics of the system involved. We have recently reported a study of SRS using a single shaped femtosecond pulse, or SPSRS [7]. We subsequently tested the suitability of this method for standoff detection. Figure 4 shows some results of SRS measurements on sulfur powder. While it was easy to identify the main sulfur vibration lines at short distances, it was impossible to do so at a distance of 5m. The main difficulty arises from the fact that in SRS the signals appear as an increase or decrease of the excitation light, and this seems to be much more difficult to identify and to separate from other processes that affect laser propagation (this in comparison with CARS spectra that appear in different spectral regions).

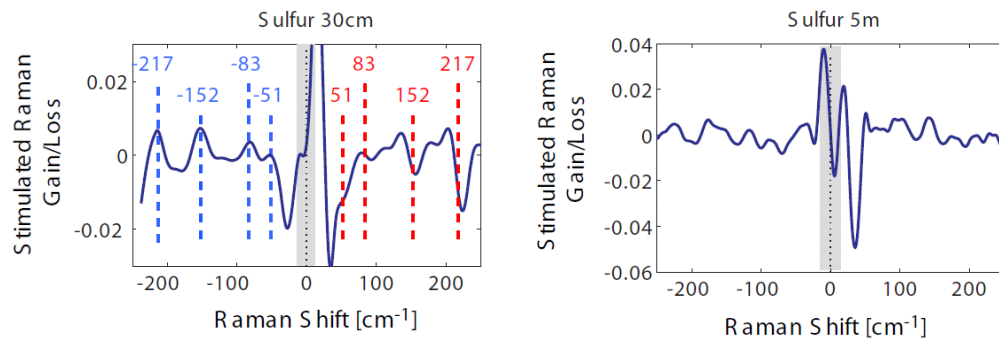


Fig. 4. Single-pulse Stimulated Raman Scattering (SPSRS) of sulfur at standoff distances. While identification was simple at short range, distances of a few meters did not enable detection. Red and blue lines identify vibrational transitions that appear as peaks or dips in the scattered light.

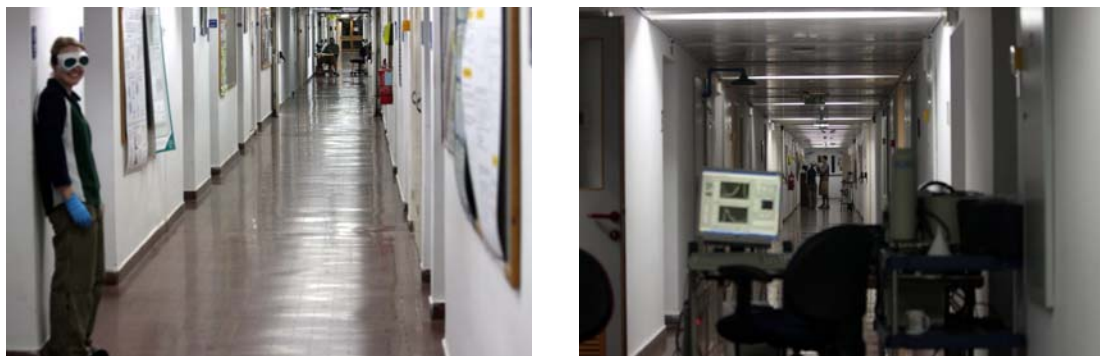


Fig. 5. Performing standoff detection experiments at distances significantly larger than 10 meters. require some improvisation and special precautions. Experiments at 50 meters were conducted at late hours, in a long corridor that was cordoned off for the duration of the experiment.

IV. Students Involved:

Ori Katz, PhD Student.

Ady Natan: PhD. student, Graduated in 2010.

Hadas Frostig: MsC student, Graduated 2011, continues for PhD.

Jonathan Levitt, Postdoctoral trainee.

V. References

- [1] Yaron Silberberg "Quantum Coherent Control for Nonlinear Spectroscopy and Microscopy" , Annu. Rev. Phys. Chem. 2009.60 (2009)
- [2] O. Katz, A. Natan, S. Rosenwaks, Y. Silberberg, "Standoff detection of trace amounts of solids by nonlinear Raman spectroscopy using shaped femtosecond pulses", Appl. Phys. Lett. 92, 171116 (2008);
- [3] O. Katz, A. Natan, S. Rosenwaks, and Y. Silberberg, "Shaped Femtosecond Pulses for Remote Chemical Detection," Optics & Photonics News 19, 47-47 (2008)
- [4] O. Katz, J. M. Levitt, E. Grinvald, and Y. Silberberg, "Single-beam coherent Raman spectroscopy and microscopy via spectral notch shaping", *Optics Express*, 18, pp. 22693-22701 (2010).
- [5] N. Dudovich, D. Oron, and Y. Silberberg, "Single-pulse Coherently Controlled Nonlinear Raman Spectroscopy and Microscopy", *Nature* 418, 512 (2002).
- [6] D. Oron, N. Dudovich, and Y. Silberberg, "Single-Pulse Phase-Contrast Nonlinear Raman Spectroscopy" *Phys. Rev. Lett.* 89, 273001 (2002)
- [7] H. Frostig, O. Katz, A. Natan and Y. Silberberg, "Single-pulse stimulated Raman scattering spectroscopy", *Opt. Lett.* 36, 1248-1250, (2011)

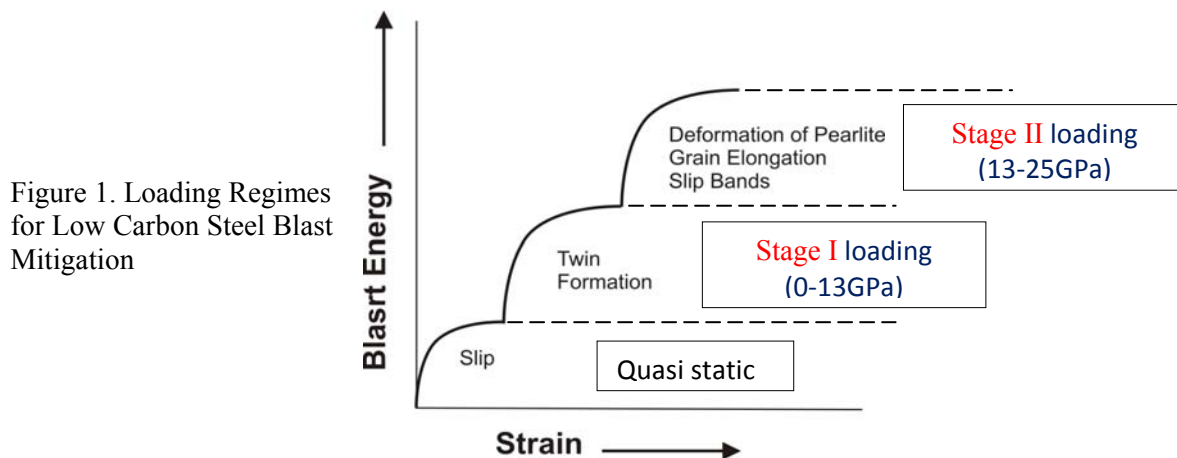
Damage Criterion and Residual Life of Structural Steel Subjected to Blast Loading

Hamouda Ghonem
Mechanical Engineering; University of Rhode Island
ghonem@egr.uri.edu

Objectives

The research in the Mechanics of Materials Research Laboratory in relation to the mitigation group of the explosion research center focuses on the response of low carbon steel (LCS), the primary reinforcing phase material in almost all critical civil structures in the USA, under blast loading in both room temperature and high temperature (fire) conditions. The goal of this work is two folds. The first is to develop an understanding of the deformation and failure mechanisms occurring at high strain rates in LCS, and the second goal is to examine material oriented methods to improve upon the mechanical behavior and response during and after the blast events.

The work completed incorporates both quasi-static and dynamic loading conditions, from which material constitutive properties and analytical material models have been developed. The three different regimes of loading conditions are graphically illustrated in Figure 1. These regimes are categorized both by pressure and by material related deformation mechanism.



The quasi-static testing has been carried out at varying strain rates (10^{-7} – 10^{-4} s $^{-1}$) and varying temperatures (30°C – 800°C) and provides a baseline of data for the material from which material constants are derived. Dynamic loading is divided into two stages; stage I and stage II. The first stage, which is governed by one deformation mechanism, is limited by the pressure amplitude at which the crystal structure of the carbon steel is altered. This stage is a representation of the far field blast shown in the pressure vs distance plot in Figure 2a. Stage II corresponds to blast conditions at which phase transformation takes place and is limited by maximum blast pressures of conventional TNT, see Figure 2a. As shown in Figure 2b, the pressure profile of an explosive blast, or ideal pressure pulse, can be replicated in a laboratory environment from planar plate impacts using a gas gun. This approach, using a gas gun to simulate blast loading, has the advantage of being infinitely repeatable for both moderate and severe loading conditions, and the incorporation of a heating unit in the gas gun design provides the ability to simulate a high temperature fire environment accompanying a blast. The work in 2010 has focused on stage I, moderate blast condition at room temperature. This work has been extended to the design and construction of a high pressure gas gun. This unique system is employed in the current research to identify the residual life associated with severe blast loading (stage II) of carbon steel.

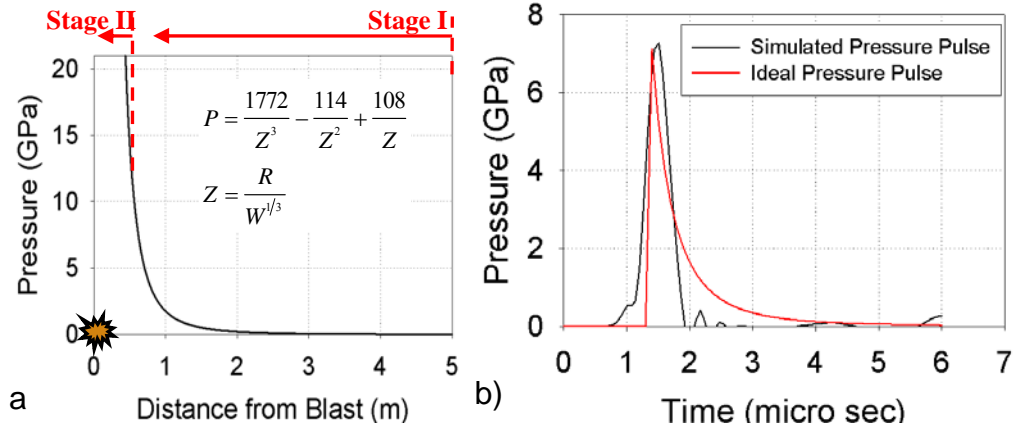


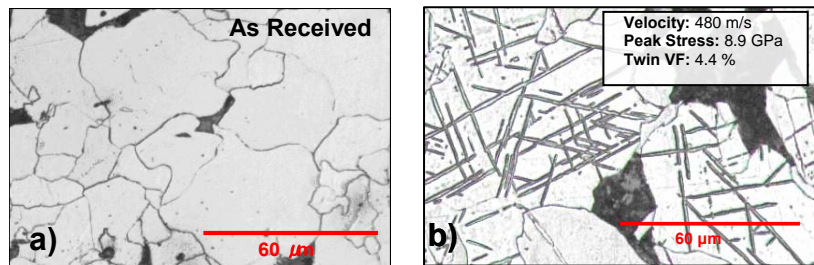
Figure 2. a.) Pressure vs. distance for a conventional TNT explosion, and b.) an ideal explosive pressure pulse and a simulated plate impact pressure pulse.

Summary of Completed Research: **Damage Criterion and Residual Life (Stage I Blast Loading)**

The objective of the study is to determine the relationship between high rate impacts and microstructure variation of low carbon steel. Five plate impact experiments were carried out and post impact microscopy shows deformation mechanisms occurring during shock loading of low carbon b.c.c. steel. The coupling of numerical simulations and the analytical constitutive model act as a tool for defining impact history and predicting post-impact microstructure. Results of this study can be briefly summarized as follows:

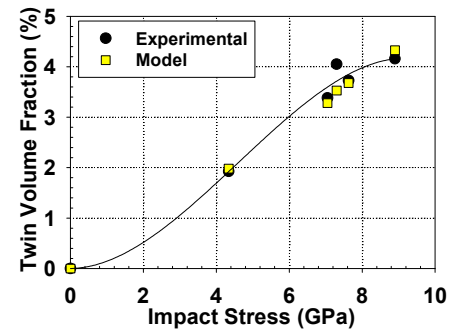
- 1- Microscopic observation of impact specimens indicate that slip and mechanical twinning are two competing deformation mechanisms occurring during high rate loading of low carbon steel. The lenticular shape of the twins, Figure 3b, indicates that the twin formation mechanism is by progressive shear of the parent lattice.

Figure 3. Example of optical micrographs steel specimens a.) as- received, b.) 8.9 GPa peak stress yielding 4.4% twins. Lighter grains are α -ferrite, and darker grains are pearlite, black arrows indicate deformation twins



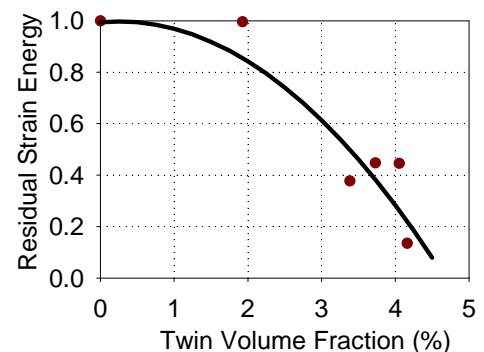
- 2- A direct and unique relationship between impact stress and volume fraction of twins has been experimentally established as illustrated in Fig. 4. Based on microscopic observations, an analytical twinning model aiming at predicting twin volume fraction incorporating both slip and twinning mechanisms has been applied and shown to accurately calculate twin volume fraction, Figure 4. This model was coupled with a rate dependent model implemented into numerical procedures and was capable of capturing deformation response and twin formation during impacts for the given stress range.

Figure 4. Comparison of experimentally measured and analytically computed twin volume fraction within α -ferrite grains as a function of impact stress



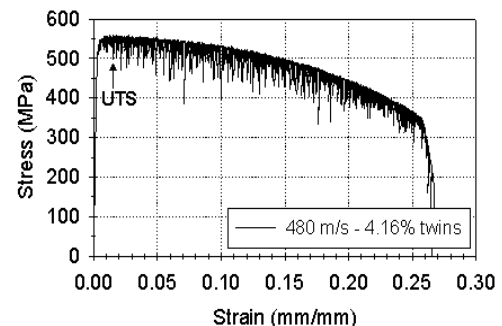
- 3- Quantitative analysis of the post-impact stress-strain curves clearly shows an increase in both yield and ultimate strength which indicates an increase in stored dislocations in the microstructure as a result of impact loading, however the available strain energy, Figure 5, is drastically reduced; up to 87%. If this trend is extrapolated further, it will show that the yield and ultimate tensile strength converge, thus eliminating available energy.

Figure 5. a.) Ultimate tensile strength and yield stress of post-impact tensile specimens as a function of twin volume fraction, b.) Residual strain energy ratio versus twin volume fraction. The ratio is in reference to the as-received condition with no twins. Strain energy is measured as area under the curve up to strain at UTS.



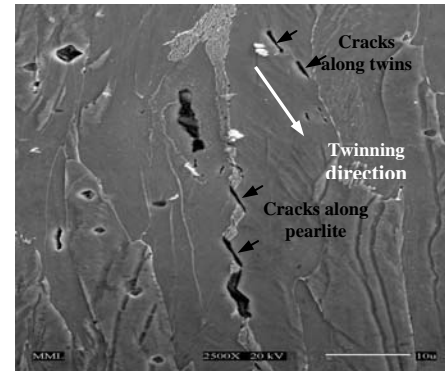
- 4- It is apparent that as the shock loading is increased, new twinning planes are activated. Qualitative analysis provides insight into the dislocation-twinning interaction during plastic deformation. At higher impact levels, the presence of multiple twinning planes and twin-twin interactions results in the transition of type-B serrations to type-C load drops during plastic deformation; Figure 6. This suggests that twin-twin interactions play a significant role in controlling plastic deformation which is responsible for instability within the microstructure.

Figure 6. Post-impact stress strain curve for steel which has been impacted prior to quasi-static tensile testing to 8.9 Gpa



- 5- The twins play an important role in the direction of cracking during failure. They provide new interfaces at which cracks may initiate and propagate, and also control the direction of crack propagation, as shown in Figure 7.

Figure 7. SEM micrograph of necked region in post-impact tensile specimen. Cracking occurred along the ferrite-pearlite and twinning interfaces during post-impact tensile testing



Summary of Current Research (2011-2012)

Residual life Due to Extreme and Repeated Blast/Thermal Loadings of Critical Civil Structures

In order to fully explore the process and effects of blast loading on low carbon structural steel, higher impact pressures and rates are required beyond the capacity of previous facilities. Development and construction of a high pressure light gas gun has commenced and has been completed during the past semester. Furthermore, two major projects have started using the capabilities of the gas gun system coupled with analytical and numerical tools established in the first phase of this program, described above. These are related to effects of pre-straining on impact loading, and impact induced phase transformation and failure in structural steel under combined blast/thermal loading. Components of the current phase of research are summarized below.

I- Design and Construction of High Pressure/High Temperature Gas Gun

A gas gun system has been designed and fully assembled, see Fig. 8. Utilizing a quick release system similar to that of a shock tube, the new system can safely carry up to 5,000 psi of compressed light gas (helium). A double rupture disc setup is utilized in order to provide a consistent and controllable release of pressure to the projectile. The projectile velocity is a function of both input pressure and the weight of the projectile. Maximum launch velocities are projected to be over 2,000 m/s and generate an impact stress greater than 30 GPa in order to simulate TNT impact loading. The new system will provide a means of achieving stress and strain rates above the saturation limit of twinning, and extend into regimes of phase transformation.

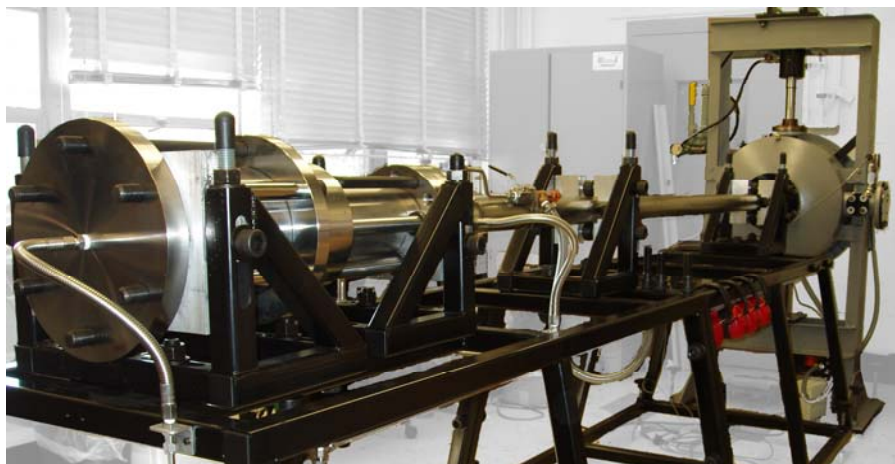


Figure 8. Fully assembled gas gun system.

II-Impact Induced Phase Transformation and Failure

The second part of our blast mitigation focuses on the high impact region in which global phase transformation occurs. This is the process by which a material under impact loading will completely revert to a closer packed, higher density structures. The objective of this work is to examine the microstructure variation and the relation to exhausted material strength, and determine the critical strain rate and stress level at which this transformation takes place. A constitutive model is currently being developed which calculates the phase transformation as a function of time and distance within the impacted disc. Based upon the basic conservation equations, strain and particle velocity are incrementally calculated as a function of pressure, shear stress, and temperature. A criterion for spall fracture due to phase transformation is also developed based upon volume fraction of transformed material and impact stress. The significance of this work to explosion research is that due to phase transformation, areas of high tensile stress can cause tensile spall fracture and ultimately lead to premature failure of steel members and consequently the structure.

III-Effects of Pre-straining on Impact Loading

Preliminary study of moderate blast loading of low carbon steel has been examined. The impact process has been experimentally carried out and numerically analyzed. A correlation has been made between impact parameters and material variation. These properties have then been quantitatively and qualitatively studied during post-impact mechanical testing. From this study it has been shown that moderate shock loading results in microstructure variations which are ultimately detrimental to post-impact residual strength. The variations, namely deformation twins, are occurring due to stress concentrations initiating from localized regions of high stress and strain rate.

The objective of this work aims at improving the material's post-impact strength. In order to improve the response, it is required that the material deforms homogeneously during the shock loading process. Previous studies have shown that the presence of dislocations within the substructure of the material prior to impact loading will lead to a reduction, or complete suppression of twins. As shown in the Stage I loading cases, the only mechanism responsible for altering the post-impact properties is the presence of deformation twins, therefore reduction in twin volume fraction will lead to an increase in overall stability. By rolling specimens in the radial directions, 2 and 3, perpendicular to the impact direction, the material remains axis-symmetric; Figure 9a. Furthermore, the amount of pre-straining is related to the amount of twins suppressed. This is related to the amount of mobile dislocations which accommodate or replace the twinning process, rather than the overall dislocation density.

The microstructure of the rolled material can be seen in Figure 9b and 9c, where it shows that a large number of dislocation colonies have been created during the rolling process.

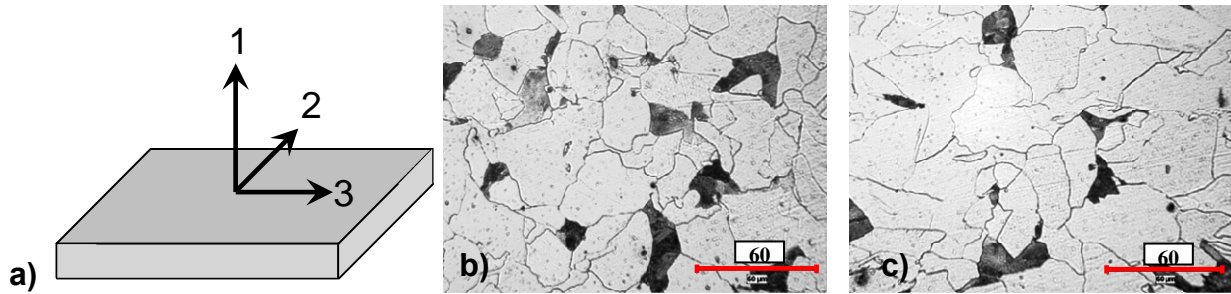


Figure 9. a.) Specimen Orientation and micrographs of b.) 2-3 plane of rolled material, and c.) 1-2 plane of rolled material.

By varying the amount of pre-strain on the specimens, 0-20%, the amount of mobile dislocations is increased. The mobility of existing dislocations will affect the nucleation of twins by reducing the number of twins required to complement slip at a given strain rate. As a result of eliminating twins, post-impact microstructure will remain stable for moderate shock loading case of as-received material. Also, the reduction in twins will prevent the grains from reorientation to a preferential direction for adiabatic shear bands which generally leads to premature failure.

Significance of Current Program to DHS Blast Mitigation Research

The overall goal of both the phase transformation study and the pre-straining study is to first understand the deformation process during impact in both Stage I and Stage II blast loading conditions. Second, once these processes have been examined and a thorough understanding is realized, this information can be used to characterize and alter the material in a way which improves both its blast performance and its post-impact residual strength.

1. Characterization of both stages of blast loading in relation to deformation mechanisms enables a direct assessment of existing structures subjected to explosive loading and provides information about the explosion; i.e. stand-off distance, maximum blast pressure, and pressure profile.
2. Characterization of both stages of blast loading in relation to deformation mechanisms enables upper loading limits for the use of the material.
3. The upper strength limits under blast loading conditions can be determined using laboratory controlled methods; gas gun facility.
4. Controlling the mechanisms governing explosive deformation will enhance the blast resistance of the steel and improve the ability to withstand further loads after the blast event.
5. Recommendations can be made to steel manufacturers on the steel forming process in order to increase blast resistance while still retaining the same composition, and effectively the same cost.

Publications and Presentations

The research group has participated in two conferences and submitted three journal papers::

- W. Visser, G. Plume, C-E. Rousseau, H. Ghonem. "Deformation Criterion of Low Carbon Steel Subjected to High Speed Impacts", *IMPLAST 2010 Conference Proceedings, Providence RI, October 2010.*

- W. Visser, Y. Sun, H. Ghonem. “Twin Influence on Post-Impact Deformation Characteristics of Low Carbon Steel”, IMPLAST 2011, *Mohegan Sun, CT. 2011.*
- K. Maciejewski, Y. Sun, O. Gregory and H. Ghonem, Time-Dependent Deformation of Low Carbon Steel at Elevated Temperatures, Submitted to *Materials Science and Engineering*, March 2011
- Y. Sun, K. Maciejewski, and H. Ghonem, Simulation of Viscoplastic Deformation of Low Carbon Steel Structures at Elevated Temperatures, *Journal of Materials Engineering and Performance*, DOI 10.1007/s11665-011-0023-0, August 2011
- W. Visser, Y. Sun, G. Plume, C.E. Rousseau, O. Gregory, H. Ghonem. “Deformation Characteristics of Low Carbon Steel Subjected to Dynamic Impact Loading”, *Materials Science and Engineering A.*, Volume 528, Issue 27, , Pages 7857-7866, October 2011.

Development of Novel Composite Materials & Structures for Blast Mitigation

Arun Shukla

Department of Mechanical, Industrial and Systems Engineering
University of Rhode Island, Kingston, RI 02881

Objective

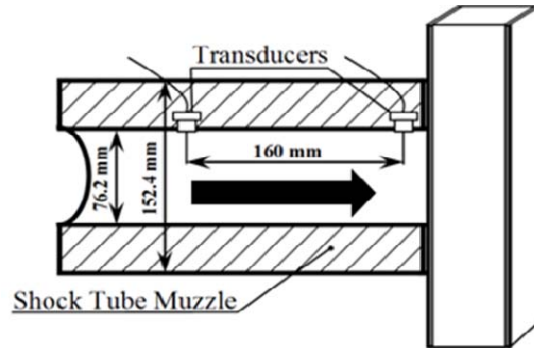
The present study aims at developing novel materials and structural configurations that could be effectively used for blast mitigation. The study also focuses on the effect of curvature in structural material to blast loading.

Summary

A shock tube apparatus was utilized to generate a controlled shock loading on the specimens (Fig. 1a). It has an overall length of 8 m, consisting of a driver, driven and muzzle section. The high-pressure driver section and the low pressure driven section are separated by a diaphragm. By pressurizing the high-pressure section, a pressure difference across the diaphragm is created. When this difference reaches a critical value, the diaphragm ruptures. This rapid release of gas creates a shock wave, which travels down the tube to impart a dynamic loading on the specimen. The driver gas is helium and the driven gas is ambient air.



(a) Shock tube



(b) Detail dimensions of the muzzle

Figure 1: Shock tube apparatus

Figure 1b shows the detailed dimensions of the muzzle and locations of the specimen and the pressure sensors (PCB102A). The sensors are mounted at the end of the muzzle section to measure the incident pressure and the reflected pressure during the experiment. The final muzzle diameter is 0.0762 m (3 in). The distance between the two sensors is 0.16m and the distance between the second sensor and the end of the muzzle is ~0.02m. The specimen was placed in the supports and positioned close to the end of the muzzle. These support fixtures ensure clamped boundary conditions with a span of 0.2032 m (8 in) by 0.2032 m (8 in). Fig. 2 gives a typical pressure profile.

The Digital Image Correlation (DIC) technique was also used to measure the full-field, in-plane and out-of-plane displacements. The DIC arrangement is shown in Fig. 3. Initially the camera records an image of the specimen in its un-deformed state. A second picture is then taken after the specimen has deformed. The two images are then compared in order to calculate the in-plane and out-of-plane displacements of the specimen. A random speckle pattern is applied on the specimen and each speckle is individually tracked in order to obtain the in-plane and out-of-plane displacements.

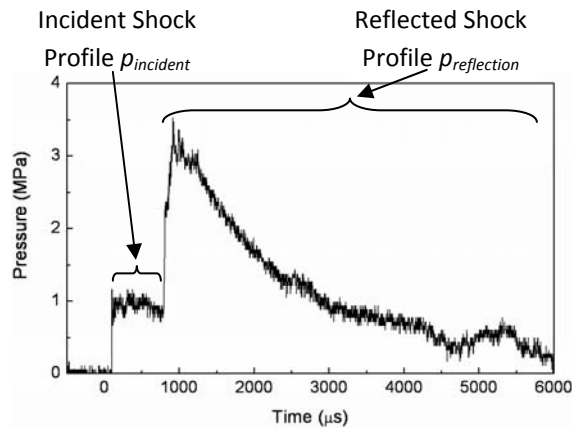


Figure 2: Typical experimental pressure profile

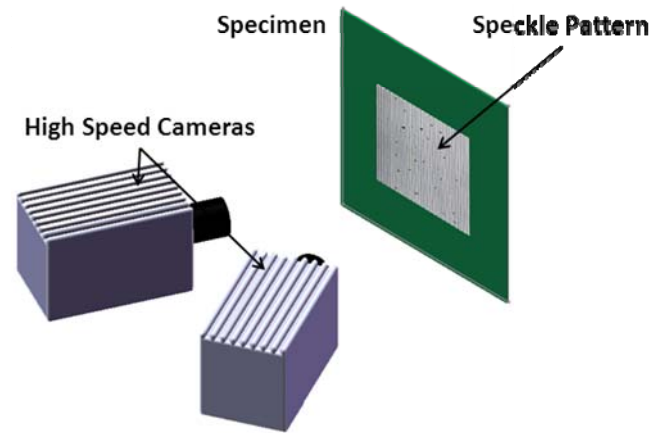


Figure 3: Schematics of the back face DIC analysis

Accomplishments

Task 1. Dynamic response of glass panels subjected to shock loading

A controlled study has been performed to understand fracture and damage in glass panels subjected to air blast. A shock tube apparatus has been utilized to obtain the controlled blast loading. Five different panels, namely plain glass, sandwiched glass, wired glass, tempered glass and sandwiched glass with film on both the faces are used in the experiments. Fully clamped boundary conditions are applied to replicate the actual loading conditions in windows. Real-time measurements of the pressure pulses affecting the panels are recorded. A post-mortem study of the specimens was also performed to evaluate the effectiveness of the materials to withstand these shock loads. The real time full-field in-plane strain and out-of-plane deformation data on the back face of the glass panel is obtained using 3D Digital Image Correlation (DIC) technique. The experimental results show that the sandwich glass with two layers of glass joined with a polyvinyl butyral (PVB) interlayer and protective film on both the front and back faces maintains structural integrity and outperforms the other four types of glass tested.

Task 2. Effect of plate curvature on blast response of aluminum panels

Experimental and numerical studies were conducted to understand the effect of plate curvature on blast response of aluminum panels. A shock tube apparatus was utilized to impart controlled shock loading to aluminum 2024-T3 panels having three different radii of curvatures: infinity (panel A), 304.8 mm (panel B), and 111.76 mm (panel C). Panels with dimensions of 203.2 mm x 203.2 mm x 2 mm were held with mixed boundary conditions before applying the shock loading. A 3D Digital Image Correlation (DIC) technique coupled with high speed photography was used to obtain out-of-plane deflection and velocity, as well as in-plane strain on the back face of the panels. Macroscopic postmortem analysis was performed to compare the yielding and plastic deformation in the three panels. The results showed that panel C had the least plastic deformation and yielding as compared to the other panels. A dynamic computational simulation that incorporates the fluid-structure interaction was also conducted to evaluate the panel response. The computational study utilized the Dynamic System Mechanics Analysis Simulation (DYSMAS) software. The model consisted of the shock tube wall, the aluminum plate, and the air (both internal and external) to the tube walls. The numerical results were compared to the experimental data. The comparison between the experimental results and the numerical simulation showed a high level of correlation using the Russell error measure.

Task 3. Blast response of 32-layered curved carbon fiber panels

Experimental study is underway to understand the effect of plate curvature on blast response of 32-layered carbon fiber panels. A shock tube apparatus has been utilized to impart controlled shock loading to carbon fiber panels having three different radii of curvatures: infinity, 304.8 mm, and 111.76 mm. The panels have a dimensions of 203.2 mm x 203.2 mm x 2 mm are held with fixed boundary conditions before applying the shock loading. A 3D Digital Image Correlation (DIC) technique coupled with high speed photography has been used to obtain out-of-plane deflection and velocity, as well as in-plane strain on the back face of the panels. Macroscopic postmortem analysis is being performed to understand the effect of curvature to blast loading.

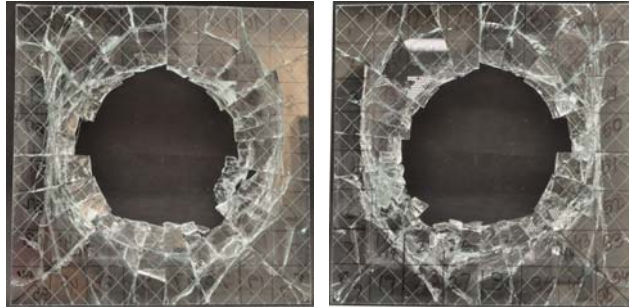


Figure 4: Post-mortem image of wired glass panel

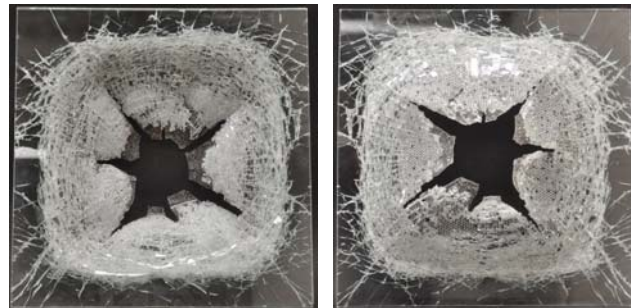


Figure 5: Post-mortem image of sandwich glass panel

Details

Task 1. Dynamic response of glass panels subjected to shock loading

A controlled study has been performed to understand fracture and damage in glass panels subjected to air blast. A shock tube apparatus has been utilized to obtain the controlled blast loading. Five different panels, namely plain glass, sandwiched glass, wired glass, tempered glass and sandwiched glass with film on both the faces are used in the experiments. Fully clamped boundary conditions are applied to replicate the actual loading conditions in windows. Real-time measurements of the pressure pulses affecting the panels are recorded. A post-mortem study of the specimens was also performed to evaluate the effectiveness of the materials to withstand these shock loads. The real time full-field in-plane strain and out-of-plane deformation data on the back face of the glass panel is obtained using 3D Digital Image Correlation (DIC) technique. The experimental results show that the sandwich glass with two layers of glass joined with a polyvinyl butyral (PVB) interlayer and protective film on both the front and back faces maintains structural integrity and outperforms the other four types of glass tested.

Material details

The five different panels used during these experiments include a clear glass panel, tempered glass panel, wired glass panel, sandwiched glass panel and laminated sandwiched glass panel with a protective film on both of its faces. Each experiment is repeated three times. The specimens are 305 mm long x 305 mm wide x 6.5 mm thick. Laminated sandwiched glass panel has a thickness of 7.5 mm because of the protective film on both front and back face of the sandwiched panel.

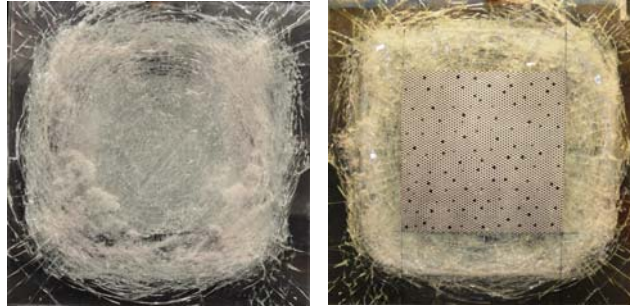


Figure 6: Post-mortem image of laminated sandwich glass panel

Macroscopic post-mortem analysis

The result of post-mortem evaluation of the shock loaded glass panels is shown in Fig. 4-6. The post-mortem analysis of the clear glass and tempered glass panels have not been shown as they completely lost their structural integrity and shattered into pieces. The post-mortem analysis of a wired glass panel is shown in fig. 4. The panel shows a large amount of fragmentation but in comparison to the clear and tempered glass panel, which shattered completely, it retained structural integrity. The post-mortem image of the sandwiched glass panel is shown in fig. 5. There is heavy fragmentation on both the front and back face as seen in figs. 5(a)-5(b). The PVB interlayer is able to withhold a substantial amount of these fragments. The post-mortem images of the laminated sandwich glass panel are shown in Fig. 6. It is evident from the post-mortem images that there is substantial fragmentation in the case of the laminated sandwich glass panel. However, the protective film is able to contain these pieces and prevent them from flying off. Also, there is no cracking in either of the layers (both on the front and back face of the glass panel) of the protective film. The laminated sandwich glass panel is around 15% thicker than the other panels because of the protective film that had been adhered to both the front and back face of the panel. The higher thickness also contributes to the improved performance of the laminated sandwich glass panel. The laminated sandwich glass panel was also tested at a higher incident pressure (1 MPa, which is twice that of the incident pressure at which the other panels were tested) and it was found that the panel survived the shock loading and that there was no catastrophic failure.

Overall, it can be concluded that the laminated sandwich glass panel has better blast mitigation properties than the other four panels. The clear glass panel and tempered glass panel have the worst blast mitigation properties and are shattered into pieces when subjected to the shock loading. The sandwiched glass performs better than the wired glass panel, but it still has fragmentation and shattered glass pieces flying around. The fragmentation in the case of the sandwich glass panel is lower as compared to that in the wired glass panel. Also, the diameter of the through hole formed in the wired glass panel is larger as compared to that in the sandwich

glass panel. This improvement in the blast response of the sandwich glass panel can be attributed to the PVB interlayer which helps in withholding some of the shattered glass pieces.

Task 2. Effect of plate curvature on blast response of aluminum panels

Experimental and numerical studies were conducted to understand the effect of plate curvature on blast response of aluminum panels. A shock tube apparatus was utilized to impart controlled shock loading to aluminum 2024-T3 panels having three different radii of curvatures: infinity (panel A), 304.8 mm (panel B), and 111.76 mm (panel C). Panels with dimensions of 203.2 mm x 203.2 mm x 2 mm were held with mixed boundary conditions before applying the shock loading. A 3D Digital Image Correlation (DIC) technique coupled with high speed photography was used to obtain out-of-plane deflection and velocity, as well as in-plane strain on the back face of the panels. Macroscopic postmortem analysis was performed to compare the yielding and plastic deformation in the three panels. The results showed that panel C had the least plastic deformation and yielding as compared to the other panels. A dynamic computational simulation that incorporates the fluid-structure interaction was also conducted to evaluate the panel response. The computational study utilized the Dynamic System Mechanics Analysis Simulation (DYSMAS) software. The model consisted of the shock tube wall, the aluminum plate, and the air (both internal and external) to the tube walls. The numerical results were compared to the experimental data. The comparison between the experimental results and the numerical simulation showed a high level of correlation using the Russell error measure.

Material details

Panels with three different radii of curvature were utilized in the experiments: infinite radius of curvature (Panel A), 304.8 mm radius of curvature (Panel B) and 111.76 mm radius of curvature (Panel C). The specimens are shown in fig. 7. Each experiment was repeated three times to assure consistent results. The specimens were 203.2 mm long x 203.2 mm wide x 2 mm thick, made out of 2024 T3 Aluminum. For the case of curved panels, the arc length of the curved edges corresponds to the plate length. Tensile testing of the material was performed in accordance with the ASTM E8 standard to characterize its material properties for use in the simulation.

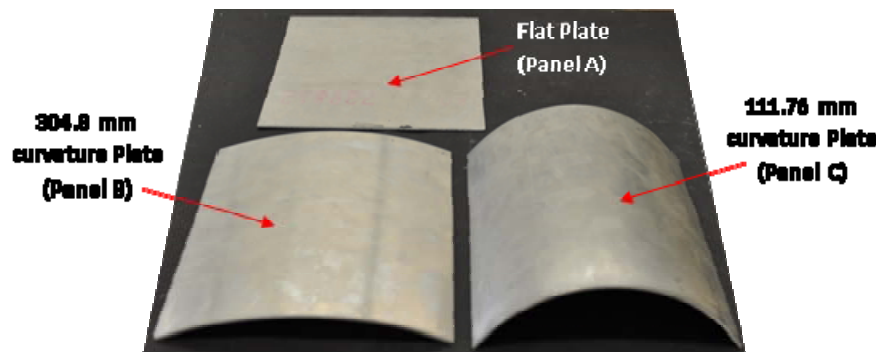


Figure 7: Specimen

Computational modeling

Computational simulations of the shock loading events have been performed with the DYSMAS software. This software is developed and maintained by the Naval Surface Warfare Center, Indian Head. It consists of a Eulerian fluid solver, GEMINI, a Lagrangian structural solver, DYNA_N, and an interface module which couples the two. Gemini is a high order Eulerian hydrocode solver for compressible, inviscid fluids. DYNA_N is a Lagrangian non-linear, explicit finite element code for structural applications. The interface module is a standard coupler interface which allows the fluid and structural codes to share the required variables for the fluid structure interaction problem.

The DIC technique is used to obtain the out-of-plane deflections and velocities as well as the in-plane strains on the back surface for all the three geometries. The shock tube used in this study provides a uniform pressure pulse over a circular area of 4562.2 mm^2 (muzzle area). This is verified by the DIC image of the out of plane displacement on flat plate during shock impingement as shown in fig. 8. The image taken at $50 \text{ } \mu\text{s}$ shows a uniform displacement of 3 mm over an area equal to the muzzle area.

Macroscopic post-mortem analysis

The post-mortem images of the shock loaded aluminum panels are shown in fig. 9. All of the panels had large inelastic deformations (Mode I). The plastic deformation in panel A was much more pronounced when compared to the other two panels. It was the least in panel C. Panels A & B had plastic deformation over the whole non clamped surface, whereas panel C had plastic deformation over an arc length of 105 mm around the central region. Panel A had perpendicular yield line formations (hinge formation) which extended from the panel corners towards the center of the panel as shown in fig. 9(a). A similar kind of hinge formation was observed in the panel B. These yield lines extended from the top corner to the bottom on both the edges as shown in fig. 9(b). Panel C had no yield line formation. It had an elliptically shaped plastically deformed region in the center (fig. 9(c)). The macroscopic post-mortem analysis and DIC deflection, velocity and in-plane strain analysis shows that the panel C (111.76 mm radius of curvature) has the least plastically deformed area out of the three panels. Also it has practically no yield line (hinge) formation as compared to the other two panels. This shows that panel C has a better blast mitigation property as compared to the other two panels.

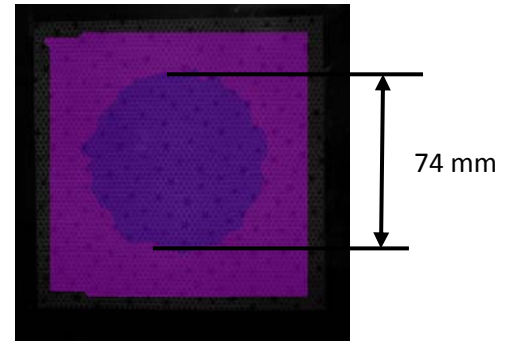


Figure 8: Full-field Deflection at $50 \text{ } \mu\text{s}$

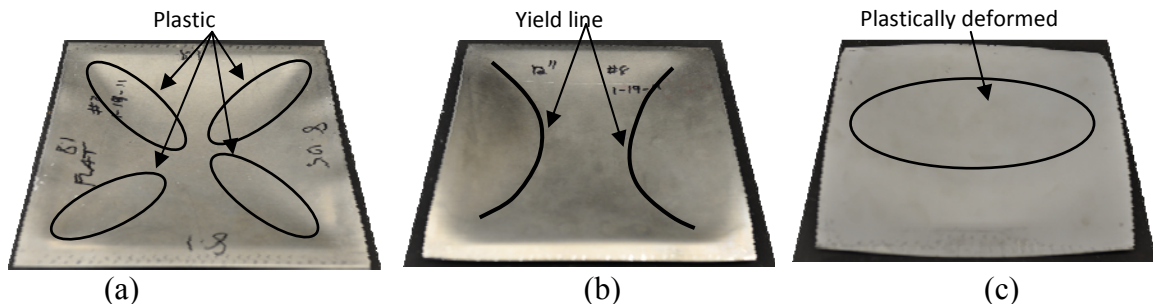


Figure 9: Post-mortem evaluation of (a) Flat Panel (b) 304.8 mm radius of curvature and (c) 111.76 mm radius of curvature

Task 3. Blast response of 32-layered curved carbon fiber panels

Experimental study is underway to understand the effect of plate curvature on blast response of 32-layered carbon fiber panels. A shock tube apparatus has been utilized to impart controlled shock loading to carbon fiber panels having three different radii of curvatures: infinity, 304.8 mm, and 111.76 mm. The panels have a dimensions of $203.2 \text{ mm} \times 203.2 \text{ mm} \times 2 \text{ mm}$ are held with fixed boundary conditions before applying the shock loading. A 3D Digital Image Correlation (DIC)



Figure 10: Post-mortem image of flat panel

technique coupled with high speed photography has been used to obtain out-of-plane deflection and velocity, as well as in-plane strain on the back face of the panels. Macroscopic postmortem analysis will be performed to understand the effect of curvature to blast loading. Some initial experiments were conducted. Post-mortem image from one of the experiments in which flat panel was subjected to shock loading is shown in fig. 10. Post-mortem analysis shows that there is delamination and fiber breakage in the panel. This study is underway and extensive experiments will be performed to understand the effect of curvature to blast loading.

Students Supported

1. Puneet Kumar
2. Matthew Jackson
3. Daniel Gracia
4. Jefferson Wright
5. Andrew Krystnewicz

Conference & Journal Publications

1. E. Wang, N Gardner and A. Shukla, "The blast resistance of sandwich composites with stepwise graded cores", *International Journal of Solid and Structures*, 46, 3492-3502, 2009.
2. E. Wang and A. Shukla, "Analytical and Experimental Evaluation of Energies during Shock Wave Loading", *International Journal of Impact Engineering*, *International Journal of Impact Engineering*, 1188-1196, 2010.
3. P. Kumar and A. Shukla, "Dynamic response of glass panels subjected to shock loading", *Journal of Non-Crystalline Solids*, DOI 10.1016/j.jnoncrysol.2011.08.009, 2011.
4. N. Gardner, E. Wang, P. Kumar and A. Shukla, "Blast mitigation in a sandwich composite using graded core and polyurea interlayer", *Experimental Mechanics*, DOI 10.1007/s11340-011-9517-9, 2011.
5. M. Jackson, A. Shukla, "Performance of sandwich composites subjected to sequential impact and air blast loading", *Composites: Part B*, 42, 155–166, 2011.
6. E. Wang and A. Shukla, "Blast Performance of Sandwich Composites with In-Plane Compressive Loading", *Experimental Mechanics*, DOI 10.1007/s11340-011-9500-5.
7. E. Wang, N. Gardner and A. Shukla, "Experimental study on the performance of sandwich composites with stepwise graded cores subjected to a shock wave loading", *SEM Annual Conference and Exposition on Experimental and Applied Mechanics*, Albuquerque, New Mexico , June 1-4, 2009.
8. N. Gardner, "Blast performance of sandwich composites with discretely layered core", *SEM Annual Conference and Exposition on Experimental and Applied Mechanics*, *Student Paper Competition*, Albuquerque, New Mexico , June 1-4, 2009.
9. S.A. Tekalur, E. Wang, M. Jackson and A. Shukla, "Failure Behavior and energy absorption of sandwich composites under dynamic loading", *SEM Annual Conference and Exposition on Experimental and Applied Mechanics*, Albuquerque, New Mexico , June 1-4, 2009.
10. E. Wang and A. Shukla, "Evaluation of Incident, Reflected and Deformation Energies During Blast Experiments", *SEM Annual Conference and Exposition on Experimental and Applied Mechanics*, Albuquerque, New Mexico , June 1-4, 2009.
11. N. Gardner and A. Shukla, "The Blast Response of Sandwich Composites With a Functionally Graded Core", *SEM Annual Conference and Exposition*, Indianapolis, Indiana, June 7-10, 2010.
12. N. Gardner and A. Shukla, "The Blast Response of Sandwich Composites With a Functionally Graded Core and Polyurea Interlayer", *SEM Annual Conference and Exposition*, Indianapolis, Indiana, June 7-10, 2010.

13. E. Wang and A. Shukla, "The Blast Response of Sandwich Composites with In-Plane Pre-Loading". SEM Annual Conference and Exposition, Indianapolis, Indiana, June 7-10, 2010.
14. P. Kumar and A. Shukla, "Blast Loading response of Glass Panels", SEM Annual Conference and Exposition, Indianapolis, Indiana, June 7-10, 2010.
15. E. Wang and A. Shukla, "Core Deformation of Sandwich Composites under Blast Loading", SEM Annual Conference and Exposition, Indianapolis, Indiana, June 7-10, 2010.
16. E. Wang and A. Shukla, "Blast Response of Sandwich Composites using Digital Image Correlation Technique", 9th International Conference on Sandwich Structures (ICSS9), Caltech, Pasadena, California, June 14 - 16, 2010.
17. E. Wang and A. Shukla, "Performance of Pre-Stressed Sandwich Composites Subjected to Shock Wave Loading", 14th International Conference on Experimental Mechanics (ICEM 14), Poitiers, FRANCE July 4-9, 2010.
18. P. Kumar and A. Shukla, "Dynamic response of glass panels subjected to shock loading", Implast 2010, SEM Fall Conference on Plasticity and Impact Mechanics, October 12-14, Providence, 2010.
19. P. Kumar and A. Shukla, "Dynamic response of shock loaded architectural glass panels", SEM Annual Conference and Exposition on Experimental and Applied Mechanics, June 13 - 16, Uncasville, 2011.
20. P. Kumar and A. Shukla, "Effect of curvature on shock loading response of aluminum panels", SEM Annual Conference and Exposition on Experimental and Applied Mechanics, June 13 - 16, Uncasville, 2011.
21. P. Kumar and A. Shukla, "Blast response of architectural glass panels", SEM Annual Conference and Exposition on Experimental and Applied Mechanics, June 13 - 16, Uncasville, 2011.

Attenuation and mitigation of stress waves propagating in blast shielding materials

Carl-Ernst Rousseau

Mechanical Engineering; University of Rhode Island

Objectives

One of the most important aspects of mitigation consists in the ability to develop effective structures and materials that can withstand the extreme loading conditions found in blast and impact situations. To succeed in fulfilling those tasks, these materials must also be subject to structural constraints related to weight and volume, thereby the necessity of selecting novel, light-weight composites, or heterogeneous materials in the search for ideal shielding and structural integrity. Particulate-, and fiber-based composites have been an essential element of novel material development, and thus require behavioral scrutiny at high loading rates. The response of these multi-phase materials under dynamic conditions is complex due to the considerable wave interactions and local failure modes that exist within the non-homogeneous material. Thus, we propose to investigate and quantify behaviors in particulate model composites, by carefully tracking propagating waves within them. Attenuation work on these materials has thus far been performed on those featuring hollow inclusions, which provides a much lighter version of the original material often at the detriment of strength. However, the work performed has highlighted a range of conditions (e.g., concentration, size) where use of these syntactic foams may still be acceptable as they do retain or enhance wave dampening capabilities. The next stage will consist in performing similar attenuation work on materials having solid inclusions. These will generally have a higher density but may boast of more dynamic resilience. Again, we will investigate the ranges within which windows of improved attenuation may lie. Ballistic impact of these, as well as the syntactic foams will follow for direct stress evaluation.

Details of Research

Task 1 - Direct Stress Attenuation: The effectiveness of each material system is determined primarily through a stress wave propagation method, where stress attenuation over a specific distance within the material is recorded by means of embedded piezoresistive stress gages. We have also acquired key components of a Photonic Doppler Velocimetry, a system through which deflection in the path of the light reflected from the back face of a specimen is captured. These variations are effectually indicative of the velocity profile (particle velocity) at the rear of the specimen and provides a means of verification of the stress recording by means of direct stress-speed relations. In addition, the technique is attractive as it is a non-invasive, non-contact method, and circumvents any slight deviation that might result from the presence of the gage in the material.

Task 2 - Internal Friction: Inherent internal friction within the material is being sought as this effect is representative of the mechanism present in energy dissipation, thereby in the dampening of the damage caused by nefarious external effects. The initial effort in this area is focussed on hollow glass particulates, or microballoons, immersed within an epoxy matrix, forming what is generally called a syntactic foam. Such material have numerous application in situations requiring a combination of reduced density, high compressive strength, low moisture absorption, and improved damping properties. Thus, they have become a frequent component in sandwich composites used in aerospace and maritime applications. Ultrasonic waves are launched into the material. Retrieval of this wave upon exiting the material provides a measure

of the internal friction elicited in reducing its magnitude. Ultrasonic attenuation coefficient from experiment is compared with a previously developed theoretical model for low volume fractions, and takes into account attenuation loss due to scattering and absorption. In addition to evaluating the apparent attenuation, quasi-static compressive tests were also conducted to fully characterize the material. Both quasi-static and dynamic properties, as well as coefficients of attenuation, ultrasonic velocities are strongly dependent upon the volume fraction and size of the microballoons. Criteria are established to provide guidance for the usage of these materials under a wide range of conditions. These same materials have been investigated with the particulates positioned in a functionally-graded configuration. Further expansion of these experiments will be conducted with solid inclusions.

Task 3 - Stress Wave Scattering: At least as important in heterogeneous material, is the scattering or dispersion across grain boundaries, and at particle or material interfaces. This mechanism generates complex stress wave interactions that can greatly diminish stress propagation-induced failure. Thus, our goals here is to enhance the scattering mechanisms through manipulation of the microstructure.

Task 4 - Numerical Modeling: Companion finite element simulations aimed at guiding the direction of the experiments are performed routinely. Conversely, each experiment is simulated numerically in an attempt to establish better simulations techniques, and sound predictive methods. Upon correlation of specific empirical and numerical data, the latter can then be used to surmise the full-field, detailed information about the material behavior.

Results

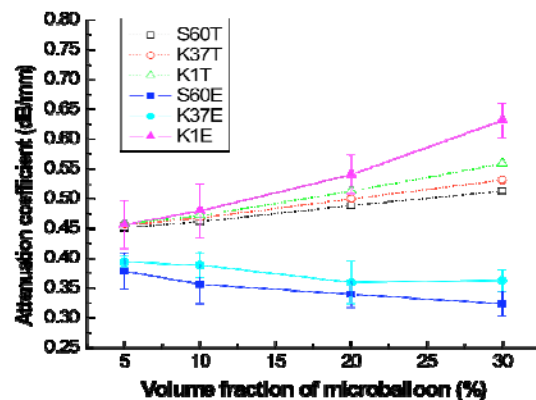
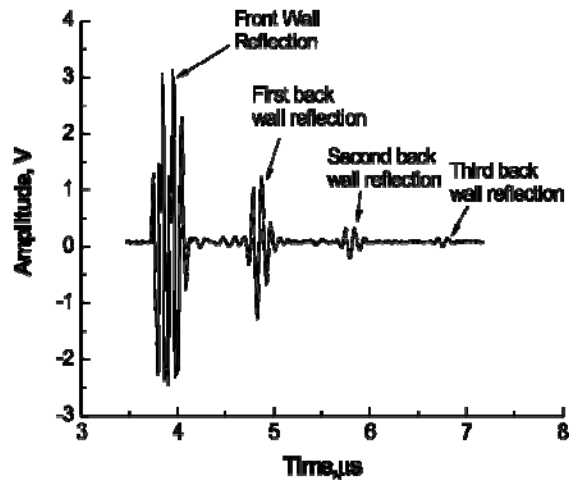
Three types of micro-balloons, with different outer and inner diameters, were selected. Ultrasonic Characterization was carried out in an immersion tank for longitudinal wave speed and attenuation measurement. A typical ultrasonic waveform obtained as shown in the figure. The peaks corresponding to the back wall reflections of the specimen can be clearly seen in the figure. The location along the time axis and the corresponding amplitude are noted for the first two back wall reflections and are used to calculate the longitudinal wave speed and attenuation of the specimen.

Various models of attenuation coefficient have been proposed to evaluate the attenuation coefficient of syntactic foams. One recent model, developed by Mylavarapu and Woldeesenbet is based on ultrasonic attenuation by scattering and absorption of spherical elastic microballoons taking into account the matrix attenuation, and the effect of particle size, porosity and radius ratio.

Experimental and Theoretical results for the attenuation coefficient are plotted in the adjacent figure. Attenuation coefficient of largest microballoon K1 (65 micron diameter) increases whereas the attenuation coefficient of K37 (45 micron diameter) and S60 (30 micron diameter) microballoons decreases with volume fraction.

Because they are composed of larger voids and have smaller wall thicknesses, K1 based composites interact with the plane longitudinal wave causing more scattering and absorption. Wave attenuation decreases as volume fraction increases for S60 and K37 syntactic foams. It can further be noted that as the radius ratio decreases the material becomes more elastic, the absorption cross-section becomes zero and does not contribute to wave decay. Hence the attenuation of K37 microballoon is higher than S60 due to larger voids for the same volume fraction and higher density.

In syntactic foam composites, wave propagation behavior, such as scattering at inclusions governs the elastic properties obtained by ultrasonic testing and is determined by the ratio of wavelength to particle size. The range of the wavelength to particle size ratio was between 35-92 at 1 MHz. Hence, the ultrasonic wave will pass through clusters rather than millions of particles that are present in the composite. Therefore, scattering of ultrasonic wave does not occur at each and every particle-particle interface rather than between clusters of particles. Since the ratio is smaller for K1 spheres than for K37 and S60, there is more probability of wave-particle interaction to occur hence a case for increase in wave attenuation. Further, larger voids and smaller wall thickness, in the case of K1, results in microballoon interaction with the plane longitudinal wave causing more scattering and absorption.



Accomplishments

Publications

A presentation was made in June 2011 at the Society for Experimental Mechanics conference on effective means of evaluating spallation in materials. A journal publication is set for publication this year in the International Journal of Nonlinear Science & Simulations, entitled 'Investigation into the spall strength of cast iron', by Plume & Rousseau. A journal publication will appear in October 2011 in Materials Science & Engineering, entitled 'Deformation characteristics of low carbon steel subjected to dynamic impact loading', by Visser, Sun, Gregory, Plume, Rousseau, & Ghonem. A journal publication is currently under review in International Journal of Polymer Science, entitled 'Dynamic attenuation properties of syntactic foams', by Ale & Rousseau.

Students

One student received his Master's degree in May 2011 (Bhaskar Ale) as a result of his work on this activity. Two other students, doctoral and a master's student are fully supported by this effort. The two students supported are, respectively, Gifford Plume and Miguel Goni. One undergraduate student, Christian Mejia is also partially supported by this project.

Collaborations

The techniques used in the research are very versatile in that their application is universal to any material. Thus, they have led to three collaborative ventures. The first relates to the study of structural steel. Properties of the material are evaluated at high temperatures in their virgin state. This is, again, repeated after impact, thus simulating a material state that is subsequent to an explosion or collision. The embedding of the gages within the material provide a faithful profile of the internal loading, which can therefore be inserted as numerical input to numerical simulations. Inference of the health monitoring of buildings is the ultimate goal of this exercise.

The second collaborative project involves the spallation study of cast iron, with the national laboratories. Spallation is a common occurrence in metals that follows a strike or an explosion.

The third collaborative project consist in a dual proposal to the National Science Foundation submitted on October 1, 2011 with the University of Connecticut. It consists in experimentations on biologically-inspired materials at URI, with numerical simulations performed at UConn, in an effort to develop effective shields based on natural observations.

Structural Response to Non-ideal Explosions

PI J.E. Shepherd; J.S. Damazo, K. Chow-Yee
California Institute of Technology

Objective and Summary of Activities in 2010–2011

Experiments and numerical simulations were performed in the Explosion Dynamics Laboratory at Caltech to investigate the effect of non-ideal explosions on thin-walled steel tubes. Gaseous detonations were used as a model to simulate various internal explosions. It is our objective to develop the capability to predict the degree of plastic deformation induced by a non-ideal explosion in steel tubes and to investigate methods to mitigate the extent of this deformation.

Experiments were performed using 304L stainless steel welded specimen tubes so that more accurate comparisons with numerical simulations may be obtained than previous work with mild (C1010) steel. The detonable mixture used was stoichiometric $\text{C}_2\text{H}_4\text{-O}_2$ of initial pressures of 0.5 bar, 2 bar, and 3 bar. This is the same mixture and pressures examined in the mild steel results thereby allowing direct comparison. For the low pressure case ($P_0 = 0.5$ bar), the deformation was purely elastic. The 2 bar and 3 bar initial pressure cases both resulted in plastic deformation and were the focus of the present study. A Johnson-Cook material model was used in an LS-DYNA finite element simulation to obtain quantitatively close comparisons for both of these plastic deformation cases. Polyurea coatings applied to both the interior and exterior of the tubes were investigated to determine the mitigation capability through the comparison of maximum plastic deformation with and without the coatings. Preliminary investigation of the mechanism of shock wave-boundary layer interaction and bifurcations were carried out to follow up on previous observations of discrepancies in pressure signals from ideal (inviscid) gas dynamic models.

Highlighted Accomplishments

1. Carried out plastic deformation testing with repeated loading using gaseous detonation in stainless steel tubes.
2. Used finite element numerical simulations with a Johnson-Cook material model to obtain quantitative comparison to experimental measurements.
3. Tested polyurea coating as a method of mitigating the material deformation resulting from reflected detonation loading.
4. Performed preliminary investigations exploring the possibility of bifurcation of the shock wave created at the reflecting end of the tube.

Details

It is the goal of these experiments to obtain a guideline such that, given an initial pressure, one may predict whether plastic deformation occurs and, if plastic deformation does occur, to what extent. In order to do this, a facility was previously constructed to allow us to plastically deform 127 mm diameter, 1.5 mm wall thickness tubes with an internal detonation (Figure 1). In order to avoid initiation transients within the specimen tubes, the detonations were initiated in a 1.2 m long thick-wall tube and allowed to develop into a steady near-CJ wave before entering the specimen tube. The presence of a well-formed detonation wave was confirmed with pressure gauges located in the driver tube. To ensure proper wave reflection, the test specimen tubes were held between an aluminum plug and steel collet at the reflection end. A pressure gauge is also located inside the aluminum plug to record the pressure trace in the reflecting end. Tube deformation and movement measurements were obtained with strain gauges—allowing us to record the dynamic material

response to the explosion; final outer-diameter measurements were also obtained using an outside micrometer.

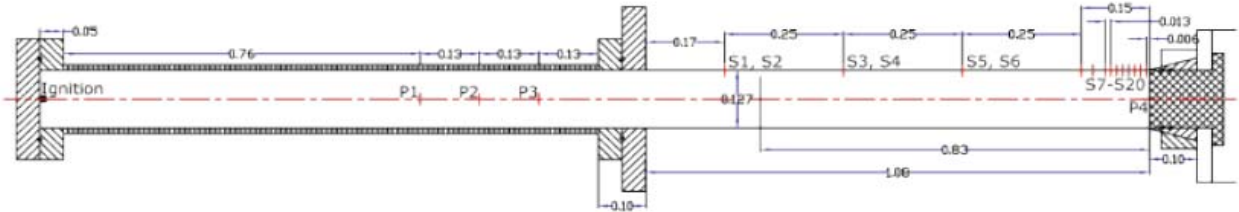


Figure 1. Diagram of experiment used in detonation experiments, dimensions in meters.

The first series of experiments in 2009-2010 was performed in C1010 mild steel tubes with a 1.5 mm wall thickness and 1.2 m length. However when simulations were performed in LS-DYNA to model the material deformation, it was determined that for the strain rates observed in experiments ($> 100 \text{ s}^{-1}$) that conventional rate-dependent material models were not adequate for modeling despite being calibrated against high-strain rate testing. For the subsequent experiments in 2010-11 that are described in this report, we used 304 stainless steel tubing as the test material. 304 stainless is a much better characterized material, particularly at high strain rates and is widely used in explosion containment systems due to the high ductility. There is also available a widely-used and well calibrated high-strain rate model of stainless steel plasticity that we can use in LS-DYNA simulations.



Figure 2. Stainless steel specimen tube subjected to five repeated detonations of mixture $\text{C}_2\text{H}_4\text{--O}_2$ and initial pressure 2 bar. The picture on the right is placed on a 5 mm grid and stretched horizontally to emphasize the periodic deformation mode.

Figure 2 shows a specimen tube after five repeated detonations of initial pressure 2 bar. The surface of the tubes shown in Figure 2 exhibit a ripple pattern previously observed in the mild steel tubes. The measured ripple wavelength was $70 \text{ mm} \pm 6 \text{ mm}$. The single degree-of-freedom model previously developed predicts a ripple wavelength of 67 mm, which is reasonable agreement and consistent with the measurement uncertainty. The computation of the wavelength was derived by Karnesky¹ as part of our research in 2009-10. LS-DYNA simulations were performed compared to outer-diameter data extracted from post-test examination. Figure 3(a) and (b) illustrate the

¹ J. Karnesky, Detonation Induced Strain in Tubes. PhD thesis, California Institute of Technology, Pasadena, California, May 2010.

comparison between the experiment and computations. It is observed that the Johnson-Cook material model applied to 304L stainless steel gives much better agreement than the previously obtained C1010 mild steel results. This improved agreement is due to stainless steel not only being a better characterized material than mild steel but also the Johnson-Cook relation is much more suitable model for modeling plastic deformation than the piecewise strain-hardening models with ad hoc strain rate corrections that were used in the mild steel case.

After the deformation resulting from reflecting detonations in stainless steel tubes had been characterized, methods to mitigate the deformation were explored. A polymer coating was selected for its proven ability of reducing plastic deformation caused by events similar to detonation loadings. A SPI Ultra Bond-100 polyurea coating was spray applied to the outer surface of the tubes to nominal thickness of 3, 4, or 7 mm. Figure 4(a) displays the effect of an external coat of polyurea. We observe that the magnitude of strain is significantly decreased for tubes with polyurea coating. A 3.9 mm coating (tube 13) saw an 8.7% reduction in residual peak plastic strain and a 2.9 mm coating (tube 15) yielded a 14.3% reduction compared to the baseline case of no coating (tube 9).

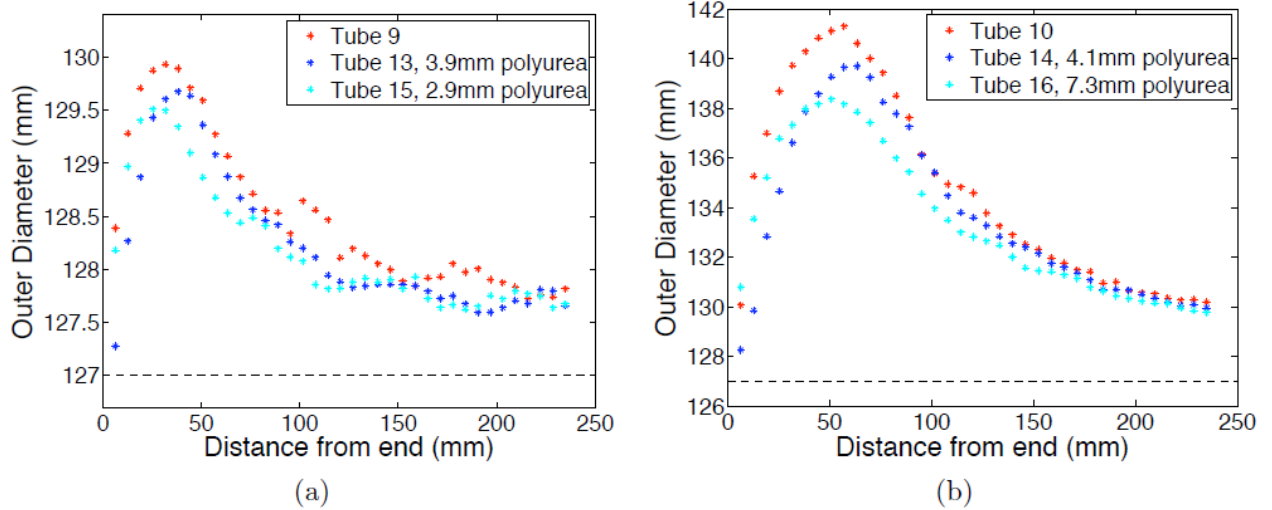


Figure 4 Effect of polyurea on residual plastic deformation after one ethylene–oxygen detonation of initial pressure (a) 2 bar and (b) 3 bar.

Surprisingly, decreasing the polyurea thickness in tube 15 resulted in decreased strain. This may indicate that the mechanism by which polyurea mitigates damage is more complex than the polyurea acting as structural reinforcement and added mass. Three tubes (tubes 10, 14, and 16)

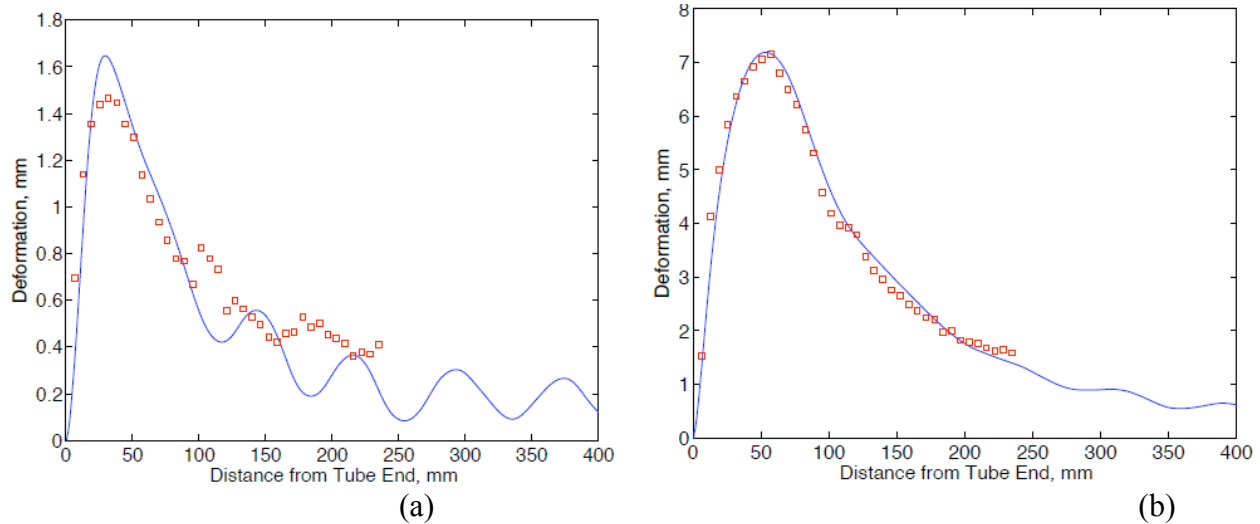


Figure 3 Comparing LS-DYNA results with the outer diameter data obtained after one detonation of initial pressure (a) 2 bar and (b) 3 bar

were subjected to detonations of initial pressure 3 bar. Analogous to the 2-bar experiments, tube 10 was uncoated for a baseline and tubes 14 and 16 had polyurea coatings of nominal thickness 4 mm and 7 mm respectively. Figure 4(b) displays the residual plastic deformation. Here we observe that, like the 2 bar initial pressure experiments, the polyurea significantly lessens the observed deformation. The peak residual strains are reduced by 11.3% and 20.5% for tubes 14 and 16 respectively.

Our experiments examining plastic deformation revealed an anomaly in the shock wave created when the detonation normally impinged on the end wall. Measurements of the shock speed and strength were inconsistent with one-dimensional gas dynamic theory suggesting multi-dimensional effects were occurring. To further investigate the physics of reflecting detonation waves, experiments were performed in the GALCIT Detonation Tube where optical access allowed pictures to be taken of reflecting shock and detonation waves. Figure 5 shows photographs taken with a traditional Z-type schlieren set-up of reflecting shock (a) and detonation (b) waves where the reflected wave is of similar Mach number. In both cases, the incident wave creates a boundary layer on the walls of the test section and a reflected shock wave that brings the gas behind the incident wave to rest. Figure 5(a) shows that the reflected shock wave creates a significant oblique wave structure (termed shock wave bifurcation) and separation of the boundary layer behind the reflected wave. This has been observed previously with shock wave reflection and is an extreme example of the multi-dimensional effects that can cause significant departures from one-dimensional wave propagation models of reflection. Interestingly, the case of an incident detonation wave, Figure 5(b), appears to show very little bifurcation effect in comparison with the incident shock wave. However, these mixtures are not the same as used in our plastic deformation experiments and it is known that the bifurcation extent depends strongly on the gas composition.

Based on this preliminary data, it appears that shock and detonation reflection can result in very disparate extents of shock-wave boundary interaction. We are currently exploring explanations for these differences through analytic and numerical models of the shock-wave boundary layer interaction as well a systematic program of experimentation.

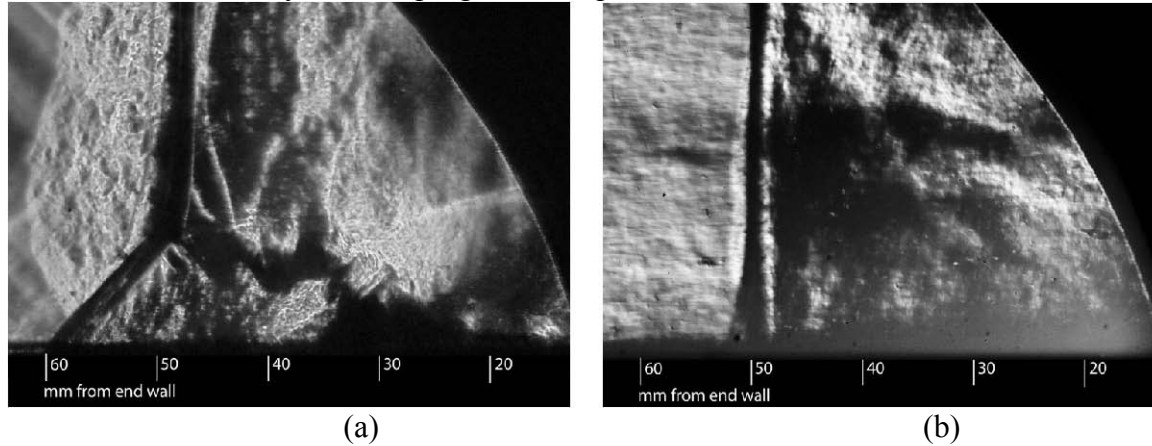


Figure 5 Schlieren photographs taken of (a) reflected shock wave in pure N₂O and (b) reflected detonation wave in 90%N₂O, 10%H₂. The bottom of the image is the floor of the detonation tube, the reflecting wall is located off-screen at $x = 0$, to the right of the images. Both tests had initial pressure 15 kPa and the reflected waves are propagating from right to left.

Future Work

The goal is ultimately to develop a comprehensive model of plastic deformation, rupture, and blast wave generation for both detonation and deflagration loading. The next steps are:

1. Improve our modeling of the loading pressure distribution through the investigation of shock-wave boundary interactions during the detonation reflection process. This will be done through experimentation in the gaseous detonation tube facility which is equipped with an instrumented test section so that simultaneous optical, pressure, and heat flux measurements can be performed during the detonation reflection event.
2. Carry out coupled fluid-structure computations to account for the feedback between deformation and gas dynamics that is observed in the experimental tests and cannot be accounted for by our current models.
3. Develop a test capability for carrying out rupture tests on tubes inside a blast chamber. We are now investigating modifying the existing blast chamber at Caltech to enable tests at higher initial pressures, sufficient to cause rupture. The key engineering challenge is to be able to install the test specimen inside a chamber with limited access.

Publications and Presentations

1. J. Karnesky, J. Damazo, J. E. Shepherd, and A. Rusinek. Plastic response of thin-wall tubes to detonation. In Proceedings of the ASME Pressure Vessels and Piping Conference. July 18-22, Bellevue, WA, 2010. PVP2010-25749.
2. J. Karnesky, J. Damazo, J. Ziegler and J. E. Shepherd “Investigating Shock Wave Boundary Layer Interaction Caused by Reflecting Detonations” 8th ISHPMIE September 5-10, 2010, Yokohama, Japan, Paper No.ISH117.
3. J. Damazo, K. Chow-Yee, J. Karnesky, and J. E. Shepherd “Mitigating Effect of Polymer

4. J. Damazo, J. Ziegler, J. Karnesky, and J. E. Shepherd, "Shock Wave–Boundary Layer Interaction in Reflecting Detonations" 63rd Annual Meeting of APS Division of Fluid Dynamics, November 21-23, 2010, Bulletin of the American Physical Society, 55(16), Abstract BAPS.2010.DFD.HX.2.
5. J. Damazo, J. Ziegler, J. Karnesky, and J. E. Shepherd "Shock Wave Boundary Layer Interaction from Reflecting Detonations" Proceedings of the 28th International Symposium on Shock Waves, University of Manchester, July 17-22, 2011.
6. J. Damazo, J. E. Shepherd, K. Chow-Yee, J. Karnesky "Deformation of Coated Stainless Steel Tubes from Reflected Detonation" 23rd International Colloquium on the Dynamics of Explosions and Reactive Systems, July 24-29, 2011, Irvine, USA. Extended Abstract 257.

All were presentations at national or international meetings. No.1, 2, 3, 5 were also published in the conference proceedings.

Water Blast Mitigation

S. F. Son (PI), A. J. Zakrajsek, L. J. Groven, and D. R. Guildenbecher
Mechanical Engineering, Purdue University

1. Objective

The purpose of this study is to investigate the effectiveness of water as a blast mitigant. Water blast mitigation is being investigated in multiple configurations including: solid water barriers, water sprays and water sheets. An explosion yielding a blast wave can cause catastrophic damage to a building and its personnel. This threat defines an immediate importance for understanding blast mitigation techniques via readily available materials. Specific blast mitigation techniques using water are being studied with the motivation of protecting high risk targets from damage. An initial understanding of the mitigating mechanisms, along with the experimental results from each configuration is presented here.

2. Summary

Since 1968, bombing has accounted for nearly half of international terrorist attacks [1]. A Department of Homeland Security (DHS) brief on the treat of domestic improvised explosives devices (IEDs) indicated that there is increased terrorism intent on attacking high risk targets [2]. Overall a blast wave from a nearby explosive can cause catastrophic damage to an intended target [3]. These simple findings present the immediate importance of protecting high risk structures by being able to mitigate incident blast waves.

For the purpose of this research, water is being studied as a readily available mitigant. Four different water configurations have been designed and tested to provide a detailed overview of the different mitigating mechanisms associated with each configuration. Specific formations of water may be able to protect high risk targets during an elevated warning level, or when a visible threat is detected.

3. Accomplishments

Four different water configurations have been designed, and tested to date. These configurations include solid water barriers, water sprays, and water sheets. Each water configuration provided different insight into different mitigating principles. These blast mitigating principles can not only be applied to water blast mitigation, but other forms of blast mitigation. Overall the water sheet performed the best, mitigating the peak overpressure and impulse of the blast up to 82%, and 77% respectively. These results point out possible advantages of using an unconfined sheet of water as a blast mitigant. Additionally, each of these configurations when compared gave insight into future possibilities of different formations of blast mitigants.

4 Details

4.1 Experimental Setup

Explosive testing was performed using an explosively driven shock tube. The explosively driven shock tube was used to produce a repeatable laboratory size blast wave to interact with the different water configurations. Previous work has shown that using an explosively driven shock tube can give a reasonably repeatable blast profile, similar to open field explosive tests [4-6]. The explosively driven shock tube directs the energy from the blast in one direction allowing the use of less explosives and making laboratory scale experiments plausible.

4.1.1 Water Configuration Setups

The four different water configurations needed to have separate setups and testing procedures. There are three separate testing configurations presented here for the four tests completed. The sponge filled with water was held in place with a Poly(methyl methacrylate) (PMMA) box. Additionally, a box made of PMMA was built for the water-confined tests.

The first spray tests were conducted with a “heavy spray” (Fulljet Nozzle) and a “fine mist” (Fogging nozzle). The mitigation was extremely minimal with no significant change in peak overpressure. From these initial tests it was determined that several different nozzles would need to be studied. Phase doppler interferometry (PDI), and phase doppler particle analyzer (PDPA), were used to develop a new testing matrix and testing configuration for water spray testing. Pressure transducers were placed at interval distances in a given spray so that the attenuation of the blast wave through the multiphase spray system can be quantified. When aligning the sprays it was important to keep a continuous spray in the line of the shock, and to minimize interactions between separate spray nozzles.

A sheet of water was generated with a custom fabricated water sheet generator that operated at a constant flow rate of approximately 56 L/min, producing a laminar sheet approximately 0.125 in thick. Pressure gauges were threaded into a custom manufactured plate to obtain the static pressure of the blast. The experimental configuration included two pressure gauge plates, with two gauges threaded into each plate. These plates were placed in front and behind of the water sheet to measure the properties of the blast wave before and after the water sheet. The water sheet was tested at 8, 12, and 16 inch standoff distances.

4.2 Water Configuration Experimental Results

4.2.1 Sponge and Solid Water Barrier Results

In comparison to the reference gauge, the dry sponge slightly lowered the peak overpressure (4.5%) while increasing the impulse (90%) and pulse duration (~60%). The wet sponge lowered the peak overpressure (54%) while significantly increasing both the impulse and pulse duration. These results verify the importance of multiple materials and layers (impedance mismatches) in blast mitigation. Large impedance mismatches are inefficient at transmitting blast waves.

The PMMA box filled with water showed a decrease of peak overpressure by 14%, a decrease of impulse by 42% and a decrease in pulse duration by roughly 50%. The empty box (no water) performed better at diminishing the peak over pressure (~56%) and slightly worse at decreasing the impulse (~25%). In contrast, the pulse duration was broadened by 27% in this case. The reason the empty box performed better than the box full of water may be due to multiple layer impedance mismatches.

4.2.2 Water Spray Results

From the new test matrix the small droplets performed the best at mitigating the peak overpressure. Overall the spray tests did not show any distinct difference between the high or low volume fractions tested. The main differences in the blast parameters were due to the droplet size differences. The averaged small droplet sprays had a peak overpressure mitigation of 43.6% at 8 inches into the spray. Additionally, as the shock passed through 14 and 20 inches into the spray a larger mitigation percentage of around 60% peak overpressure reduction was seen. The results obtained at the Naval Research Laboratories [7, 8], specifically the overpressure reductions are similar to the findings presented here. The impulse and positive pulse of the blast was not significantly affected by the sprays. Figure 1 shows a comparison of the droplet size and volume fractions of different sprays compared to the free field (no spray). The spray's discontinuous surface reduced the reflected wave because of less impedance mismatch. The effects of evaporation, droplet breakup, atomization, and phase change are the main mitigating factors of the water spray.

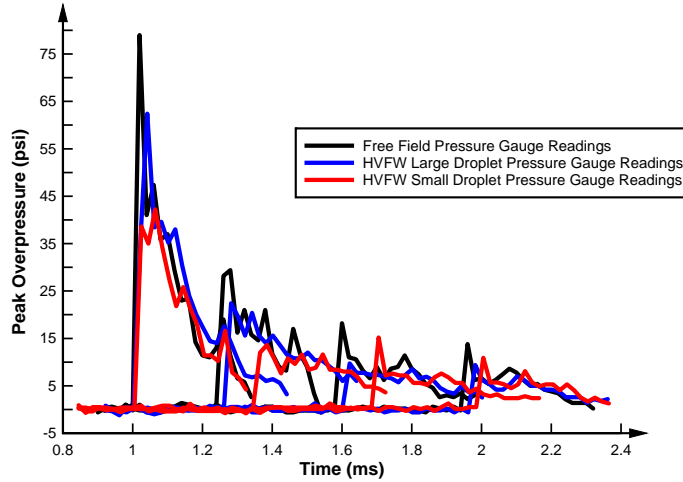


Figure 1. High volume fraction of water sprays vs. free field.

4.2.3 Water Sheet Results

The results show that the unconstrained free flowing water sheet significantly reduces the overpressure and impulse from the blast. At the 12 in standoff distance the peak overpressure is reduced by 82% and the impulse is reduced by around 77%. Figure 2 shows the pressure traces for all four pressure gauges with a water sheet standoff distance of 12 inches for a typical test. Figure 2 also shows the ramped profile of the transmitted blast wave through the water sheet, and how it compares to a free field (no water sheet) blast profile. There was no noticeable distinction between the standoff distance and blast parameters. Also, the positive pulse duration was seen to decrease for all of the blast conditions except for one. The standard error was calculated between the three experiments performed at each condition showing repeatable results.

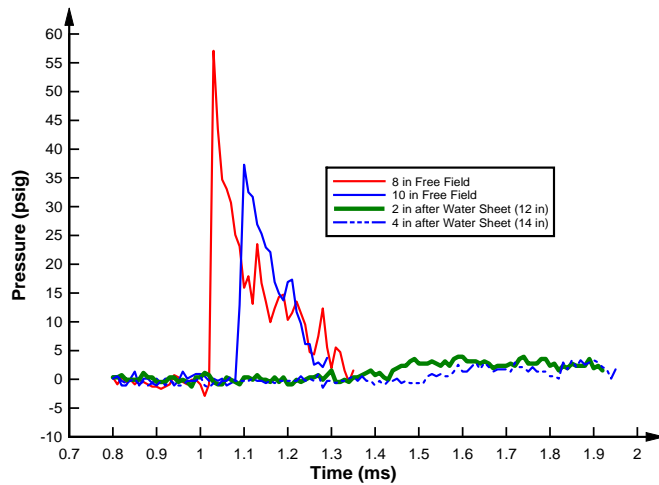


Figure 2. Pressure trace of a typical blast test with a water sheet at a 12 inches standoff.

The blast wave interaction with the water sheet was imaged with the shadowgraphy technique described in Settles work [9]. Select images from the high-speed video are shown in Fig. 3. The reflected wave seen in the third image is due to the impedance differences between the air and water. In the fourth image a weak transmitted blast wave is observed. Along with the impedance mismatch the water sheet is mainly effective at mitigating the blast wave by momentum transfer and breakup of the liquid sheet. Comparison with the free field Mach numbers indicates that the transmitted blast wave has been

attenuated by the water sheet. The observed shadow of the water sheet is interpreted to be the breakup of the liquid sheet into smaller fragments of water.

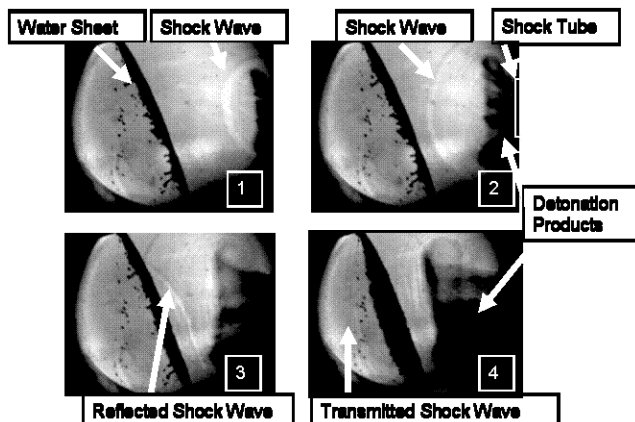


Figure 3. High speed shadowgraphy of water sheet at 13 in standoff distance.

5. Conclusions and Discussion of Test Results

From the four fundamentally different testing configurations experimental comparisons along with qualitative conclusions were obtained. From the sponge and solid water barrier tests initial observations resulted in an initial glimpse into importance of impedance mismatch, along with the need for unconfined mass of water. These tests led to the water sheet configuration that performed the best at mitigating the blast wave to date. The water sheet effectively mitigated the blast wave likely due to a combination of momentum transfer (translation of the water), and two impedance mismatches (continuous surface area). The spray tests most likely less impedance mismatch and momentum transfer than the water sheet. The primary mitigation mechanisms would then be atomization, droplet breakup, phase changes, and evaporation. These effects did not prove as beneficial when compared to the water sheet.

Each test configuration is useful in discovering the blast attenuation mechanisms associated with different water geometry, however, it also has not been determined how mass loading affects these geometries and the shock water interactions. Through these different configurations, and other blast mitigation research, general guidelines can be stated or in most instances re-stated for effective blast mitigation.

General Concepts for Water Blast Mitigation and Blast Mitigation are Summarized Below:

- **Impedance Mismatch**
 - Having multiple layers of material that result in frequent and large impedance mismatches (density variations) improves mitigation. Air gaps between layers of materials are often beneficial due to the low density of air compared to most materials.
 - Having a large, continuous surface area to reflect a large portion of the blast wave. Reflecting the blast wave back towards the source or away from the target can be a successful mitigation scheme and is mainly due to impedance mismatches (density variations).
- **Momentum Transfer**
 - Using an unconfined mass that can translate/deform while it reflects an incident blast wave is beneficial. Smaller droplets are more effective at mitigation, but the volume fraction does not have as big of an effect.

These guidelines have been qualitatively revealed through analyses of different water configurations under blast loading along with background research and other experiments involving blast

mitigation. These guidelines should only be used as general concepts when designing blast-mitigating systems for testing. Additionally, most of these guidelines have been previously documented and investigated by other researchers of blast mitigation.

6. Students Supported

Andrew Zakrajsek

7. Conference and Journal Publications

- We plan to submit these results to the Journal of Shock Waves within the next few months.
- A conference paper will appear in the proceedings of the 17th APS Shock Compression Conference and is titled, “ Experimental and Computational Study of Water Blast Mitigation Associated with Different Water.”
- Some of this work was presented at 17th APS Shock Compression Conference on June 29, 2011. A poster was presented at DHS Review Meeting for ALERT research projects.

8. Future Work

As testing continues, the mitigating mechanisms will be investigated with ALE3D or CTH modeling. It is important to better understand the mechanisms associated with water blast mitigation. A small scale water sheet testing facility is built and assembled. This will allow us to study the water sheet on a more fundamental basis, along with trying to control for mass loading to compare it to the water spray tests. The small water sheet tests will also allow testing of water sheets of different thickness conveniently. Sand-Water slurries may also be tested later may also be considered.

9. Works Cited

1. National Research Council. “Protecting Buildings from Bomb Damage: Transfer of Blast-Effects Mitigation Technologies from Military to Civilian Applications,”. Washington, DC: National Academy, (1995). Print.
2. Domestic Improvised Explosive Device (IED) Threat Overview.
<http://publicintelligence.info/DHS-DomesticIED.pdf>
3. B.M. Luccioni, R.D. Ambrosini and R.F. Danesi, Analysis of building collapse under blast loads, *Eng Struct* 26 (2004), pp. 63–71.
4. Alley, M. D. “Explosive Blast Loading Experiments for TBI Scenarios: Characterization and Mitigation,”. Thesis. West Lafayette, IN / Purdue University, (2009). Print.
5. Benjamin Schimizza, Steven F. Son, Rahul Goel, Andrew P. Vechart, Laurence Young. An experimental and numerical study of blast induced shock wave mitigation in sandwich structures. 2010
6. Freiwald, D. A.; “Approximate Blast Wave Theory and Experimental Data for Shock Trajectories in Linear Explosive Driven Shock Tubes,”. JPN J APPL PHYS, vol. 43, no.5, pp. 2224-2226, (May 1972).
7. Bailey, Jean L., Farley, John P., Williams, Frederick W. “Blast Mitigation Using Water Mist” NRL Memorandum Report 6180—06-8933, 18 January 2006.
8. Willauer, Heather D., Ananth, Ramagopal, Farley, John P., Williams, Frederick W. “Blast Mitigation Using Water Mist: Test Series II” NRL Memorandum Report 6180 – 09 – 9182, 12 March 2009.
9. Settles, G., “High-Speed Imaging of Blast waves, Explosives, and Gunshots,”. AM SCI, vol. 94, No. 1, (2006), pp. 22-31.

Self Healing Materials for Autonomic Mitigation of Blast Damage

Nancy R. Sottos; Scott R. White

Beckman Institute for Advanced Science & Technology

University of Illinois at Urbana-Champaign

I. Objective

The aim of this project is to develop self-healing composite sandwich panels for mitigation of blast damage (Fig. 1). Blast events cause the foam core to fracture and the composite face sheets delaminate, significantly reducing structural stiffness and sandwich efficiency of the composite system. Self-healing of core and face sheet damage will enable recovery of mechanical integrity and should result in enhanced resistance to multiple blast events.

II. Accomplishments

Over the past year we made significant progress towards achieving a self-healing sandwich panel. Specific accomplishments summarized in this report include:

- Incorporation of bio-inspired microvascular networks into cellular materials to deliver expansive foam healing chemistries suitable for rapid, macro-scale blast damage recovery in polymeric foam sandwich core materials.
- Demonstration of self-healing in a commercial, polyisocyanurate (PIR) foam core using a 3-pt. Single Edge Notched Bend (SENB) Mode I fracture test under quasi-static loading conditions.
- Development of “sacrificial fiber” technology for fabrication of microvascular, fiber-reinforced polymer composites.

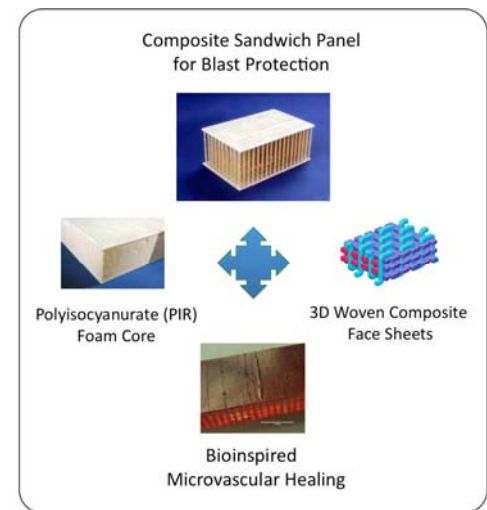


Figure 1 Methodology for microvascular self-healing sandwich panel.

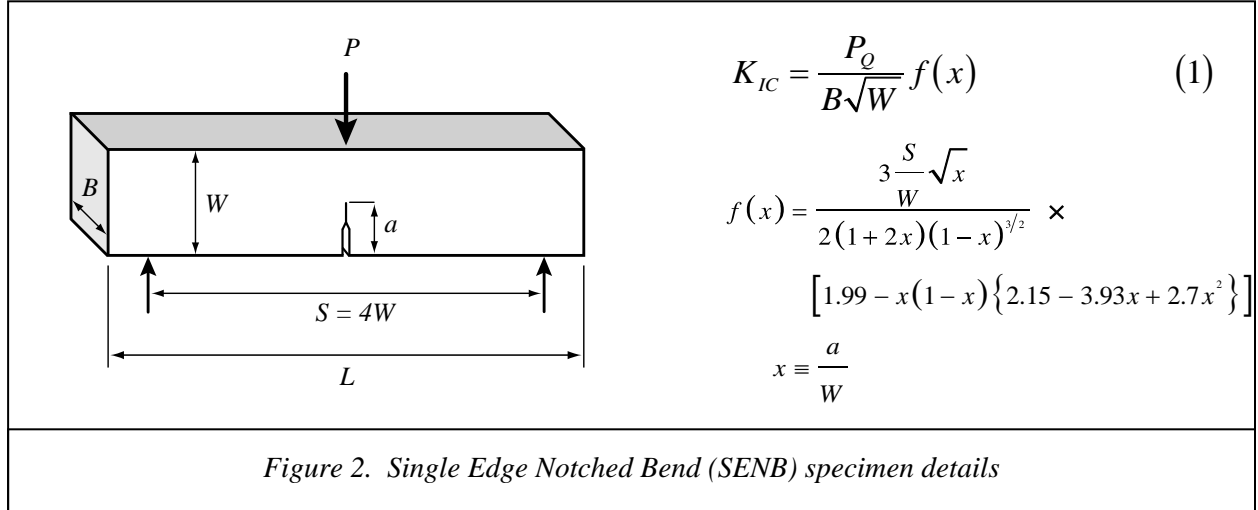
III. Details

1. Microvascular Based Self-healing Polymeric Foam

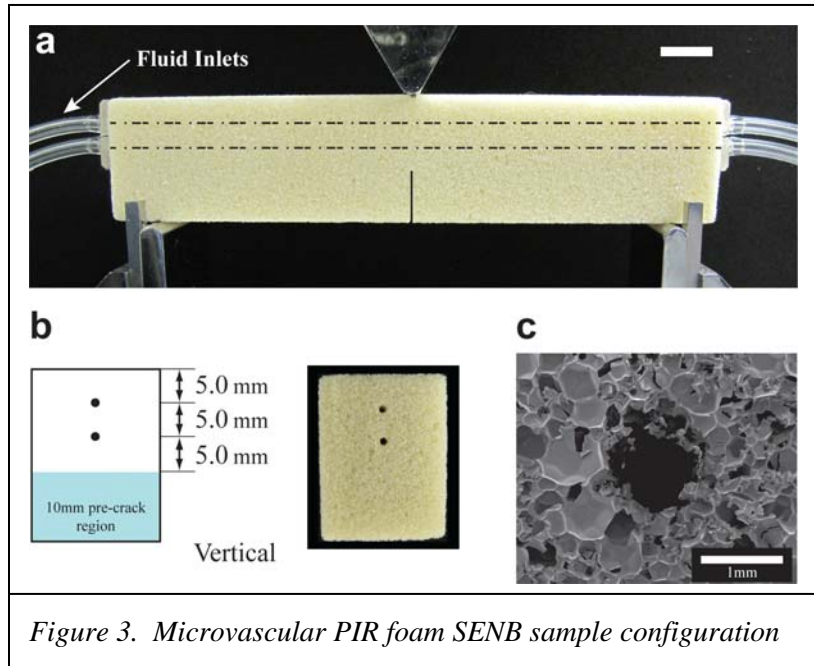
Two commercial, rigid polyurethane (PUR) foam formulations were investigated. Trymer 3000, a PUR modified polyisocyanurate (PIR) produced by DOW Chemical, was obtained in the form of 25mm thick boardstock. X-30, supplied as a two-component liquid PUR system, was obtained directly from TAP Plastics and used as received. The first component of the X-30 system, commonly and herein referred to as Part A, consists of methylene diphenylene diisocyanate (MDI). The second component, designated Part B, consists of a proprietary blend of polyols, hydrofluorocarbon blowing agents, and a chlorinated phosphate ester flame retardant.

A three-point Single Edge Notched Bend (SENB), mode-I fracture test, was selected as the mechanical testing protocol to assess healing performance. A schematic of the test setup is shown in Fig. 2. Rectangular beam samples were cut and sanded to dimensions: Length ($L = 120\text{mm}$), Height ($W = 25\text{mm}$), Depth ($B = 19\text{mm}$), whereas the span length ($S = 100\text{mm}$) was

set by the test fixture supports. Prior to testing, a pre-crack of length ($a = 10\text{mm}$) was introduced at mid-span on the tensile side of the specimens using a razor blade. Plane-strain fracture toughness K_{IC} , is calculated according to Eq .1. The samples were loaded to failure on a load frame under displacement control at a rate of $25\mu\text{m/s}$.

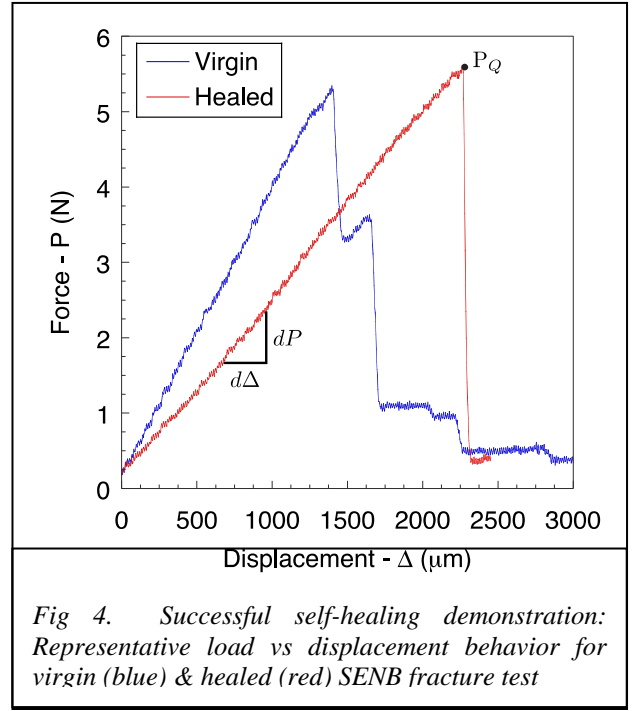


Trymer 3000 is a rigid foam, i.e. closed-cell material with low absorption ($<0.7\%$ by vol.), enabling the vascular containment of liquid healing agents within its microstructure. Self-healing SENB specimens of the same outer dimensions (Fig.2) were vascularized by machining two channels with an average diameter of $970 \pm 40\mu\text{m}$ in a vertical configuration, spaced at a constant 5mm along the entire length, as shown in Fig. 3. Barbed tube fittings were embedded into the ends of both channels, and served as sealed connections for the external tubing to supply liquid healing agents. The healing agents, X-30 Parts A and B, were separately contained in plastic syringes connected to the vascular foam samples via tubing, and precisely delivered ($\pm <1\%$) using a syringe pump.



The “virgin” self-healing SENB sample is loaded to propagate the initial pre-crack and fracture through both channels. The loading sequence is then paused and the healing agents are delivered to the crack plane. The sample is carefully moved to a fume hood, where it is placed on a mimic support structure and allowed to heal for a prescribed time at room temperature ($RT \sim 22^\circ\text{C}$). Representative load

versus displacement curves for a virgin and healed SENB test are provided in Fig. 4. The virgin curve (blue), indicates first propagation of the pre-crack occurs around 1500 μm displacement followed by a series of progressive fractures until the load carrying capacity is virtually diminished around 3000 μm displacement. The healed test (red), often failed in a more dynamic fashion characterized by a single crack propagation event. The representative healing curve clearly depicts a considerable recovery of mechanical integrity both in terms of stiffness ($dP/d\Delta$) and peak load (P_Q) carrying capacity used to determine Mode I fracture toughness.



Two metrics for quantifying healing efficiencies have been defined in Eq. 2:

$$\psi = \frac{dP/d\Delta^{\text{Healed}}}{dP/d\Delta^{\text{Virgin}}} \quad \eta = \frac{K_{IC}^{\text{Healed}}}{K_{IC}^{\text{Virgin}}} \quad (2)$$

In addition to the customary healing efficiencies, new metrics designated “specific” healing efficiencies are calculated according to Eq. 3. These were developed to account for the increased weight due to the relatively high-density healing agents sequestered in a lightweight host material.

$$\bar{\psi} = \psi \cdot \left(\frac{\rho^{\text{Healed}}}{\rho^{\text{Virgin}}} \right) \quad \bar{\eta} = \eta \cdot \left(\frac{\rho^{\text{Healed}}}{\rho^{\text{Virgin}}} \right) \quad \rho \equiv \text{mass density} \quad (3)$$

The microvascular SENB specimens were evaluated for healing performance with Parts A and B sequestered in the top and bottom channels respectively. Fig. 5a summarizes the results obtained from five samples at each of the total volumes (20, 40, 80 μL) of healing agents delivered for a pumping ratio of 1A:1B and tested after 24 hrs at RT. The plot indicates a nearly linear increase in both stiffness and fracture toughness healing efficiencies as the amount of healing agent increases. The explanation is straightforward; as the amount of healing agents delivered increases the more PUR foam is produced to expand and fill a greater portion of the fractured region. This is visually observed in a series of optical images (5b) taken after 30 min. post-healing agent delivery and unloading of the virgin sample. On average, specific healing efficiencies were 19% lower than standard metrics, strictly due to the increased weight from the sequestered liquid healing agents.

The reaction between X-30 Parts A and B is rapid, even in the absence of complete mixing, with PUR foam ejecting from the crack plane on the order of minutes. Thus it was necessary to evaluate the reaction kinetics and determine just how fast healing could occur. A series of self-healing cure kinetics investigations were performed by testing five samples at each of the various time periods (30 min, 1 hr, 2hrs, 4hrs, 6hrs, 24hrs), for a total delivery of 80 μ L at a constant pumping ratio of 1A:1B. The results of this study are shown in Fig. 6. After only 30 minutes of delivering the 2-part healing agents, healing efficiency in terms of both stiffness and fracture toughness had reached approximately 43%. As time progressed, stiffness reached a maximum value more quickly than fracture toughness. Eventually, fracture toughness values exceeded stiffness healing efficiencies, achieving over 100% recovery in the virgin strength. A publication summarizing this research is currently in preparation and will be submitted next month.

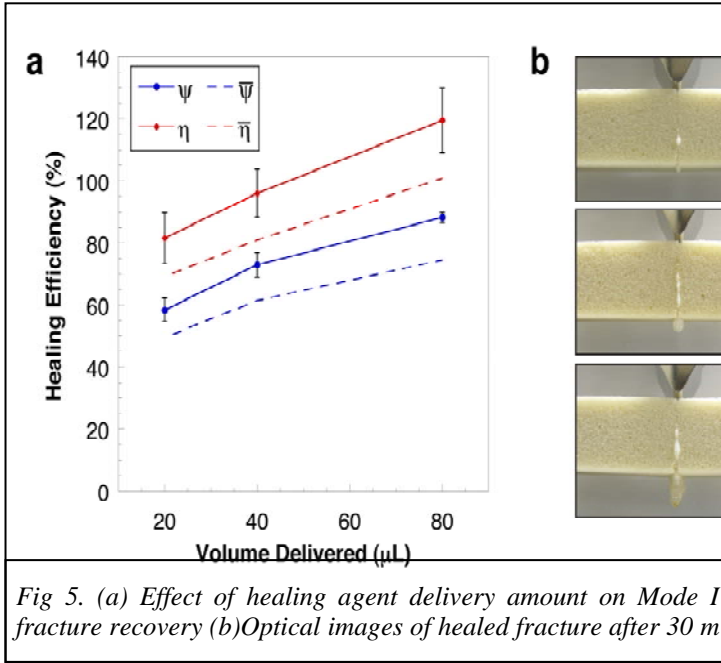


Fig 5. (a) Effect of healing agent delivery amount on Mode I fracture recovery (b) Optical images of healed fracture after 30 m

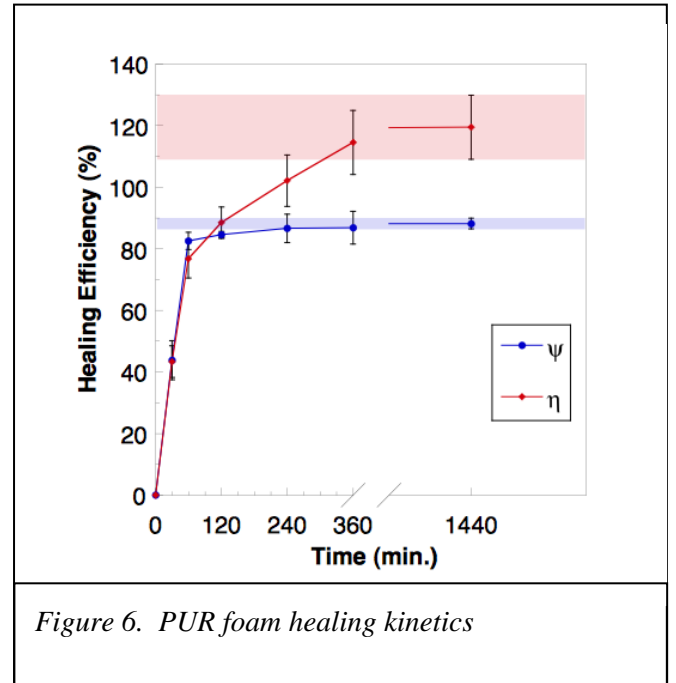
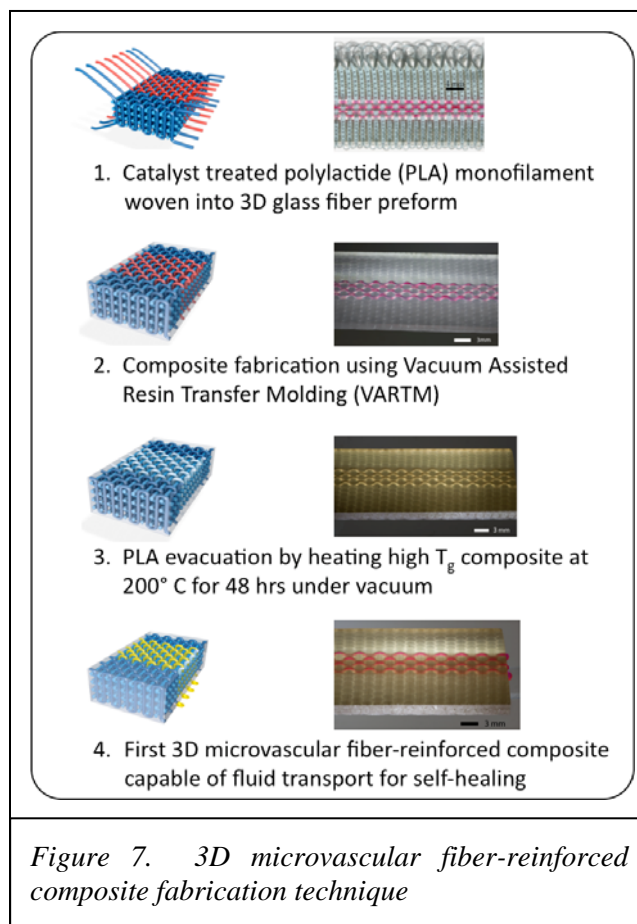


Figure 6. PUR foam healing kinetics

2. 3D Microvascular Fiber-Reinforced Composites

The second component of the proposed structural sandwich panel and vital to the mitigation of blast-induced damage is the 3D woven composite face sheets. We have recently developed a novel technique for incorporating vascular networks into fiber-reinforced composites that are capable of containing liquids. This feature will not only allow self-healing functionality but also provide a conduit for additional utility such as fire-protection. The vascularization (VaSC) procedure is outlined in Fig. 7. The process begins with catalyst-impregnated polylactide (PLA) monofilament being woven, into an E-glass, textile preform (7a). Epoxy infuses the technical fabric by means of Vacuum Assisted Resin Transfer Molding (VARTM), which cures to form a composite (7b). Following a post-cure (150°C), the fiber-reinforced composite is then heated to 200°C under vacuum and the “sacrificial” PLA fiber depolymerizes, leaving behind inverse replica microchannels (7c). The vascular network can then be filled with various fluids, to imbue self-healing functionality or alternative utility (7d). Future research direction is focused on the demonstration of self-healing in these microvascular composite materials, followed by total integration of the vascular core and face sheet components into a single sandwich panel. The intended outcome of this work is to produce a commercially viable structural composite capable of high-performance blast mitigation and damage recovery.



IV. Students Supported

Jason Patrick, Ph.D. subject: *Self-healing composite sandwich panels for blast resistance*

V. Conference and Journal Publications

Esser-Kahn, A.P., Thakre, P.R, Dong, H., Patrick, J.F., Vlasko-Vlasov, V.K., Sottos, N.R., Moore, J.S. and White, S.R. Three-Dimensional Microvascular Fiber-Reinforced Composites, *Advanced Materials* **23**, 3654-3658 (2011).

Patrick, J.F., Farfield, D.J., Sottos, N.R., White, S.R. Microvascular Based Self-healing Polymeric Foam, Proceedings of the 3rd International Conference on Self-Healing Materials, Bath, U.K. June 2011.

Patrick, J.F., Sottos, N.R., White, S.R. Microvascular Based Self-healing Polymeric Foam, *In Preparation for Submission to Polymer*, (2011).

Self-Healing Concrete

Triparna Bhattacharya, Arijit Bose
Chemical Engineering, University of Rhode Island

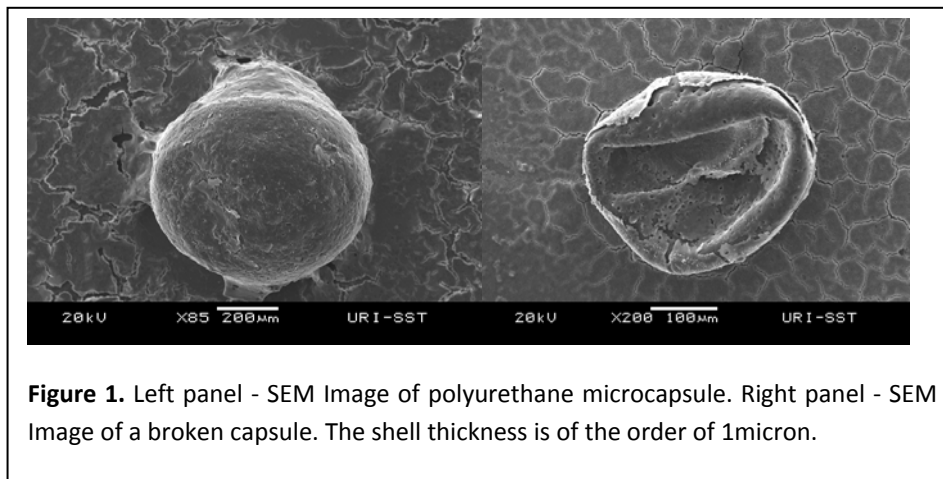
Objectives

We explore a novel concept where external stress is used to trigger crack healing in concrete. Polyurethane microcapsules prepared by interfacial polymerization of an emulsion and filled with sodium silicate solution are incorporated randomly into a concrete mixture. As a crack propagates and encounters a microcapsule, it ruptures the shell, releasing the sodium silicate solution into the crack. The sodium silicate solution flows into the crack via capillary action and reacts with calcium hydroxide present in the cement to form a calcium-silicate-hydrate gel, which partially heals the crack. We have shown that the healed material recovers a large portion of its original flexural strength. The compressive strength is not affected. Current work is focused on characterizing this concrete under dynamic loading conditions.

Experimental Details

Preparation of microcapsules: Polyurethane microcapsules containing sodium silicate are formed through interfacial polymerization. Preparation of the capsules included the following steps: (1) dispersion of the sodium silicate solution in toluene, (2) addition of the shell-forming interfacially active monomer, dimethyl isocyanate (DMI) solution, and (3) formation of the shell by thermally induced interfacial polymerization of DMI to polyurethane. Figure 1 shows a whole and a broken microcapsule. The polyurethane shell thickness is of the order of $1\mu\text{m}$ for this sample.

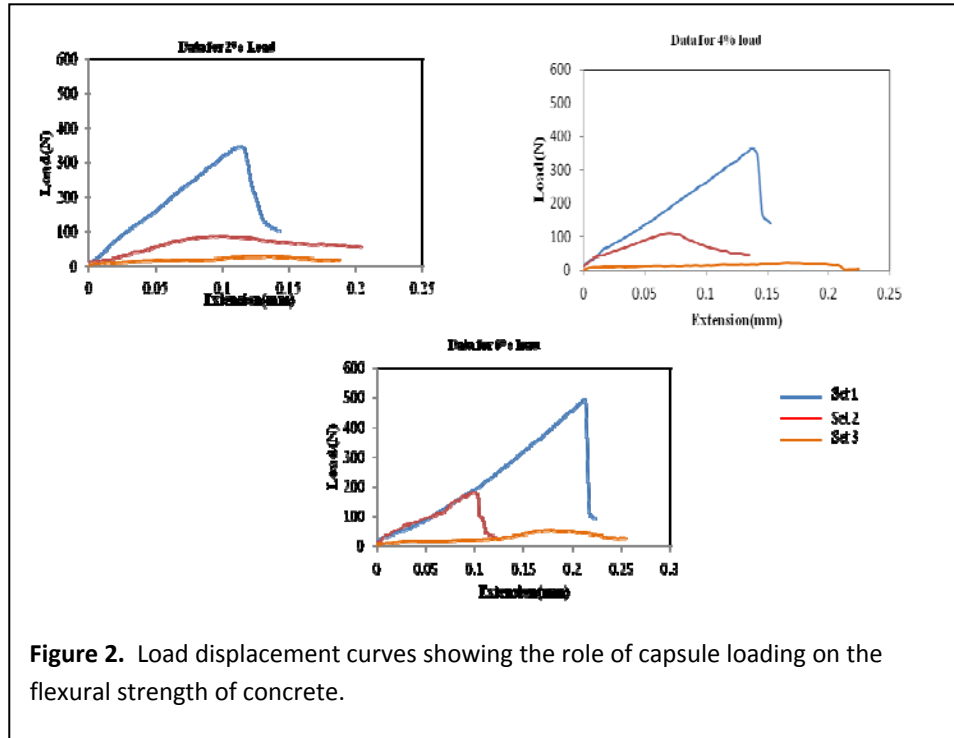
Preparation of concrete samples: All samples are prepared to the specifications of ASTM C-109 with a mix containing 1375 grams of Ottawa C-109 sand, 500 grams of Type I/II Portland cement and 242 mL of water. For samples containing the polyurethane microcapsules, the capsules were added to the mix water at 2% volume (or another volumetric concentration) and prepared identical to the control samples. Molds of dimensions 160mm x 40mm x 20mm (for flexural strength) and 500mm x 500mm x 500mm (for compressive strength) were used. After being stripped from the molds, the specimens were submerged in water for two days then contained in a 95% constant humidity environment for 28 days to ensure full curing.



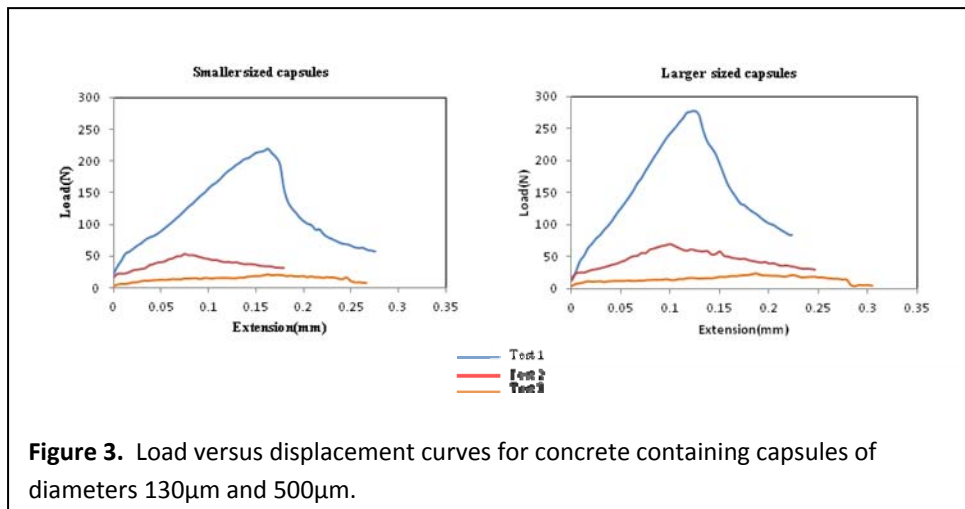
Randomized internal microscale damage was induced with an applied load to incipient failure, to mimic realistic cracking patterns. Samples were allowed to cure for 7 days after each load displacement cycle had and recharacterized to monitor healing efficiency.

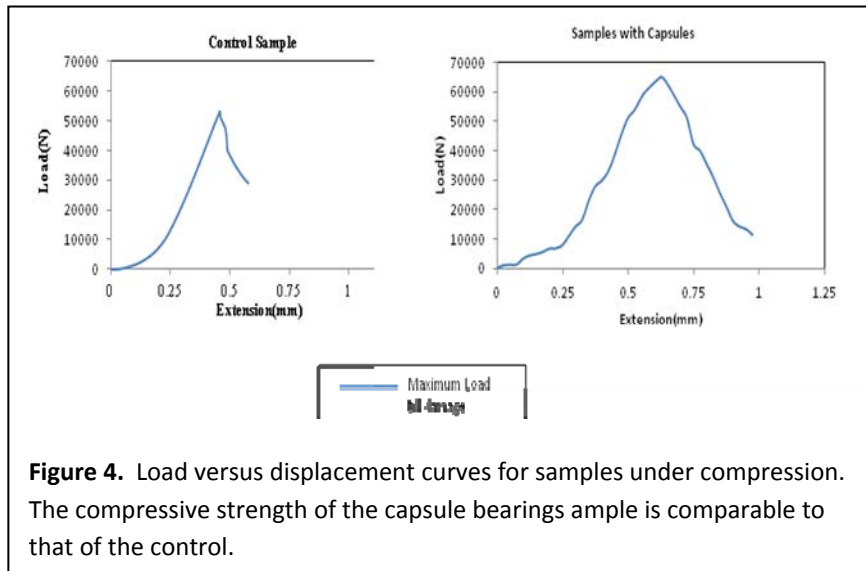
Results & Discussion

Effects of capsule loading on flexural strength of concrete: Capsules were loaded at 2%, 4% and 6 % by volume into the concrete specimens and characterized after 28 days. Figure 2 shows load versus displacement profiles for each load cycle. As the number concentration of capsules increased the recovery of flexural strength of the concrete improved. We believe this is a direct consequence of a larger number of capsules being ruptured as the concentration of capsules increases.



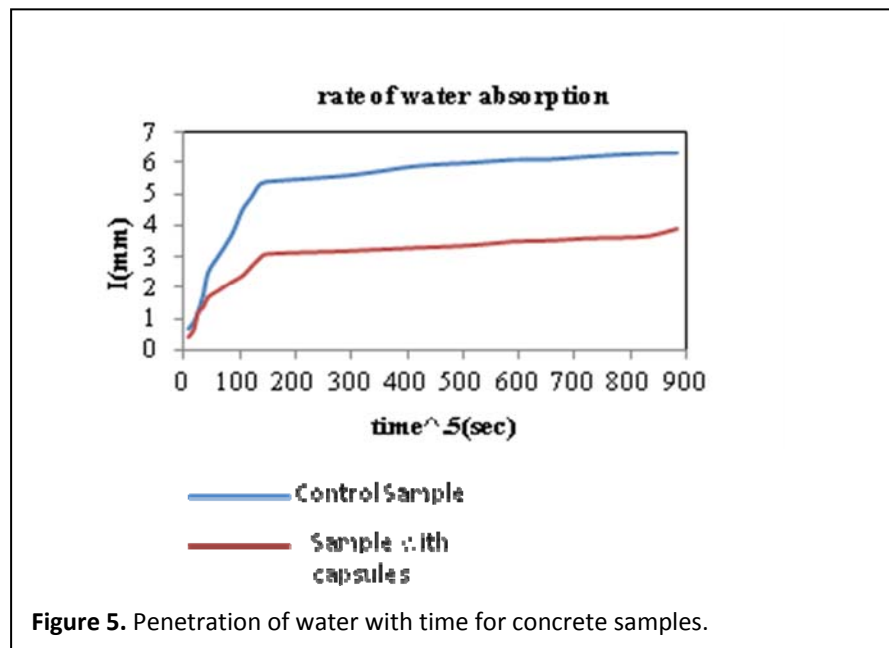
We have examined the role of varying the capsule size at 2% volume loading. Microcapsule sizes of approximately 130 μ m and 500 μ m were incorporated into the concrete and tested. Figure 3 displays the load versus displacement curves for these samples. The samples with smaller capsules have an average recovery of 28.7% and the samples with larger capsules had a recovery of 27.13%, a difference that appears to be statistically insignificant. We believe that the lower number concentration of the larger capsules compensates for their ability to break more easily.





Effect of capsules on the compressive strength of concrete: The compressive strength of each specimen is adapted from ASTM C109. Control and specimens with capsules were tested in an Instron machine. Figure 4 shows the maximum load the samples can take before damage. The presence of capsules does not have any adverse effect on the compressive strength of the concrete.

Effect of capsules on the water absorption rate of concrete: Cubes of concrete specimens were exposed to water from one face, and their mass was recorded over 8 days. Figure 5 compares the rate of absorption of water for control and test samples. Both the rate as well as the final water content in the capsule-containing sample is less than that for the control. The release of healing agent causes the overall permeability, porosity and connectivity of material to decrease thus decreasing the intake of water.



Conclusions

The experiments presented in this study focused on the healing potential of concrete in the presence of sodium silicate encapsulated polyurethane microcapsules. The results show that in the presence of well

formed capsules the properties of concrete are enhanced. Further experiments are being done to check the behavior of this capsule-bearing concrete under dynamic loading conditions and also characterize the corrosion inhibiting capability.

Graduate students supported:

Michelle Pelletier – 2007-2009, MS.

Triparna Bhattarcharya – 2010-2011; MS

Svenja Reinke – 2011-2012; MS/Diplome

Nicholas Heeder – 2011-2012; Ph.D.

Publications

Self-healing Concrete, M. Pelletier, R. Brown, A. Shukla, A. Bose, in review, Cement and Concrete Research, 2011.

Presentations

IMPLAST 2010 – Providence

CEMEX, Zurich – 2011

WR Grace, Cambridge – 2011

Patent

Self- mending concrete – provisional patent application filed, June 25, 2011